Measuring the Density Structure of Star-Forming Dense Cores

A thesis presented

by

Daniel Harvey

to

The Department of Astronomy

in partial fulfillment of the requirements
for the degree of
Doctor of Philosophy
in the subject of
Astronomy

Harvard University
Cambridge, Massachusetts

August 2003

Measuring the Density Structure of Star-Forming Dense Cores

Dr. David J. Wilner Daniel W.A. Harvey

Abstract

I have used two newly feasible observational techniques — dust extinction, and dust emission — and intensive computer modeling to measure the density structure of selected dense molecular cloud cores that are evolving to form stars: protostar Barnard 335, and contracting starless core Lynds 694–2. These measurements test competing theories of isolated star formation, the process by which stars like the Sun are formed. In particular, the studies of B335 provide insight into the dynamics of protostellar collapse, while the studies of L694–2 provide insight into the initial conditions.

The extinction study of B335 is the only extinction work that has been done with the Hubble Space Telescope. The data provide a quantitative test of the "inside-out" collapse model: the *shape* of the density profile is well matched by the model, but the *amount* of extinction corresponds to larger column densities than predicted. The emission observations constrain the flux from the circumstellar disk, and demonstrate an inner density structure consistent with the profile of gravitational free-fall, as predicted for the formation of a star. Combined, these studies constrain the density profile with a precision that is unique amongst protostellar cores.

The extinction study of L694–2 shows an outer density profile that is significantly steeper than the initial condition of the inside-out collapse model. The emission observations measure the inner density structure not probed with extinction, demonstrating a turn-over in the density profile to substantially more shallow behavior in the inner regions. The turn-over suggests that pressure forces still support the core, and that it has not relaxed to the singular initial condition of the inside-out collapse model, despite purported inward motions. A cylindrical model viewed nearly end-on reproduces all the observations remarkably well, including the apparent asymmetry of the core. In this context the inward motions may represent the contraction of a

prolate core along its major axis. If the core is sufficiently magnetized then fragmentation may be avoided, and later evolution might produce a protostar similar to B335, with mass larger than expected for a spherically symmetric core.

Contents

For my family and friends

The known is finite, the unknown infinite; intellectually we stand on an islet in the midst of an illimitable ocean of inexplicability. Our business in every generation is to reclaim a little more land.

T.H. Huxley

Acknowledgements

This thesis stems from a simple satisfaction in solving problems and a desire to understand the physical processes that govern the world around us. My appetite for learning was instilled at an early age, and reinforced throughout my childhood. Without this teaching and encouragement from my family, this PhD would not have been possible.

I am greatly indepted to my advisor David Wilner. Thank you for taking me on as your student, and giving me the opportunity to contribute to our understanding of the Star Formation problem. You have provided me with inspiration at times when it was lacking. I hope future graduate students will benefit as I have from your perspective on science, and your relaxed and supportive advising.

Other scientists who have added significantly to my graduate education include: Alyssa Goodman, Charlie Lada, Avi Loeb, Phil Myers, Ramesh Narayan, George Rybicki, and Pat Thaddeus.

A number of CfA graduate students have contributed to my overall experience. In particular, I want to thank my good friend Aaron Sokasian as a constant source of support and advice throughout my time at the CfA. Your comradeship kept me sane, and your ambition helped me maintain my focus. Pinaki Chatterjee, Jonathan Jenkins, Aaron Tustin and Xiaohu Wang all made the CfA a more friendly place.

There are a number of people who have greatly enhanced my life as a whole during my work on this thesis, and to whom I am very grateful. In particular: Drew Kowalevicz who ensured I didn't forget any simple physics; Klay Dendrinos my companion at the Fells;

Brian Locher who opened my eyes to Jiu-Jitsu; Jay Ku my cycling buddy; and Sandy Noyes who made Boston feel like my home.

Chapter 1

Introduction

1.1 Background

The origin of stars represents one of the most fundamental unsolved problems of contemporary astronomy. Stars are the basic objects of the universe. The discovery of their nature as natural thermonuclear reactors, and the subsequent development of the theory of stellar evolution rank amongst the greatest achievements of 20th-century science. We know that the heavy elements of which we are made are the by-products of the reactions that took place in the centers of previous generations of stars, and in the supernova events by which they ended their lives. We are able to follow in quantitative detail the lives of stars as they exhaust their fuel reserves and evolve to their eventual death. But deciphering the first stage of stellar evolution — stellar genesis — still eludes us.

Bok & Reilly (1947) first drew attention to "Dark Nebulae" as holding the key to star

birth in the solar neighborhood. Through the years, spectral line surveys of these molecular hydrogen clouds have identified a large sample of dust-enshrouded dense cores (e.g. Benson & Myers 1989), of which roughly half are associated with young stellar objects detected by IRAS — the Infra-Red Astronomy Satellite (Beichman et al. 1986). The properties of these cores have been adopted into a standard model of isolated star formation. In the theory, a slowly rotating, nearly spherical dense core loses magnetic support and relaxes to a balance between gravity and thermal pressure. The balance is critically unstable and the dense core collapses under its self-gravity. Material falls towards the center, achieving near free-fall in the innermost regions. At some stage, material from the outer envelope of the core has too much specific angular momentum to reach the center directly, and collapses into the rotation plane forming a circumstellar accretion disk. The disk transfers matter onto the central star, shedding angular momentum via a high velocity bipolar outflow. The disk also provides the reservoir of mass out of which a planetary system may eventually form. This standard theory has proved very successful in many predictions (see the review of Shu et al. 1993), but one fundamental aspect has proved elusive: compelling observational evidence for gravitational collapse. Indeed, the identification of a collapsing protostar is a "holy grail" of star formation research.

The search for protostellar collapse is difficult for several reasons. First, collapse likely initiates in the center of the core, in which case it will only be detectable with observations of sufficiently high resolution to probe the infall region. Second, the collapse process takes place over a period of a few $\times 10^5$ years, so the evolution of a given core is not observable. The inward motions associated with the collapse can theoretically be measured via their

Doppler shift, but the velocities of these motions are small, comparable to the intrinsic thermal velocity, and much smaller than the velocities of the bipolar outflows that are powered by the young stellar objects. To date the most promising claims for collapse have been inferred from subtle signatures in molecular spectral lines. But, the signatures are not unique to a collapse scenario, and consequently these claims have often been the subject of controversy.

The appropriate initial conditions to protostellar collapse are also the subject of debate. The "starless" dense cores represent the earliest stage of the star formation process. The physical conditions in this early stage have a profound impact on the eventual evolution of the protostar towards the main sequence. The initial density structure, particularly in the innermost regions, determines the dynamics of the collapse and the rate at which infalling matter is deposited onto the protostar (Foster & Chevalier 1993). In turn, this affects many of the observable properties of the protostar, including luminosity. Better observations of starless cores are needed to constrain the initial conditions of the collapse process.

The best and most direct way to study the structure and dynamical state of a dense core is to observe the way in which the mass of the core is distributed. The continuity equation of fluid dynamics means that a measurement of the density structure provides information on the velocity fields in the core. For instance, material in gravitational free-fall, as expected for the central regions of a collapsing protostar, has a density distribution that is a power law: $\rho \propto r^{-3/2}$. Observations that constrain the density structure of both starless cores and collapsing protostars are therefore vital to improving our understanding of the star formation process. Precise measurements of the density structure of starless cores

will constrain the appropriate initial conditions of the collapse process. Measurements of the density structure of protostellar cores can constrain the dynamics of the collapse, and test quantitatively the competing theories. This thesis attempts to address these issues.

1.2 Measuring the Density Structure of Dense Cores

The majority of the mass of dense cores is in the form of molecular hydrogen (H_2). Unfortunately, H_2 is not directly observable under the conditions that are present in these clouds. This occurs for two reasons: 1) H_2 is a homonuclear molecule that lacks a permanent dipole moment and has very weak rotational transitions; 2) the molecule is very light, with lowest rotational transitions having high excitation energy (stemming from angular momentum quantization), lying at mid IR wavelengths which are unobservable from the ground (blocked by the atmosphere) and are also not excited at the cold (T<10 K) temperatures of the cores. Generally, the physical properties of dense cores have had to be inferred from observations of "tracers", species such as CO, CS, NH_3 that are many orders of magnitude less abundant (typically 10^4–10^9) than H_2. But, variations in chemical abundance, opacity, and excitation conditions render the interpretation of such observations complicated.

The most robust way to trace molecular hydrogen is to observe dust. Essentially, dust does not suffer the severe excitation and depletion effects that plague observations of molecular spectral lines. The gas-to-dust ratio in interstellar clouds has been established observationally to be fairly constant (e.g. Bohlin, Savage, & Drake 1978), though these measurements have been made in regions with much lower column density than protostel-

lar dense cores, so grain growth in these dense regions (due to molecular depletion and agglomeration) may affect this claim.

1.2.1 Dust Emission Observations

A direct method for measuring the density structure of dense cores utilizes observations of long-wavelength dust emission, where the intensity provides an integral along the line-of-sight of the product of the dust temperature and density. By modeling the dust temperature and specific mass-opacity, the observed intensities constrain the density distribution of the core. This technique has been successfully exploited to study both starless cores and protostars using bolometer cameras on large single dish telescopes, including the IRAM 30 meter (Ward-Thompson, Motte & Andre 1999) and the JCMT (Shirley et al. 2000; Visser, Richer & Chandler 2001). But single-dish studies inevitably lack the resolution to accurately constrain the density structure in the inner regions of a dense core (resolution $\sim 15''$). The structure on smaller size scales can only be probed using interferometers. Observations of dust continuum with mm-wave interferometers can sample the density profile to size scales about an order of magnitude smaller than single dish data. With interferometer data, the density fall-off with radius in the inner regions can be constrained through analysis of the dust emission directly in the visibility domain (e.g. Keene & Masson 1990, Mundy, Looney & Welch 2000, Harvey et al. 2003a, Harvey et al. 2003c, Looney, Mundy & Welch 2003). This approach is intensive computationally, but recognizes the limitations of standard Fourier inversion and deconvolution techniques, and thereby sidesteps problems caused by the characteristics of the synthesized beam.

Starless cores and protostars present two different challenges to study with an interferometer. Starless cores tend to have shallower central density profiles and are less centrally condensed than cores of similar mass that contain embedded protostars. This means that generally they are highly resolved on all but the shortest baselines that can be achieved with available millimeter interferometer arrays, making it a challenge to even detect the core, let alone measure structure. In addition, the lack of a well defined center can make choosing where to point the array difficult. In contrast, protostellar cores present little difficulty for detection with modern interferometers, and the envelope may be presumed to be centered on the location of the protostar. However, the presence of the central source complicates the modeling of the envelope structure. This complication also arises in single dish studies of protostellar cores. Essentially, a combination of a bright central source and a shallow envelope can mimic a combination of a dim central source and a steeply-falling envelope. An uncertain brightness of the central source therefore leads to an imprecise measurement of the density structure of the surrounding core. The degeneracy between envelope and central source can only be broken by interferometer observations that span a wide range in baseline. Measurements on long baselines where the envelope is heavily resolved can constrain the compact component of the emission from e.g. a circumstellar disk. With the flux of the compact component thus constrained, short baseline measurements then provide a direct and precise measure of the envelope density structure.

1.2.2 Dust Extinction Observations

Observations of dust extinction arguably provide a more reliable measure of column density than observations of dust emission, mainly because extinction is not sensitive to gradients of dust temperature. This approach utilizes the property that the effective cross-section of dust grains decreases with increasing wavelength of the radiation. The basic method is to observe stars background to the dense core at two different but nearby wavelengths. The observations are best made at near-infrared wavelengths, where the cross-section of the dust is much smaller than at optical wavelengths, thereby allowing denser regions to be probed. The difference in brightness of a given background star between the two near-infrared filters, termed its *color*, is the sum of the star's intrinsic color and the differential optical depth of the core at that position, termed the *color excess*. The color excess from the core is directly proportional to the dust column density via a near infrared reddening/extinction law. The dust column density, in turn, is proportional to the gas column density via the gas-to-dust ratio. The extinction law and gas-to-dust ratio are effectively constant, since departures due to grain growth, etc. are small at near infrared wavelengths (Martin & Whittet 1990). In practice, the intrinsic colors of the individual stars need not be measured directly since they span a small range; a statistical correction can be obtained empirically, taking account the star colors in nearby fields.

Thus, observations of a dense core through two near-infrared filters provide measurements of the column density distribution at the positions of the background stars. With detailed modeling, these estimates can be used to determine the overall structure of the obscuring core. Historically, this method has been impossible to apply to small regions of high

extinction because of poor sensitivity and a paucity of background stars, even at infrared wavelengths where the method is most efficient (e.g. Bok & Cordwell 1973, Jones et al. 1980, 1984). But the development of large format near-infrared array cameras sparked renewed interest in the technique (e.g. Lada et al. 1994, Alves et al. 1998). The sensitivity available on large ground-based telescopes and the Hubble Space Telescope has made accessible the immediate environs of starless dense cores and candidate protostars (Alves, Lada & Lada 2001, Harvey et al. 2001, Harvey et al. 2003b).

1.3 Thesis Work

Combining observations of dust extinction and emission from a dense core provides an extremely powerful tool for measuring density structure. The two methods are very complementary since they probe different regions of a dense core. Extinction studies are most sensitive in the outer envelopes where the sample of background stars is highest but where the core is heavily resolved in emission studies with interferometers. In contrast, emission studies are most sensitive in the high column density, inner regions, where the dust emission is strongest, but which cannot be penetrated by extinction observations. A combination of the two techniques can provide a complete study of the density structure of a dense core on all size scales down to subarcsecond level ($\sim$ 100 AU for nearby dense cores).

For my thesis, I have used these techniques to constrain the density structure of two carefully selected isolated dense cores that may be in the process of evolving to form stars: protostellar collapse candidate Barnard 335, and candidate contracting starless core

Lynds 694–2. Figure 1.1 shows the Digital Sky Survey POSS-II image of the region (J band) containing the two cores. Both cores are both fairly isolated, round condensations, situated very close to each other on the sky (separated by less than 4°). Indeed the cores have likely formed from the same parent molecular cloud complex. Molecular spectral lines observed in both cores exhibit strong redshifted self absorption, an indication that inward motions are likely present. Yet the two cores differ significantly in their evolutionary state: the B335 core harbors an embedded young stellar object and a strong bipolar outflow, while L694–2 is apparently starless.

The dust extinction study of B335 (Chapter 2) is the first application of this method to a candidate protostar, and the only extinction work that has been done with the Hubble Space Telescope. The results were presented at the European Southern Observatory (ESO) Star and Planet Formation meeting in April 2001. The dust emission studies of B335 (Chapters 3, 4) provide the first millimeter-wave flux measurement for the circumstellar disk, and constrain the inner density profile with unprecedented precision. The studies of contracting starless core L694–2 in dust extinction (Chapter 6) and dust emission (Chapter 7) provide the most precise and complete measurement of the density structure of a core in this most important intermediate evolutionary phase. The studies raise many interesting questions concerning the important effects of departures from spherical symmetry in the early stages of the star formation process. We have also studied L694–2 (and selected other starless cores) with the Very Large Array to confirm the starless nature of this core (Chapter 5).

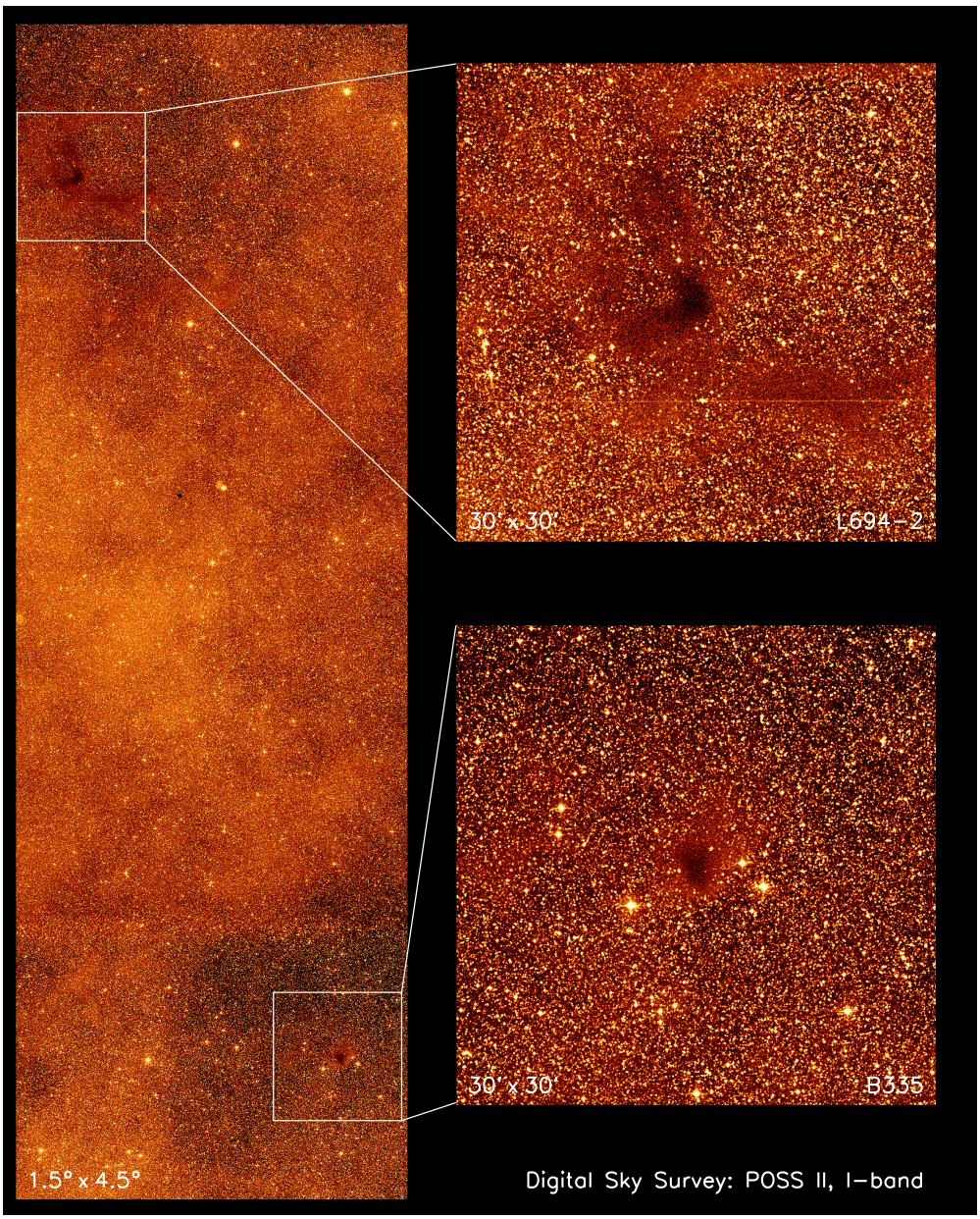

Fig. 1.1.— Wide field J-band image of the region containing protostellar core B335 and starless core L694–2 from the Digital Sky Survey. The two cores are separated by less than 4°. Both are fairly isolated, round condensations that likely formed from the same parent cloud complex.

Chapter 2

Structure of Protostellar Collapse Candidate B335 Derived from Near-Infrared Extinction Maps [1]

Daniel W.A. Harvey, David J. Wilner, Charles J. Lada, Philip C. Myers, João F. Alves, & Hua Chen 2001, *The Astrophysical Journal*, **563**, 903

---

[1]Based on observations with the NASA/ESA Hubble Space Telescope, obtained at the Space Telescope Science Institute, which is operated by the Association of Universities for Research in Astronomy, Inc. under NASA contract No. NAS5-26555, and observations obtained at the W.M. Keck Observatory, which is operated as a scientific partnership among the California Institute of Technology, the University of California and NASA, made possible by the generous financial support of the W.M. Keck Foundation.

Abstract

We present a near-infrared extinction study of the dark globule B335, a protostellar collapse candidate, using data from HST/NICMOS and the W.M. Keck Observatory. These data allow a new quantitative test of the "inside-out" collapse model previously proposed to explain molecular line profiles observed toward this region. We find that the *shape* of the density profile is well matched by the collapse model, but that the *amount* of extinction corresponds to larger column densities than predicted. An unstable Bonnor-Ebert sphere with dimensionless outer radius $\xi_{\rm max} = 12.5 \pm 2.6$ provides an equally good description of the density profile, and is indistinguishable from the collapse model over the range in radius sampled by the extinction data. The bipolar outflow driven by the embedded young stellar object has an important effect on the extinction through the core, and modeling the outflow as a hollowed-out bipolar cone of constant opening angle provides a good match to the observations. The complete extinction map is well reproduced by a model that includes both infall and outflow, and an additional 20% dispersion that likely results from residual turbulent motions. This fitted model has an infall radius of $R_{\rm inf} = 26 \pm 3''$ (0.031 pc for 250 pc distance), and an outflow cone semi-opening angle of $\alpha = 41 \pm 2°$. The fitted infall radius is consistent with those derived from molecular line observations and supports the inside-out collapse interpretation of the density structure. The fitted opening angle for the outflow is slightly larger than observed in high velocity CO emission, perhaps because the full extent of the outflow cone in CO becomes confused with ambient core emission at low velocities.

2.1 Introduction

The near-infrared color excess of extincted background stars can reveal the dust distribution in a dense core and provide information on physical structure. Historically, this technique has been hampered in small, dense regions by limited instrumental sensitivity (Jones et al. 1980, 1984), but the development of large format array cameras has sparked renewed interest (Lada et al. 1994, Alves et al. 1998, Lada, Alves & Lada 1999, Alves, Lada & Lada 1999, 2001). The unprecedented sensitivity available with the Near Infrared Camera and Multi Object Spectrometer (NICMOS) instrument on the Hubble Space Telescope (HST) opens up a new regime. In particular, the high extinctions of dense cores that form the immediate environs of candidate low mass protostars are now accessible.

Molecular line surveys of nearby dark clouds have identified a large number of low mass dense cores (Myers, Linke & Benson 1983) of which roughly half are associated with young stellar objects detected by *IRAS* (Beichman et al. 1986). These observations have contributed to the general paradigm that at least some low-mass stars like the Sun form by the gravitational collapse of isolated, dense cores. In the standard theory, originating with Shu (1977), the dynamical collapse to a star/disk system occurs from the inside-out. First, an $n \propto r^{-2}$ distribution is established prior to collapse as the cloud core loses magnetic and turbulent support through ambipolar diffusion and relaxes to a balance between gravity and thermal pressure. Collapse is initiated at the center where the density is highest, and a wave of infall propagates outward at the sound speed. Conditions inside the infall radius asymptotically approach free-fall, with $n \propto r^{-1.5}$ and $v \propto r^{-0.5}$. Modifications to the simple theory have been made to account for more realistic initial conditions, including

slow rotation (Tereby, Shu & Cassen 1984) and residual magnetic fields (Galli & Shu 1993, Li & Shu 1997). A similar radial density profile is also produced by the competing self-similar collapse theory of Larson (1969) and Penston (1969). However, the Larson-Penston flow predicts far larger infall velocities than the Shu theory, and has proved unsuccessful at explaining molecular line observations (see e.g. Zhou 1992).

Unambigous identification of inside-out collapse motions has proved difficult for several reasons. First, the fact that collapse initiates in the center of a core means that it can be detected only with observations of sufficiently high angular resolution. Further difficulty comes from the fact that the velocities associated with infall motions are small, comparable to intrinsic line widths and much smaller than the velocities of the bipolar outflows powered by young stellar objects. The presence of localized, redshifted self-absorption in spectral lines of moderate optical depth provides one signature of infall motions, but this signature is not unique. Scenarios other than collapse can produce the same spectral line profiles. The most promising claims for collapse have been inferred from redshifted self-absorption, and consequently these claims are often controversial (see the review of Myers, Evans & Ohashi 2000).

The dense core in the B335 region is generally recognized as the best protostellar collapse candidate. The B335 region contains an isolated, roughly spherical globule at a distance of roughly 250 pc (Tomita, Saito & Ohtani 1979). Deeply embedded in the globule is a young stellar object discovered at far-infrared wavelengths by Keene et al. (1983) and detected only at $\lambda > 60$ μm by *IRAS*. Observations of high velocity molecular line emission have shown that the young stellar object drives a bipolar outflow with semi-

opening angle of $\sim 25 \pm 5^{\circ}$ (Cabrit, Goldsmith & Snell 1988, Hirano et al. 1988, 1992). Detailed radiative transfer models based on the theory of inside-out collapse provide good fits to many molecular line profiles of dense gas tracers observed at $10''$–$30''$ resolution (Zhou et al. 1993, Choi et al. 1995). These models imply an infall radius of 0.03 pc ($25''$), an age of 1.3×10^5 yrs, and a central mass of 0.37 $M_{\odot}$. While the agreement of the model with few parameters and the observed molecular line profiles strongly support inside-out collapse, the model is not unique. For example, in one extreme scenario discussed by Zhou et al. (1993), an unrelated foreground cloud of just the right excitation properties absorbs emission from a static core and exactly reproduces the infall signatures. Recent molecular line observations of B335 made with the higher angular resolution of interferometry are also starting to show perhaps important discrepancies with the predictions of inside-out collapse (Wilner et al. 2000).

An extinction map of sufficient depth can probe the density structure of B335 and test the claim for inside-out collapse in a way that is free from many of the problems that plague molecular line studies, including excitation effects and spatially varying abundances of the molecular tracers. B335 is fortuitously placed for an extinction study, located at Galactic coordinates $l = 44.9$, $b = -6.6$, which is a direction with a very high density of background stars with uniform properties. Previous optical extinction studies of B335 were not sensitive to the structure of the dense core anywhere close to where the molecular line data suggest collapse (see Bok & McCarthy 1974, Dickman 1978, Tomita et al. 1979 and Frerking et al. 1987). In this paper, we present a near-infrared extinction study of B335 using data from HST/NICMOS, supplemented by data from the W.M. Keck Observatory. Section 2.2

briefly reviews the technique and describes the observations and data reduction. Section 2.3 presents an analysis of the extinction data in the context of several physical models for the B335 density structure, and comparisons with the results of previous studies. Simulations of the observations are also presented, using a Monte Carlo approach detailed in the appendix. Section 2.4 summarizes the main conclusions.

2.2 Observations and Data Reduction

2.2.1 Review of the Near-Infrared Color Excess Technique

Measurements of the extinction of stars background to a dense core provides estimates of column density along many pencil beams. These estimates can be used to determine the overall structure of the obscuring core. The extinction measurements are best done at infrared wavelengths, where absorption due to dust is much less than in the optical, thereby probing regions of higher (visual) extinction. The basic method is to measure the near-infrared color excess for each background star:

$$\mathrm{E(H-K)} = (\mathrm{H-K})_{\mathrm{observed}} - (\mathrm{H-K})_{*} \ , \tag{2.1}$$

where $(\mathrm{H-K})_{*}$ is the intrinsic color of the star. The color excess represents the differential optical depth between the two near-infrared filters, which is directly proportional to dust column density. The observed color excess may be converted to an equivalent visual extinction using the standard reddening law (e.g. Rieke & Lebosfsky 1985), and then converted to gas column density by adopting a gas-to-dust ratio (e.g. Bohlin et al. 1978). There are some uncertainties in both of these conversions. The gas-to-dust ratio in protostellar cores is the

subject of some debate; at low extinction there is some evidence to suggest that it is constant along different lines of sight in the galaxy (Bohlin et al. 1978), but at high extinction it is unclear whether the gas-to-dust ratio remains constant. For example, if grain growth occurs in the high extinction regions as a result of molecular depletion and agglomeration, then one might expect lower extinction for a given column density. The reddening law is probably less problematic and nearly universal at near-infrared wavelengths, given the small grain sizes present in protostellar envelopes (Mathis 1990).

In practice, the color excess method does not require a knowledge of the intrinsic colors of the individual extincted stars. A statistical correction to their observed colors may be obtained empirically from the background stellar population, provided it is sufficiently spatially uniform. For stars of spectral types A0 to late M, in the main sequence or the giant loci, the intrinsic colors lie in the narrow range $0 < (H - K)_* < 0.3$ (Koornneef 1983). Therefore, at high extinctions, little error is introduced by simply assuming a mean background star color derived from nearby control fields.

2.2.2 NICMOS Observations

The B335 globule was imaged with the NIC3 camera on HST (Cycle 7—NICMOS, GO-7843, 1998 June 23) using two broadband filters, F160W and F222M, similar to the usual H band and K band filters that are matched to the 1.6 μm and 2.2 μm atmospheric windows. The NIC3 camera has 256×256 pixels with size $0\farcs20$ giving a $51\farcs2$ field of view. The observations were obtained during the second of two periods of a few weeks when the HST secondary mirror was adjusted to allow the NIC3 camera to be in focus (the "NIC3 Campaigns").

The observing program had two parts: (1) a deep 3×3 mosaic of the central region of high extinction, taking 6 orbits, and (2) a radial strip of images extending about $4'$ from the center, taking 1 orbit, to reach the background stellar population and provide a sample of stars to transform NICMOS magnitudes to a standard photometric system. The length of the strip was the maximum allowed before suffering the heavy overhead of guide star reaquisition. (The strip included the center of B335 as insurance in the event that the deeper observations were unsuccessful.) Figure 2.1 shows the observed fields overlayed on a wide field optical view of the region from the Digital Sky Survey. We note that the NIC3 orientation angle on the sky and stepping direction of the radial strip were given by the spacecraft orientation on the day of observation. Advance specification of a particular orientation would have created an untenable scheduling constraint; the orientation obtained was based solely on where the spacecraft happened to be during the period when the NIC3 camera was in focus and B335 was accessible.

The central region was observed with a standard nine-point spiral dither pattern with $10''$ offsets, and a total exposure time of 896 seconds per dither. The resulting square mosaic covers $72''$. The strip images were taken in *one-chop* mode, an exposure time of 56 seconds per chop, with an offset of $3''$ between chops, and roughly $3''.7$ overlap between successive images. This resulted in a strip of coverage $55''$ wide that extends $247''$ from the mosaic center. The data were taken in the NICMOS *multiaccum* mode, for which an initial readout of the detector array is followed by non-destructive readouts during the course of a single integration. The intermediate readouts can be used to identify and to remove the effects of cosmic ray hits and saturated pixels.

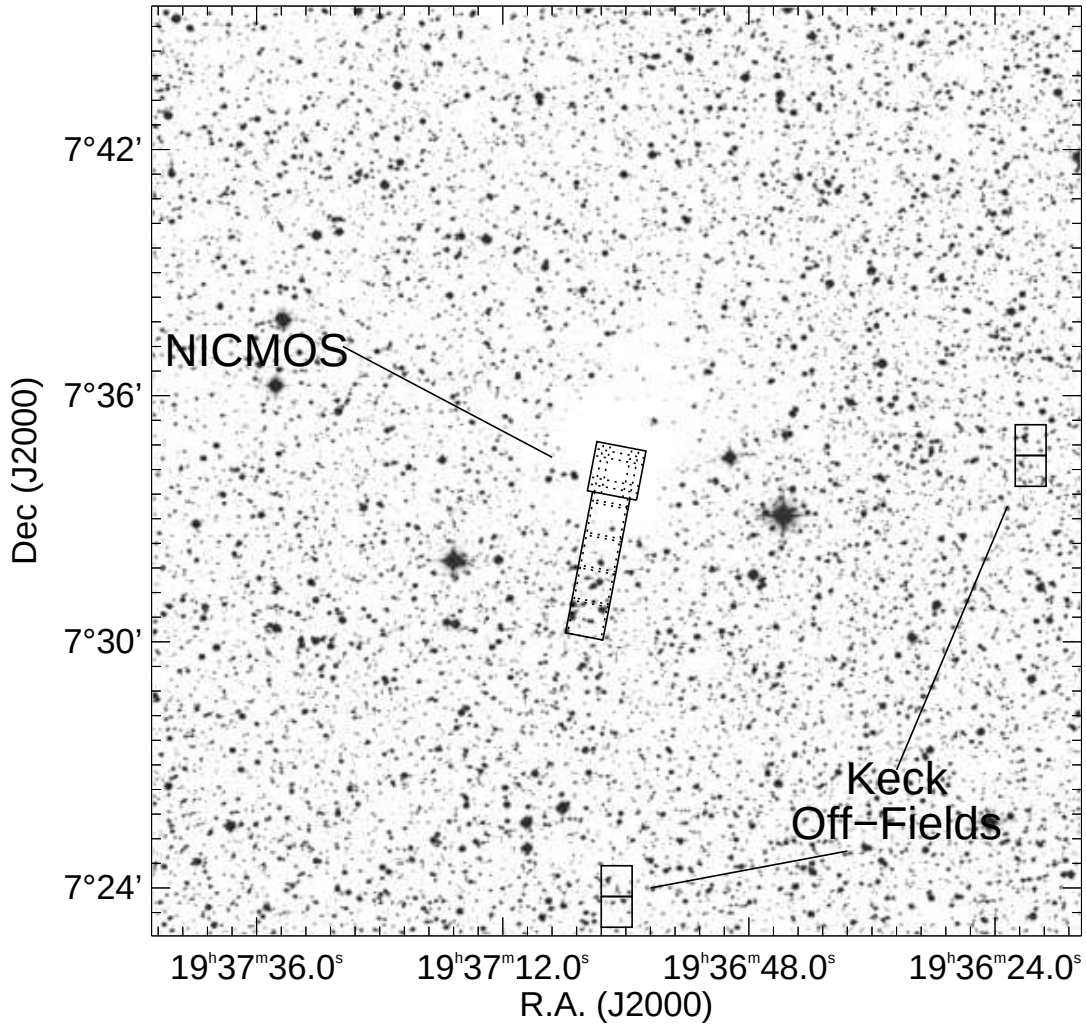

Fig. 2.1.— Wide field optical view of the B335 region from the Digital Sky Survey. Superimposed is a diagram of the observed fields from both NICMOS and Keck.

The NICMOS data were obtained from the HST archive in FITS format both unprocessed and already processed through the STScI pipeline (CALNIC A & B). Initial inspection showed the STScI pipeline did not adequately deal with a variety of instrumental effects, and so we reprocessed the data in IRAF using the NICREDUCE software developed by Brian McLeod (McLeod 1997, Lehar et al. 1999). The NICREDUCE package provides superior and more versatile handling of sky and dark current subtraction, as well as cosmic ray hits and other defects.

The bottom rows of the NICMOS images suffered from a small amount of vignetting. The effect was most pronounced in the F222M images, where about $2\farcs4$ were unusable. The overlap of images in the dither pattern and in successive images of the strip was sufficient to ensure that the vignetting resulted in only a small loss in sensitivity in the affected regions, and no gaps in the spatial coverage.

The dithered images of the central region of B335 suffered an additional complication due to the presence of a very bright star (H magnitude of 9.0) on the west side of the mosaic center. The enormous count rate from the star caused the image reduction software to produce a small depression in the continuum level of the quadrant of each image that contained the star. This deviation was fixed by adding a constant to the relevant quadrant so that for each image the median pixel value was uniform in all four. Ghost impressions of the star in successive exposures were interactively masked in the affected images and were not included in the final mosaic.

Photometry

Stars were identified by visual inspection of the images, as several attempts at automatic star finding were compromised by the effects of diffraction spikes and rings around the brighter stars. Photometry on each star was performed with the suite of routines in the *apphot* package. A series of apertures from $0\farcs2$ to $0\farcs5$ in radius was used for each star. Aperture corrections were then performed using a minimum of four isolated and bright stars from the relevant image. Each aperture was used to calculate a magnitude and associated error as a check to identify any unusual behavior. The measured count rates were corrected to a $1''$ radius aperture, and then multiplied by 1.075 as detailed in the NICMOS Photometric Calibration CookBook (available from STScI). The instrumental magnitudes were then transformed to the Vega scale using constants for each filter provided in the HST Data Handbook (Version 4, Dec 1999). For stars that were observed in a region of overlap between strip images, weighted mean magnitudes were calculated. For stars observed in the overlap region of the central mosaic and the first strip image, the value from the more sensitive central mosaic was taken. The complete NICMOS photometry list contains 1026 stars detected with the F160W filter and 471 stars detected with the F222M filter with magnitude error < 0.1. The NICMOS limiting magnitudes are spatially dependent and are depicted in Figure 2.2. In the central $32''$, with the most integration time, the limiting magnitudes are H=24.8 and K=21.5 (in the CIT system).

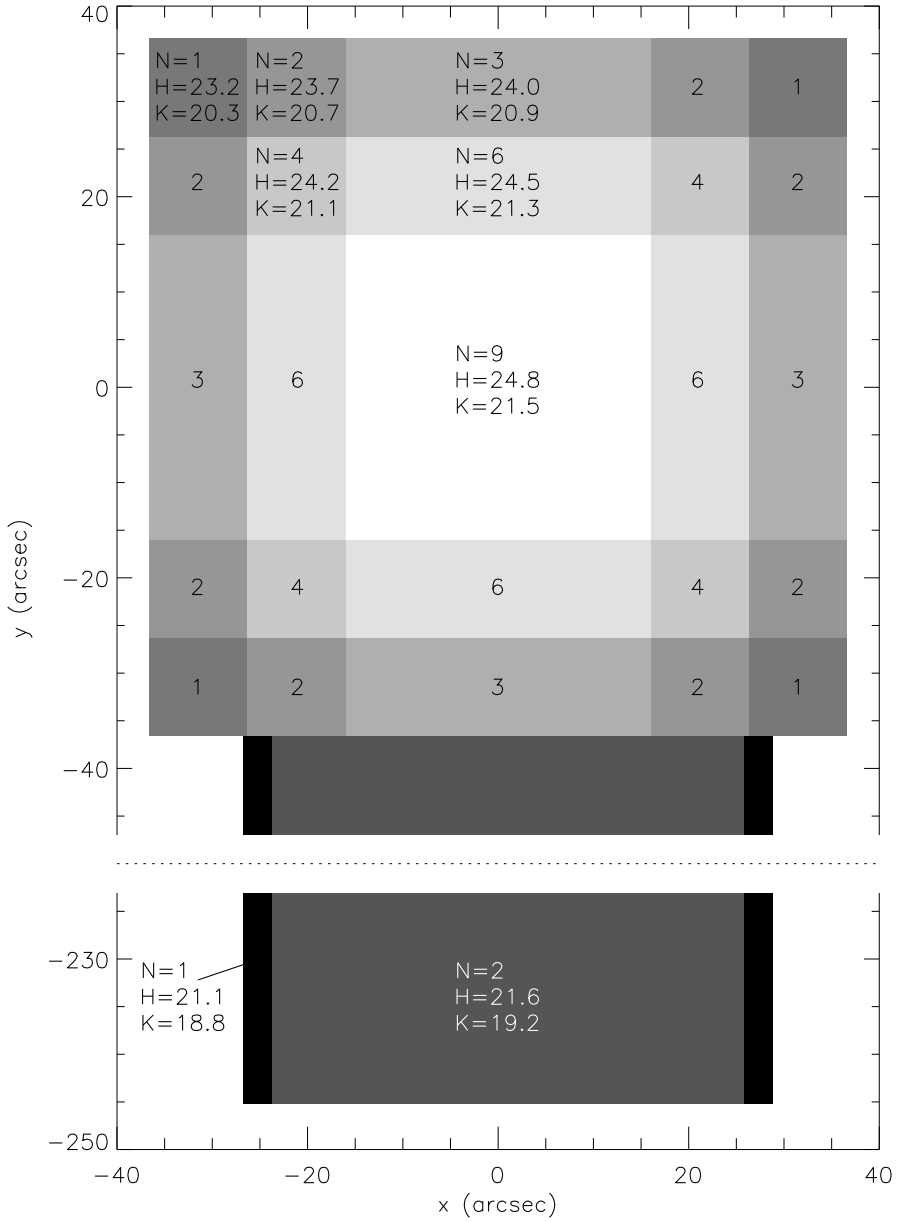

Fig. 2.2.— Diagram showing the spatially dependent limiting magnitudes (in the CIT system) for the NICMOS observations. The quantity N indicates the number of exposures taken of that region.

2.2.3 Keck Observations

Observations of B335 were made on 1998 July 10 using NIRC (Matthews & Soifer 1994) on the Keck I telescope. These observations were made for two reasons: (1) to obtain a better study of the stellar background population around B335, and (2) to transform the NICMOS F160W and F222M magnitudes to a standard system. The NIRC has 256×256 pixels with size $0\farcs15$, giving a $38\farcs4$ field of view. Each basic observation consisted of nine dithered 5 second integrations, in a 3×3 pattern with $3''$ offsets, which were mosaiced together. Observations were made with J, H, and K filters. The program had three parts: (1) nine images of the central region of B335, approximately mimicking the sub-images of the NICMOS central mosaic, (2) five images leading away from the center of B335, at each position of a NICMOS strip image, and (3) four additional fields $10'$ away from B335, to study the characteristics of the stellar background population. These regions are marked on Figure 2.1.

The data reduction and calibration was done in IRAF following the standard dark/flat/sky subtraction procedures, using a running flat. This procedure works well when the background emission does not change rapidly. For some periods during the observations, the sky emission in the H band did change relatively quickly, and the background subtraction for observations during these periods is not perfect. The typical seeing during the night was $0\farcs5$, though there were periods when it was better and also much worse.

Photometry

The majority of stars in the Keck images of B335 could be identified with reference to the NICMOS data, since the Keck images are all less deep than the NICMOS equivalents and the field of view slightly smaller. For the Keck fields not observed with NICMOS, all stars were again identified by visual inspection.

Photometry was performed for all non-saturated stars using the *apphot* package. Again, a series of increasing radial apertures was used for each star, and each aperture was used to calculate a magnitude. This approach allowed a confidence level in the measurement to be assigned to each star, based on whether the distribution of measurements from different apertures was consistent with the predicted uncertainty. If the spread of the various magnitudes was greater than 0.2 magnitudes, then the measurement was identified as low quality (18% of the stars detected at H and 17% of the stars detected at K). These low quality stars have point-spread-functions that differ from the norm, mainly from those periods of poor and varying seeing conditions. The instrumental magnitudes were transformed to the CIT system through observations of the HST infrared standards SJ9164 and SJ9182 (Persson et al. 1998) and the UKIRT standard FS35 (Casali & Hawarden 1992). The internal dispersion in the zero points measured for these stars was 0.02 magnitudes, and no atmospheric extinction correction could be discerned. The Keck photometry list contains a total of 297 stars detected at H, and 340 stars detected at K, in the overlap region between the Keck and NICMOS datasets.

The four Keck fields $10'$ away from B335 contain typically 100 detected stars per square

arcminute with H< 20. The four fields display uniform properties and no discernable reddening; the star counts in each image are identical to within Poisson errors, and the mean (H − K) color of the fields are all in the range 0.07 to 0.11, consistent with the intrinsic colors of giant and main sequence stars. A detailed study of the background stellar population is presented in Section 2.3.1. The limiting magnitudes of the Keck observations are approximately H=19.7 and K=19.6.

2.2.4 Transformation of NICMOS Magnitudes

For extinction calculations, the NICMOS F160W and F222M magnitudes are transformed to standard H and K magnitudes. Linear least squares fits (not including the lower quality Keck data) give slopes of −0.05 for (H − F160W) vs. F160W, −0.03 for (K − F222M) vs. F222M, and 0.99 for (H − K) vs. (F160W − F222M), where the formal uncertainties in the fitted slopes are $\sim$ 0.01. The formal uncertainties are underestimates of the true uncertainties since the magnitude comparison slopes are strongly biased by the few brightest stars, and the color comparison slope is biased by the few reddest stars. Experimentation with subsets of the stars resulted in variations in the fitted slopes at the 0.05 level. We conclude that these data provide no evidence for non-zero slopes or color terms in the transformation. We calculated constant offsets for the magnitude conversions for each filter, using a weighted mean of (H − F160W) and (K − F222M) values. The result is H = F160W + (0.035 $\pm$ 0.003), and K = F222M + (0.052 $\pm$ 0.003), where the uncertainties represent the standard error in the mean. Figure 2.3 shows the scatter plot of (H − K) vs. (F160W − F222M) with the derived color transformation superimposed. For the (H − K)

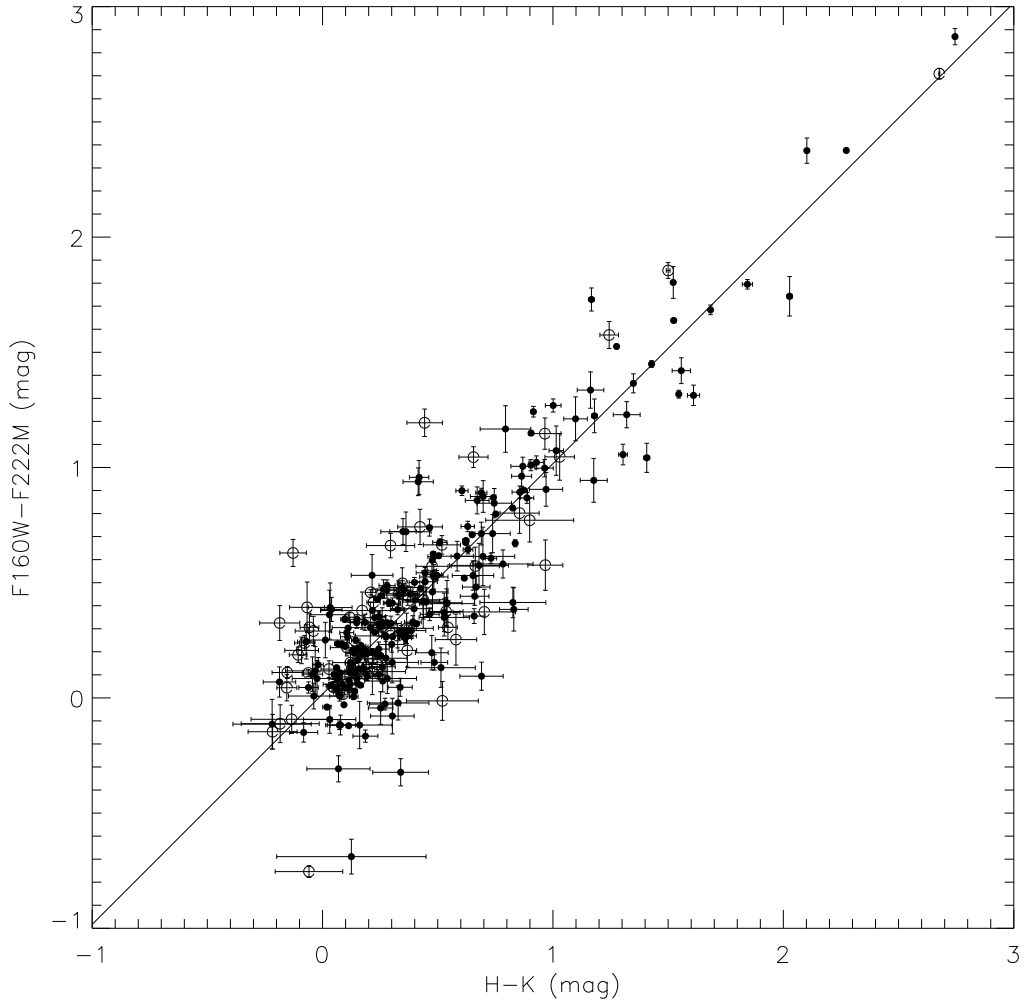

Fig. 2.3.— Plot of NICMOS (F160W − F222M) color against Keck (H − K) color. Stars for which the Keck H or K measurement are of lower quality are marked as open circles. Also plotted is the derived transformation: (F160W − F222M) = (H − K) + 0.017.

colors of interest, in the range 0 to 3, the differences between the two photometric systems are remarkably small.

Support for the accuracy of these transformations comes from published ground-based photometry of the one very bright star observed by Krügel et al. (1983), who measured Johnson H and K fluxes of 310 ± 25 mJy and 605 ± 45 mJy, which correspond to magnitudes of $H = 8.89 \pm 0.07$ and $K = 7.58 \pm 0.07$, and color $(H - K) = 1.31 \pm 0.11$. These values compare very favorably with the transformed NICMOS magnitudes of $H = 9.039 \pm 0.001$ and $K = 7.675 \pm 0.001$, and color $(H - K) = 1.364 \pm 0.001$. Note that systematic errors limit the accuracy of the NIC3 photometry to a few percent, and are not reflected in the random uncertainties quoted here.

2.3 Results and Analysis

2.3.1 Background Population Mean Color and Dispersion

To check the uniformity of the background stellar population, the starcounts and mean colors of the four Keck off fields were compared with those for the two NICMOS strip images furthest away from the center of B335. The colors in the different images are consistent within the observed dispersions. The fifth NICMOS strip field has a mean color and standard deviation of $\overline{H-K} = 0.17$, $\sigma(H-K) = 0.18$, very similar to that found for the combined Keck off-fields: $\overline{H-K} = 0.10$, $\sigma(H-K) = 0.13$. The fourth NICMOS strip field shows a slightly redder mean color ($\overline{H-K} = 0.26$) and higher dispersion ($\sigma(H-K) = 0.23$) than the other fields; most likely, this field is not far enough away from the center of B335 to

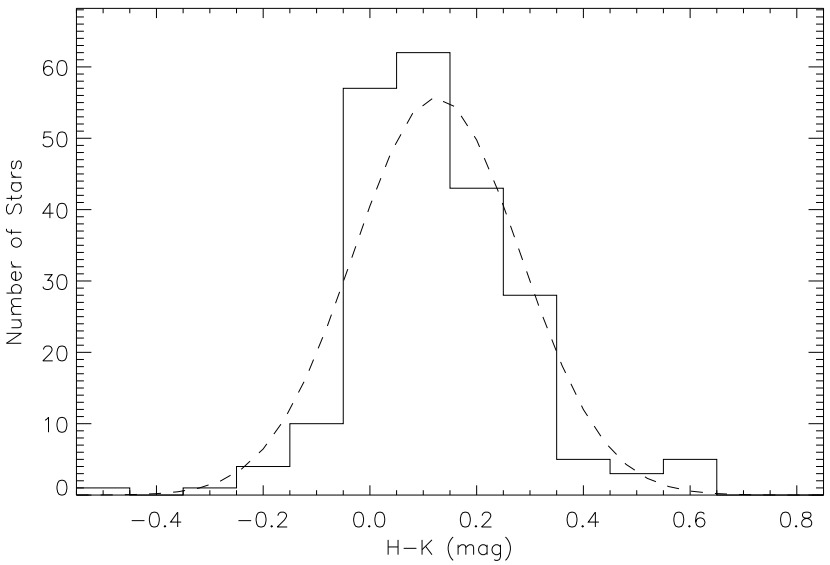

Fig. 2.4.— Histogram of the (H − K) colors of the background population, with bins of width 0.1 magnitudes. Also plotted is a Gaussian distribution with the same mean ($\overline{\mathrm{H-K}} = 0.13$) and standard deviation ($\sigma(\mathrm{H-K}) = 0.16$), and normalized so that the area under the curves are equal. Stars observed at Keck with lower quality photometry as discussed in the text are not included in this histogram.

be completely free of its extinction, and this field was excluded from our characterization of the background stellar population. Figure 2.4 presents a histogram of the (H − K) colors of the "background" stars in 0.1 magnitude bins (excluding the Keck stars with lower quality photometry). The (H − K) mean color is 0.13 magnitudes, with standard deviation 0.16 magnitudes. Also shown for comparison is a Gaussian distribution with the same mean and standard deviation (normalized so that the area under each curve is equal). A color-magnitude diagram constructed for this sample shows no sign of any important systematic trends, e.g. there is no tendency for fainter stars to be redder. The starcounts in the

fifth NICMOS strip field are indistinguishable from those in the Keck off-fields, taking into account the different size fields of view.

2.3.2 NICMOS Central Mosaic Image

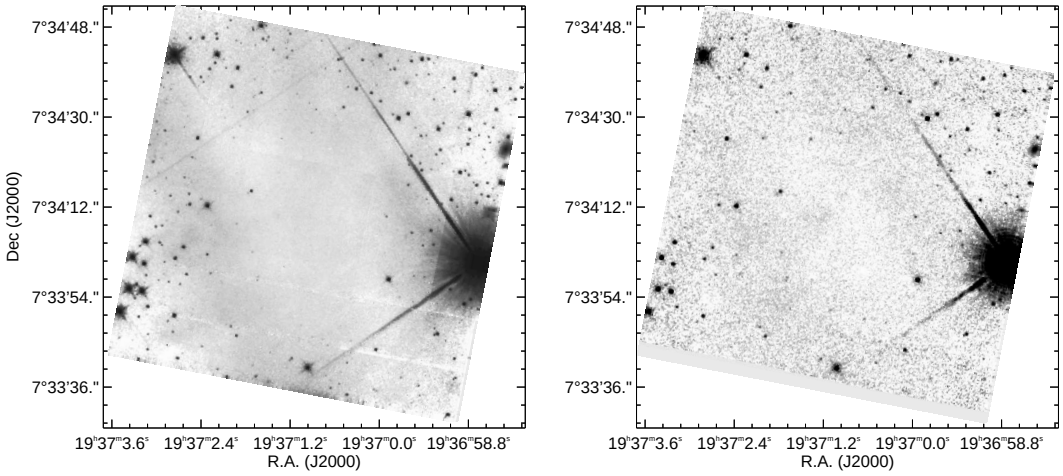

Fig. 2.5.— NICMOS F160W (left) and F222M (right) mosaic images of the central B335 region.

Figures 2.5 & 2.6 show the NICMOS F160W and F222M images of the B335 region. The central mosaic images in Figure 2.5 may be compared to H band and K band images of a smaller part of the central region of B335 obtained over three nights at Keck by Hodapp (1998) using NIRC. In the region of overlap, the F222M image shows the same stars as the K band image, but the overall sensitivity of the NICMOS image is better and the point-spread-function much sharper, leading to better separation of nearby stars. The F160W image shows many more stars than the corresponding H band image. In contrast with the ground-based data, essentially all stars detected with the F222M filter are also detected with

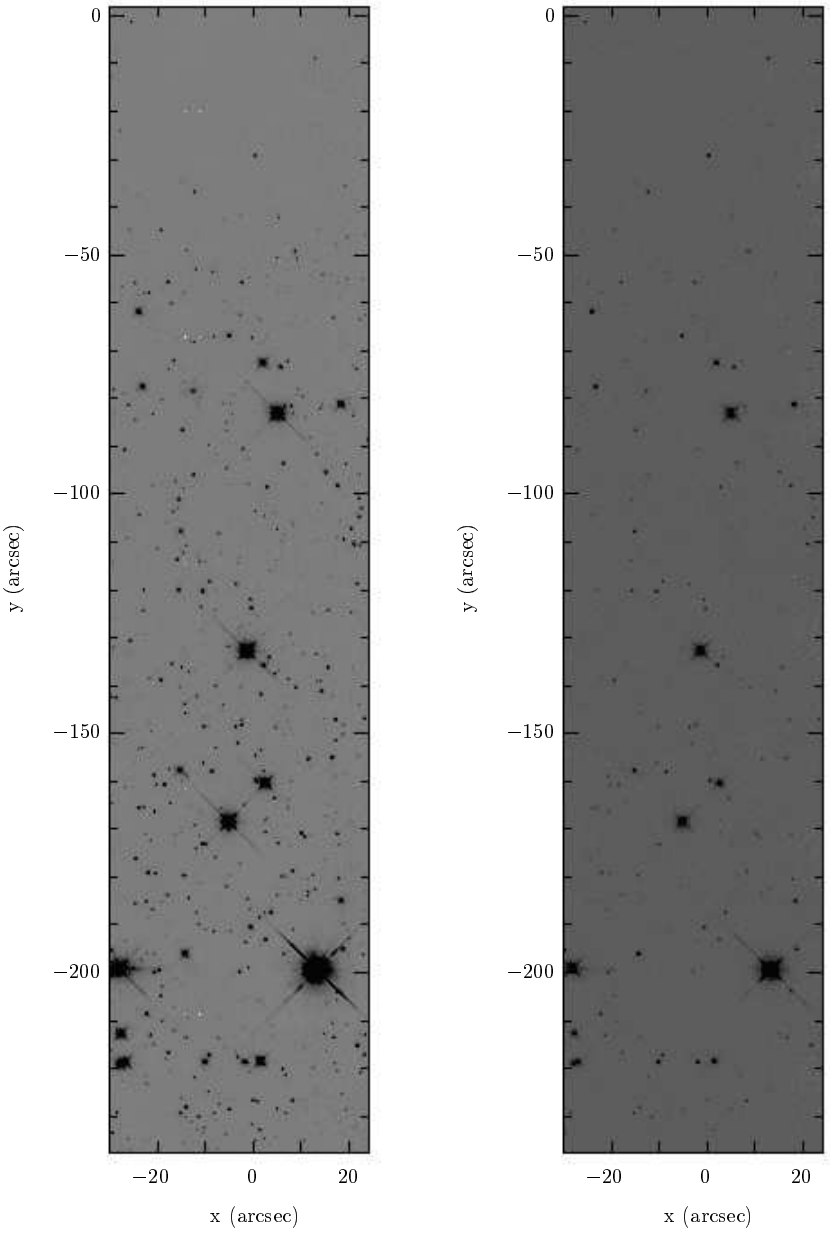

Fig. 2.6.— NICMOS F160W (left) and F222M (right) images of the strip leading off B335.

the F160W filter because of the low background and greater sensitivity of the space-borne NICMOS at the shorter wavelength.

Figure 2.7 conveys much of the information from the central mosaic of NICMOS observations. The left plot is a pseudo-image in that the two axes are spatial, the apparent brightness of a star determines its "size", and the value of its (H − K) color determines its "color". The right-hand plot displays the radial dependence of the (H − K) colors out to 180″ from the center. The origin in both plots is given by the position of the embedded young stellar object, as determined by interferometric observations of millimeter continuum emission (Wilner et al. 2000); the uncertainty in the registration of the NICMOS images and the millimeter peak is estimated to be about 1″. Based on an inspection of the extinctions, the stars in the right hand plot have been marked according to their spatial location: those that lie in the North or South quadrants are marked in red, and those that lie in the East or West quadrants are marked in blue (the quadrant boundaries are marked in the pseudo-image as dashed lines). Defining θ to be the angle subtended between the vector to a star and the axis of the outflow (which runs very close to east-west), this division may be expressed simply as $\theta > 45°$ or $\theta < 45°$. The NICMOS central mosaic image contains 239 stars detected at H, 121 stars detected at K, and 119 stars that are detected in both filters. The detected star closest to the embedded young stellar object is at 14″ radius. The reddest detected star is at 17″ radius and has an (H − K) color of 4.0, corresponding to over 60 magnitudes of equivalent visual extinction.

The major features of Figure 2.7 are: (1) a strong gradient in the (H − K) colors as one approaches the protostar; (2) fewer stars are detected close to the center, despite

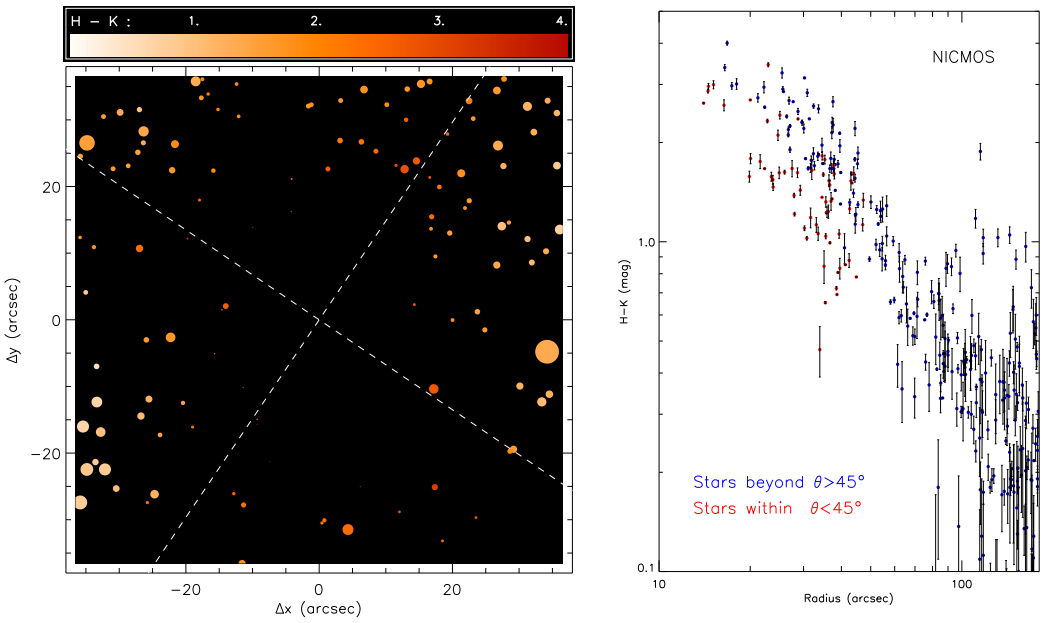

Fig. 2.7.— Left: Pseudo-image of the NICMOS mosaic: the axes are spatial, magnitude determines a star's "size", and (H − K) determines its color. The axes are in the frame of the NICMOS image. The mosaic contains 119 stars detected in both filters. The dashed line distinguishes the regions that are more than 45° from the outflow axis (the outflow axis has position angle roughly 100° in the pseudo-image). Right: (H − K) color against radius out to 180″ from the center of B335. There is a steep gradient towards the protostar location. The symbol color indicates whether the star lies within 45° of the outflow axis. The outer edge of B335 occurs at a radius of approximately 125″.

better sensitivity; (3) reddening of the stars turns off into background noise beyond the 125″ (0.15 pc) outer radius of dense gas determined from molecular line data (Zhou et al. 1990); (4) there is a marked asymmetry in the stellar colors associated with the bipolar outflow– stars viewed within $\sim 45°$ of the outflow axis have systematically lower colors; (5) the dispersion of the (H − K) colors at a given radius and in the quadrants away from the outflow is $\sim 20\% \times$ E(H − K) greater than that of the background population.

2.3.3 Theoretical Models of the B335 Density Distribution

We describe several theoretical models for the density distribution of B335 and evaluate the success of these models in light of the extinction data. The models considered are not meant to comprise an exhaustive list. They include the inside-out collapse models previously proposed for B335, Bonnor-Ebert spheres, and simple power law descriptions. We also discuss briefly the effects of the bipolar outflow and turbulent motions in B335.

Inside-Out Collapse Models

There is a substantial literature of theoretical work by Frank Shu and colleagues describing the density structure of collapsing dense cloud cores, starting from the initial condition of a singular isothermal sphere. Taking parameters appropriate for the B335 region, we briefly describe the pre-collapse state, the spherical inside-out collapse, and the modifications to spherical collapse expected for slow initial rotation or weak magnetic fields.

Pre-collapse Configuration: The initial state is that of a singular isothermal sphere; the density falls off as $\rho \propto r^{-2}$, where r is the radius, with the normalization of the density determined by the effective sound speed. For B335, Zhou et al. (1990) derive a value for the effective sound speed of $a = 0.23$ km s^{-1} from molecular line data, which corresponds to a kinetic temperature of 13 K. The static initial condition is therefore given by:

$$\rho_{\rm static}(r) = \frac{a^2}{2\pi G r^2} \tag{2.2}$$

$$= 1.33 \times 10^{-20}\ {\rm g\,cm^{-3}} \left(\frac{a}{0.23\,{\rm km\,s^{-1}}}\right)^2 \left(\frac{r}{0.1\,{\rm pc}}\right)^{-2} \tag{2.3}$$

$$n_{H_2}(r) = 2.80 \times 10^3\ {\rm cm^{-3}} \left(\frac{a}{0.23\,{\rm km\,s^{-1}}}\right)^2 \left(\frac{r}{0.1\,{\rm pc}}\right)^{-2}, \tag{2.4}$$

where the conversion to a molecular hydrogen number density assumes 0.7 for the the mass fraction in hydrogen.

Spherically Symmetric Collapse: The simplest scenario is the spherically symmetric collapse (Shu 1977). In this model, a spherical wave of collapse propagates outwards from the center at the effective sound speed. The radial distance that the wave has traveled, sometimes called the infall radius, is the only additional parameter that defines the density distribution. Inside the infall radius, conditions approach free fall, with the density taking the asymptotic form $\rho \propto r^{-3/2}$. By reproducing essential features of several molecular line profiles with this model, Zhou et al. (1993) claimed evidence for inside-out collapse in B335. Choi et al. (1995) made more detailed radiative transfer models to match the Zhou et al. (1993) observations of H_2CO and CS molecules, determining the infall radius to be 0.030 pc (25″). Note that this derived infall radius falls entirely within the deep central mosaic of NICMOS coverage.

Rotation: The effect of slow rotation on the collapse has been solved using a perturbative approach from the spherically symmetric case (Terebey, Shu & Cassen 1984). The result is a distortion to the shape of the collapse wave of order $4 \times 10^{-4}\,\tau^2$, where τ is the number of times that the cloud has rotated since collapse initiated (this is also equivalent to the ratio of the infall radius to the centrifugal radius). For B335, Frerking et al. (1987) found an angular velocity of 1.4×10^{-14} s^{-1} through C^{18}O observations. This indicates a value of $\tau^2 \sim 3 \times 10^{-3}$, and a distortion in the wave by only $\sim 10^{-6}$ — an entirely negligible effect. The density distribution is more strongly distorted, with the effect largest near the center of collapse. For radii greater than a tenth of the infall radius (i.e. $r \geq 2\farcs5$) — already well within the innermost radius where stars are detected — the correction is always less than of order τ^2, which is also completely negligible. Such slow rotation also has an unimportant effect on the model line profiles towards the center of B335 (Zhou 1995). We therefore do not include rotation in our models.

Magnetic Fields: The effect of a weak magnetic field on the inside-out collapse of a cloud has been studied by Galli & Shu (1993) and Li & Shu (1997). The collapse wavefront and the density distribution are again distorted, in a similar way to the rotational model. In the magnetic case, the parameter τ is given by the ratio of the infall radius to the magnetic radius:

$$R_m = \frac{2\,a^2}{B_0\,\sqrt{G}} \tag{2.5}$$

$$= 0.044\,\mathrm{pc}\,\left(\frac{a}{0.23\,\mathrm{km\,s^{-1}}}\right)^2\,\left(\frac{B_0}{30\,\mu\mathrm{G}}\right)^{-1} \tag{2.6}$$

Galli & Shu (1993) showed that the field effects only a small perturbation to the spherically symmetric solution outside a radius of $r \geq 0.2\,\tau^{4/3}\,R_{\mathrm{inf}}$. Figure 2.7 shows that variation in

color between the two spatial populations of stars can be as large as a factor of two, well beyond the infall radius of 25″ derived by Choi et al. (1995). Since this certainly cannot be construed as a "small perturbation" at these radii, we can place a lower limit on the magnetic field that would be needed to explain the asymmetry in the context of this model. Taking $r/R_{\rm inf} \simeq 1$, we find that:

$$B_0 \gtrsim 150 \left(\frac{a}{0.23\,{\rm km\,s^{-1}}}\right)^2 \left(\frac{R_{\rm inf}}{25''}\right)^{-1} \mu{\rm G} \tag{2.7}$$

Such a minimum magnetic field strength is implausibly large. For example, Crutcher & Troland (2000) measured a line-of-sight magnetic field of B $\sim$ 11 μG in the starless protostellar core L1544 using the Zeeman effect in lines of OH, and this is much higher than the typical upper limits found for other dark clouds (Crutcher et al. 1993). In this context, it therefore seems very unlikely that a magnetically modified inside-out collapse could be responsible for the large asymmetry observed in the B335 extinction data.

Bonnor-Ebert Models

Bonnor-Ebert models are pressure confined isothermal spheres, for which the solution remains physical at the origin (Ebert 1955, Bonnor 1956). In common with the singular isothermal sphere, the initial condition for inside-out collapse, they are solutions of a modified Lane-Emden equation (Chandrasekhar 1967):

$$\frac{1}{\xi^2}\frac{d}{d\xi}\left(\xi^2\frac{d\psi}{d\xi}\right) = \exp\left(-\psi\right) \,, \tag{2.8}$$

where $\xi = (r/R_0) = (r/a)\sqrt{4\pi G\rho_c}$ is the dimensionless radius, and $\psi(\xi) = -\ln(\rho/\rho_c)$ is a logarithmic density contrast, with ρ_c the (finite) central density. Unlike the singular

solution, the Bonnor-Ebert solutions do not diverge at the origin. Instead, the boundary conditions are that the function ψ and its first derivative are zero at the origin.

The above equation can be solved by division into two first order equations which can then be tackled simultaneously using numerical techniques (in our case a 4th order Runge-Cutta method). There is a family of solutions characterized by a single parameter — the dimensionless outer radius of the sphere, $\xi_{\rm max}$. For a given sound speed and a particular choice of the shape of the density curve (i.e. $\xi_{\rm max}$), there is one additional degree of freedom, the physical scale of the model. This additional degree of freedom may be removed by implementing an additional constraint, for example by fixing the outer radius, the total mass, or the external pressure.

Configurations with dimensionless outer radius $\xi_{\rm max} > 6.5$ are unstable to gravitational collapse (Bonnor 1956). The gravitational collapse of Bonnor-Ebert spheres has been studied numerically by Foster & Chevalier (1993). They find that the flow asymptotically approaches the Larson-Penston solution at the origin at the time of and prior to the formation of a central core, but emphasize that these large early accretion rates last for a very short time. If the cloud is initially very centrally condensed (i.e. $\xi_{\rm max} \gg 6.5$) the later stages of infall closely resemble Shu's inside-out collapse of a singular isothermal sphere.

Recently, Alves, Lada & Lada (2001) used the color excess method to study B68, a starless core, with data from the ESO VLT. The B68 system is much less centrally condensed than B335, and has much lower column density at the center (only about 30 magnitudes of equivalent visual extinction). The Alves et al. (2001) extinction map of B68 suggests that the density structure is well described by a Bonnor-Ebert sphere with dimensionless

outer radius slightly in excess of critical: $\xi_{max} = 6.9 \pm 0.2$. Although the B335 core is at a much later evolutionary stage than B68, with an embedded protostar, we consider the Bonnor-Ebert sphere since it describes B68 so successfully.

Bipolar Outflow and Turbulence

The outflows from young stellar objects can have a substantial impact on their surroundings. A bipolar outflow in B335 was discovered in CO by Frerking & Langer (1982). Later studies in various tracers by Cabrit, Goldsmith & Snell (1988), Hirano et al. (1988, 1992), Chandler & Sargent (1993), and Wilner et al. (2000) show that on arcsecond to arcminute scales, the outflow is well collimated with a semi-opening angle of about $25 \pm 5°$, and with the axis lying very nearly in the plane of the sky. The outflow orientation is close to east-west, with position angle roughly 100° in the coordinate system of the NICMOS images. Inside the region affected by the outflow, the density structure is modified as the core material is swept out by the flow, but the exact form of the density field associated with the outflow is not known.

The bipolar outflow may be an important driver of turbulent motions. Zhou et al. (1990) determined a turbulent component to the effective sound speed in B335 of 0.08 km s^{-1}. Coupling of the velocity and density fields via the continuity equation suggests that the perturbations to the velocity field should induce density contrast perturbations, i.e. $\delta \simeq [(1/3) < v/a >^2]^{1/2} \simeq 0.2$. The resulting perturbations to the column densities (and extinctions) will depend on the size scale of the velocity and density field perturbations. The perturbations to the column density will be largest when the size scale is a factor of a

few smaller than the dense core. The extinction map is consistent with this possibility since the observed colors of neighboring stars are generally very similar, yet there exists a $\sim 20\%$ dispersion for stars that are not neighbors but are located at similar radial distances from the protostar (see Figure 2.7). The effect of the column density perturbations are inevitably reduced by integration along the line-of-sight, but the observed residual turbulence most likely contributes significantly to the dispersion in the observed colors.

2.3.4 Fitting Model Parameters and Evaluating Fit Quality

We evaluate the goodness of fit for these various model density distributions by calculating a reduced χ^2, defined as:

$$\chi^2_\nu = \frac{1}{N-m} \sum \left(\frac{\mathrm{E(H-K)}_i^{\mathrm{NIC}} - \mathrm{E(H-K)}_i^{\mathrm{model}}}{\sigma_i^{\mathrm{NIC}}} \right)^2 , \tag{2.9}$$

where m is the number of free parameters in the model being fitted, and the sum extends over a particular subset of N stars taken from the total number detected in both NICMOS filters. The values of the observed color excess $\mathrm{E(H-K)}_i^{\mathrm{NIC}}$ and the uncertainty σ_i^{NIC} are calculated using the properties of the unreddened stellar background population (see Section 2.3.1, and Figure 2.4), assuming each star to have an intrinsic color of $(\overline{\mathrm{H-K}})_{\mathrm{BG}} = 0.13$, with an uncertainty of $\sigma_{\mathrm{BG}} = 0.16$:

$$\begin{aligned} \mathrm{E(H-K)}_i^{\mathrm{NIC}} &= (\mathrm{H-K})_i^{\mathrm{NIC}} - (\overline{\mathrm{H-K}})_{\mathrm{BG}} \\ &= (\mathrm{H-K})_i^{\mathrm{NIC}} - 0.13 , \end{aligned} \tag{2.10}$$

$$\begin{aligned} \sigma_i^{\mathrm{NIC}} &= \sqrt{\sigma_i^2 + \sigma_{\mathrm{BG}}^2} \\ &= \sqrt{\sigma_i^2 + 0.16^2} , \end{aligned} \tag{2.11}$$

where σ_i is the uncertainty in the observed (H − K) color of a given star. This procedure implicitly assumes that the photometric errors (σ_i) and the intrinsic (H − K) colors both have Gaussian distributions. Though the latter condition is not strictly true, Monte Carlo trials show that the χ^2_ν values calculated with the above recipe agree very closely with those produced when the intrinsic color of each star is instead chosen randomly from the Gaussian distribution with the same mean and standard deviation as the sample of background colors. We conclude that the results of the fitting are not sensitive to this approximation.

Since the models are in general non-linear in the fitting parameters, we analyze the uncertainty in the best-fit model parameters using a Monte Carlo technique known as the *Bootstrap* method (Press et al. 1992). To describe the method, let us represent the dataset that is being used in the fitting by S. The first step is to construct a new dataset of equal size S', by randomly selecting N times from the original dataset. This new sample is then analyzed in the same way as the original dataset, and the fitted model parameters recorded. This process is then repeated n times, where n is sufficiently large that the resulting distribution of best-fit model parameters is insensitive to its exact value (for our models, typically $n = 200$). The standard deviation of this distribution provides an estimate for the uncertainty of the parameters that best fit the original dataset. Table 2.1 summarizes the results from the various χ^2 analyses and these results are discussed below. Figure 2.8 shows a schematic diagram of the spatial coverage of the NICMOS observations relative to the important size scales in B335.

Table 2.1. Summary of the χ^2 Analyses Data

Fit	Model Density Distribution	Fit Region	Stars	Fitted Model Parameter(s)	χ^2_ν
A	Scaled Power Law: $\rho \propto r^{-p}$	$r < 100$" ; $\theta > 45°$	146	$p = 1.91 \pm 0.07$	3.37
B	Scaled Infall: $\rho = \mathcal{F}\rho_{\rm Shu}(r, R_{\rm inf})$	$r < 100$" ; $\theta > 45°$	146	$R_{\rm inf} = 28 \pm 3$" ; $\mathcal{F} = 5.25 \pm 0.13$	3.10
C	Scaled Bonnor-Ebert ($R = 125''$)	$r < 100$" ; $\theta > 45°$	146	$\xi_{\rm max} = 12.5 \pm 2.6$; $\mathcal{F} = 3.42 \pm 0.10$	2.93
D	Scaled Infall, Hollow-Cone Outflow	$r < 100$"	209	$R_{\rm inf} = 30 \pm 3$" ; $\alpha = 41 \pm 4°$; $\mathcal{F} = 5.25 \pm 0.13$	4.02
E	As Fit D with 20% Dispersion	$r < 100$"	209	$R_{\rm inf} = 26 \pm 3$" ; $\alpha = 41 \pm 2°$; $\mathcal{F} = 4.77 \pm 0.14$	1.04

Note. — For each Fit, we consider only stars within $100''$ of the protostar location, to avoid noise-related issues near the edge of the cloud. Fits A–C consider only the regions that are well removed from the outflow, while Fits D & E are for the entire dataset within 100". Fit A is for a general power law density distribution. The remaining Fits use the Zhou et al. (1990) effective sound speed ($a = 0.23$ km s^{-1}), with a free scaling applied to the predicted color excess, representing the many potential sources of systematic error in the conversion from color excess to density. Fit B uses the Shu inside-out collapse model, and Fit C uses a Bonnor-Ebert sphere. Fit D uses a combination of an infalling model with a model outflow that empties a cone of constant opening angle. Fit E uses the same model, but includes an extra dispersion in E(H − K) to account for extra small scale structure in the cloud.

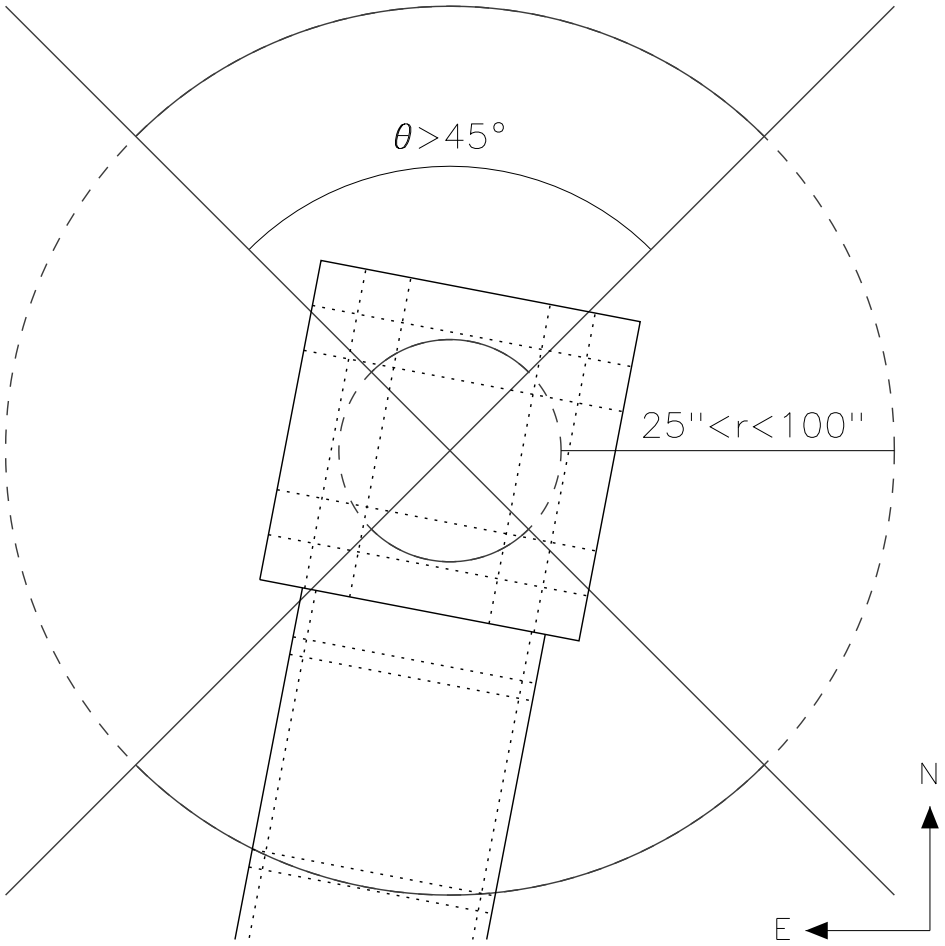

Fig. 2.8.— Schematic diagram showing the scale and coverage of the NICMOS observations relative to important scales of B335. The region beyond 45° from the outflow axis is marked.

2.3.5 Excluding the Outflow (Fits A, B & C)

The asymmetry in the observed colors appears to be associated with the bipolar outflow. Since we do not know from theory the effect of the outflow on the material distribution, we initially restrict attention to the quadrants that are located away from the flow, $\theta > 45°$, where θ is the angle subtended between the vector to a star and the axis of the outflow. To avoid noise near the boundary of the globule, we also restrict the fitting region to $r < 100''$. In Fit A of Table 2.1, we use a power law model for the density distribution. In Fit B we use the Shu inside-out collapse model, and in Fit C we use a Bonnor-Ebert sphere.

The best fitting single power law model (Fit A) to the dense core region unaffected by the outflow has an index of $p = 1.91 \pm 0.07$. This value is well matched to the r^{-2} envelope of the isothermal sphere that represents the initial condition of the inside-out theory. The inside-out collapse solution (Fit B), which is similar to a broken power law with fixed indices, provides a somewhat better description than can a single power law model with arbitrary index. Remarkably, the fitted infall radius of $R_{\rm inf} = 28 \pm 3\,''$ (0.034 ± 0.004 pc) agrees within uncertainties with those calculated by Zhou et al. (1993) and Choi et al. (1995) by modeling molecular line profiles. That the minimum χ^2_ν value for these fits are near 3 instead of unity reflects the $\sim 20\% \times {\rm E(H-K)}$ greater dispersion in the observed colors than in the intrinsic colors of the background stars.

A Bonnor-Ebert sphere provides an equally good description of the density structure in B335 (Fit C). Figure 2.9 shows a comparison of the (H − K) radial profiles predicted by the Bonnor-Ebert sphere in Fit C, and the inside-out collapse model in Fit B. The plot

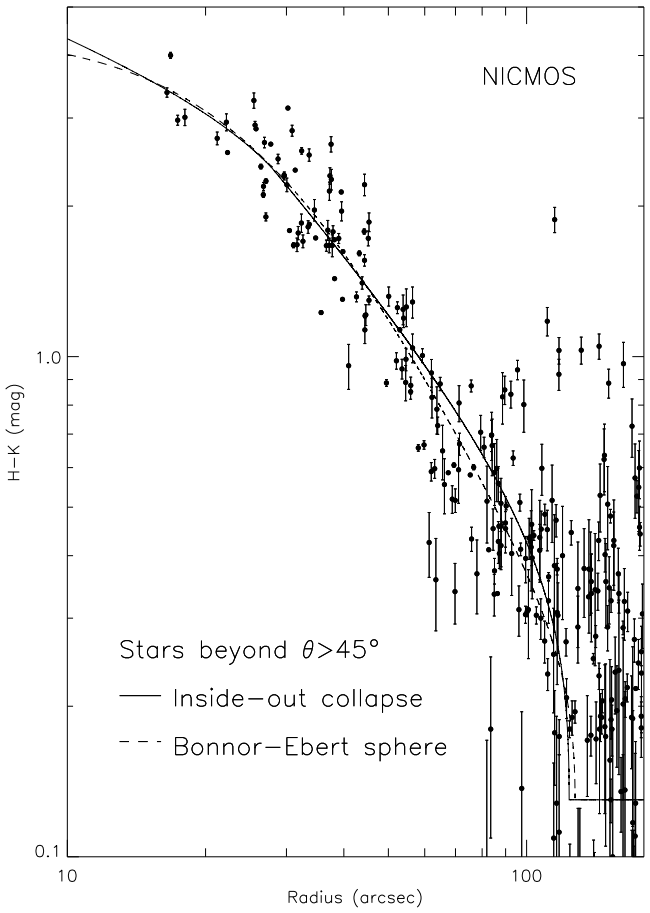

Fig. 2.9.— (H − K) vs. radius for the NICMOS stars beyond 45° from the outflow axis. Overplotted are predicted curves for the best fitting infall model (Fit B) and the unstable Bonnor-Ebert sphere (Fit C), assuming a constant background color of 0.13. The two curves are indistinguishable over the range in radius where there are stars to fit.

shows that the two models are practically indistinguishable over the range in radius where there are stars to fit (14″–100″). At large radii, the Bonnor-Ebert solution has slope close to a power law index of 2.0, and at smaller radii, the slope flattens. In effect, the best fit Bonnor-Ebert sphere is one that mimics the inside-out collapse solution over the range in radius for which there is data. The models diverge only at such small radii that extinction data of sufficient depth to discriminate between them is currently impossible to obtain. One discriminant may be sensitive, high resolution observations of dust emission, which is strongest at these small radii where extinction data is lacking. Regardless, the value of $\xi_{max} = 12.5 \pm 2.6$ for the best fit Bonnor-Ebert sphere is well in excess of the critical value of 6.5, and it is therefore an unstable configuration that should undergo gravitational collapse similar to Shu's inside-out solution (Foster & Chevalier 1993).

2.3.6 Modeling the Outflow

The simplest model we imagine to simulate the effects of the bipolar outflow on B335 is to assume that the outflow has completely cleared out the dense material in a bipolar cone of constant opening angle. Figure 2.10 shows the radial behavior of the (H − K) colors from simulated observations we have made of an infalling model for four different values of the model outflow semi-opening angle α. (The appendix describes how the simulations are constructed.) Stars viewed through the model outflow cone are marked in red, and those not viewed through the outflow cone are marked in blue. The density distribution for $\theta > \alpha$ in each of the simulations is the infalling model that best fits the E(H − K) data beyond 45° from the outflow axis (Fit B). As the model opening angle increases, the stars begin to

separate into two distinct populations. Two effects are evident as the angle increases: (1) the population of detected stars with reduced colors becomes larger, and (2) the separation in the colors of the two populations grows larger. Manifest in the simulation with the largest opening angle (55°) is that the first effect is not only caused by the outflow cone occupying a larger fraction of the sky, but is also due to there being less column density for lines-of-sight passing through the cone, which allows a greater number of the background stars to be detected. Comparison of the radial behavior of the (H – K) colors in these simulations with the observations in Figure 2.7 shows that these simple models successfully reproduce the major features. The extent of the spread between the colors of the two populations of stars in the NICMOS data seems to be reproduced best by the simulations with semi-opening angles of 35° and 45°. These angles also roughly reproduce the observed number of stars with significantly reduced colors.

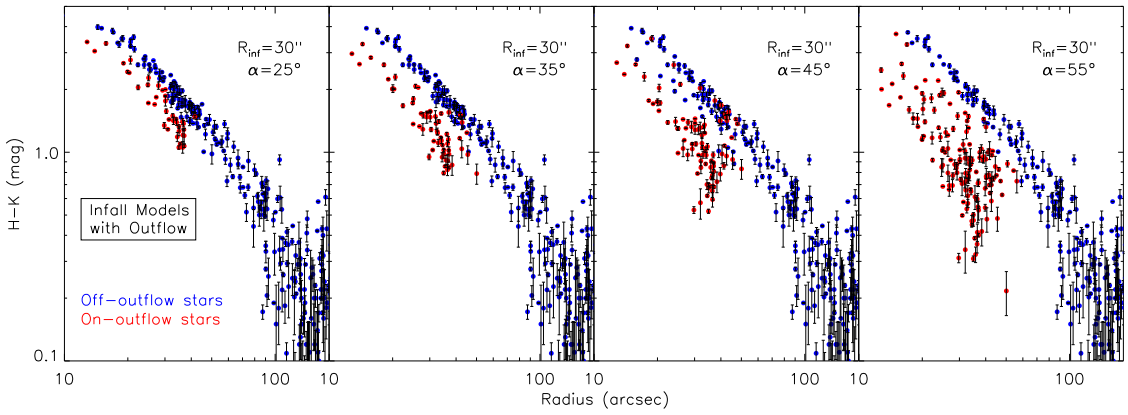

Fig. 2.10.— (H – K) vs. radius for simulations of an infalling model with outflow cones of various outflow semi-opening angles, α.

2.3.7 Including the Outflow (Fits D & E)

The simple hollow cone model of the bipolar outflow allows the stars viewed closer to the outflow axis to be included in the χ^2 analyses. The fact that the predicted (H − K) colors are a sensitive function of the model outflow opening angle means that we are able to fit for the opening angle of the flow.

In both Fits D & E, we fit for the entire region within $r < 100''$, with a model which has both the infall radius and outflow opening angle as free parameters, and with the color excess normalization for each model chosen to minimize the χ^2_ν in the region beyond 45° from the outflow axis (as in Fit B). The only difference between Fit D and Fit E is that Fit E includes an extra $20\% \times \mathrm{E(H-K)}$ dispersion term in σ_i^{NIC} to account for additional structure in the cloud, perhaps from the residual turbulent fluctuations. Table 2.1 lists the best-fit parameters for Fit D and Fit E, and they are nearly identical. In both Fits D & E, χ^2_ν is essentially an independent function of the infall radius and the outflow opening angle. Figure 2.11 shows a contour plot of the surface of χ^2_ν for Fit D. The minimized value of χ^2_ν is 4.02, with fitted infall radius $R_{\mathrm{inf}} = 30 \pm 3''$ $(0.036 \pm 0.004\,\mathrm{pc})$ and outflow semi-opening angle $\alpha = 41 \pm 4°$. For Fit E, the contour plots and fitted parameters are essentially identical — infall radius $R_{\mathrm{inf}} = 26 \pm 3''$ $(0.031 \pm 0.004\,\mathrm{pc})$ and outflow semi-opening angle $\alpha = 41 \pm 2°$ — but the minimized χ^2_ν is $\simeq 1$ due to the extra dispersion. That the two fits agree so closely, particularly with regard to the infall radius, is interesting. The extra dispersion in Fit E reduces the weight of the most reddened (and most central) stars, which inevitably are those that constrain the fitting of the infall radius.

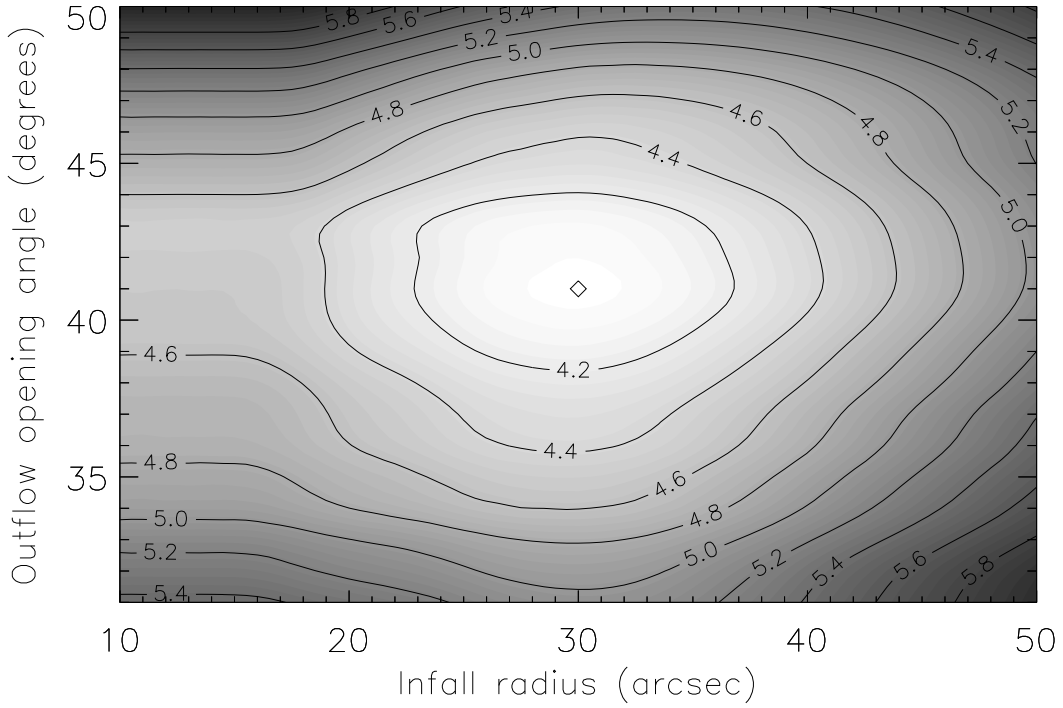

Fig. 2.11.— Contours of the surface of χ^2_ν for models with both infall and outflow, where the outflow has been assumed to clear out a cone of opening angle (α). The minimum in the reduced χ^2 is 4.02 and corresponds to fitted parameters of $R_{\rm inf} = 30 \pm 3''$ (0.034 ± 0.04 pc at a distance of 250 pc), and $\alpha = 41 \pm 4°$. The position of the fitted paramters is marked with a diamond. The best fitting model is labelled Fit D in Table 2.1.

The composite model with infall and bipolar outflow provides a consistent description of the density structure of B335. When the regions affected by the outflow are excluded from consideration, the inside-out collapse solution provided a good description of the data. Modeling the outflow as a hollowed-out bipolar cone allows inclusion of the stars from the

outflow region in the χ^2 analysis. Despite the obvious crudeness of this model for the outflow, the fits to the entire dataset (Fits D & E) constrain both the infall radius and outflow opening angle, and the fitted infall radii are entirely consistent with our earlier determination (Fit B) and with the values determined by molecular line studies. The fitted opening angle of the outflow is somewhat larger than indicated in studies of high velocity CO emission. Examination of the CO velocity structure (e.g. Hirano et al. 1988, 1992) suggests that the flow is more collimated at higher velocities, and that the opening angles dervied from CO must be lower limits since the low velocity outflow becomes confused with the ambient globule emission (and is resolved out by interferometers). This effect may explain why the opening angle appears wider in extinction than in CO emission. Of course, the one parameter model fitted here simply may not provide an adequate description of the outflow geometry at this level of detail.

Figure 2.12 presents a simulation of the models for Fit D and Fit E to afford another way to examine the success of these models, as well as the differences between them (the appendix describes the detailed recipe for constructing these simulations). The model for Fit D has an infall radius of $30''$ and an outflow opening angle of 41° (the normalization of the color excess is matched to the data by the χ^2 analysis). This model reproduces the gross structure of the NICMOS data very successfully. However, the radial plot shows that the dispersion in the $(H-K)$ colors at a given radius in the simulation is clearly significantly less than in the observations. The model for Fit E is nearly identical to Fit D except that the color excess has been multiplied by a Gaussian random variable with mean of unity and standard deviation 20%. The simulated data from the model for Fit E, with this additional

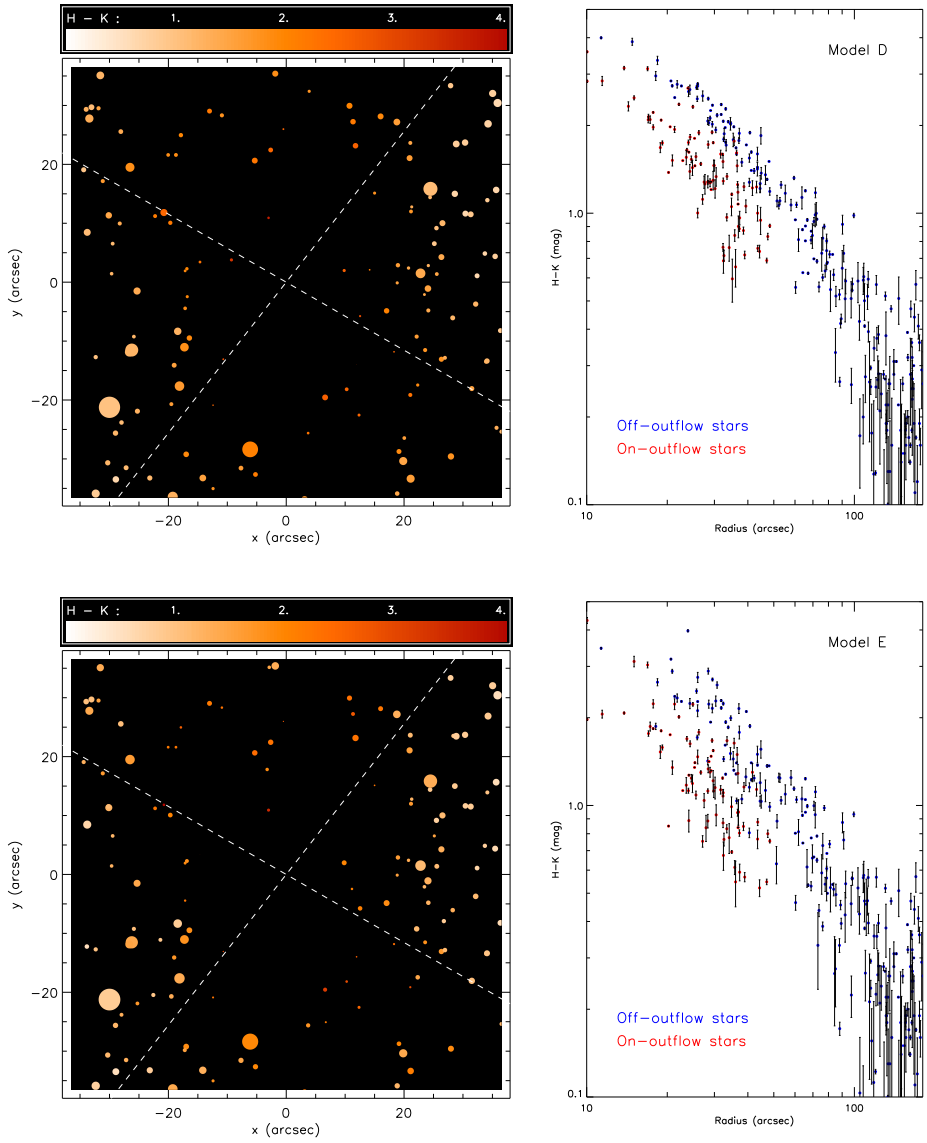

Fig. 2.12.— A simulation of the models of Fit D (Top) and Fit E (Bottom). For each model: (Left) Pseudo-image of the simulated NICMOS mosaic image; (Right) (H − K) color vs. radius out to 180″ from the center.

dispersion to mimic the effects of residual turbulence, compares much more favorably with the observations in Figure 2.7.

2.3.8 The Scaling Factor

So far, we have been concerned only with the *shape* of the density profile and have ignored the free scaling factor applied to the color excess predicted by the various models during the fitting. For both the inside-out collapse models and the Bonnor-Ebert spheres, the normalization of the density distribution is entirely determined by the effective sound speed, measured to be 0.23 km s^{-1} (Zhou et al. 1990). This measurement, together with the distance to the cloud, gas-to-dust ratio, and near-infrared reddening law, make a unique prediction for the color excess normalization in each model. As listed in Table 2.1, a scaling factor $\mathcal{F} \sim 3$–5 is required to match the models with the observed color excess. Figure 2.13 shows a simulation of the spherically symmetric inside-out collapse model with the effective sound speed of 0.23 km s^{-1}, the standard distance of 250 pc (Tomita et al. 1979), and the infall radius of 25″ derived by Choi et al. (1995). The simulation demonstrates the extent to which the model underestimates the observed reddening and extinction in B335. If this model were correct, then the NICMOS observations would have been sufficiently deep to see right through the center of the cloud, and the number of stars detected would have been far greater than observed. This therefore leads to the question: if the inside-out collapse model or the Bonnor-Ebert sphere model is correct, then what explains the need for this large scaling factor between the predicted extinction and the measured values?

The first possibility to consider is that the effective sound speed in B335 has been

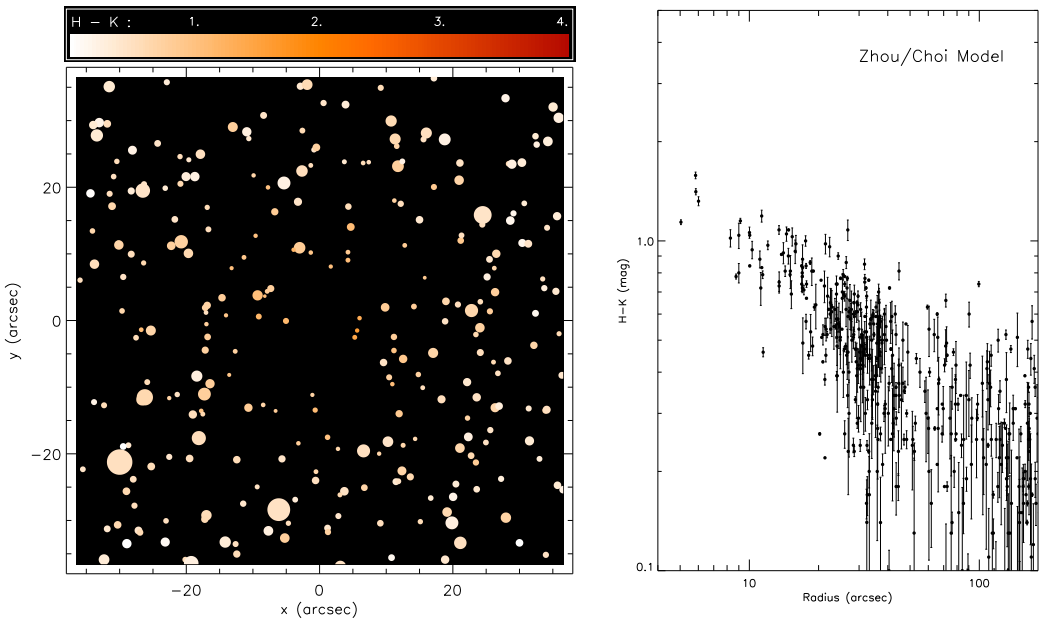

Fig. 2.13.— A simulation of the spherically symmetric inside-out collapse model with infall radius $25''$ (Choi et al. 1995), and normalization determined by the sound speed of $a = 0.23$ km s^{-1} (Zhou et al. 1990) and standard distance of 250 pc (Tomita et al. 1979). Left: Pseudo-image of the simulated NICMOS mosaic image. Right: (H − K) color vs. radius out to $180''$ from the center.

underestimated. To account for the $\mathcal{F} \sim 3$–5 by a larger kinetic temperature in the initial state seems implausible — a temperature of $T \simeq 40$–60 K would be needed. Multi-transition observations of NH_3 show that the bulk of the dense gas in B335 has a kinetic temperature of 10–12 K (Menten et al. 1984), consistent with a balance between heating and cooling processes. To account for the factor with non-thermal motions also seems implausible, given the measured widths of molecular lines. A non-thermal contribution of $v_{\rm turb} \simeq 0.35$–0.45 km s^{-1} would be required, which is clearly at odds with a multitude of molecular

line data. For example, Zhou et al. (1990) used observations of H_2CO to determine a small turbulent contribution of $v_{\rm turb} = 0.085$ km s^{-1} to the thermal sound speed. Similar results from a variety of different molecules are documented by Menten et al. (1984) and Frerking, Langer & Wilson (1987). One might envision a form of non-thermal support that is not reflected in the observed molecular line-widths, perhaps because of a special viewing geometry. If magnetic support were primarily from a static field and not waves, and this field were oriented so that the motions were not observable along the line-of-sight, then it would be effectively undetectable. Although such a special situation seems contrived and unlikely, the orientation of B335 is special in that the outflow lies close to the plane of the sky, which may make such a configuration more plausible.

Another possibility that affects the overall scaling lies in the outer boundary, i.e. where the cloud ends. Zhou et al. (1990) calculated the mass of B335 using an outer radius of 0.15 pc based on their radio map and the 250 pc distance estimate. The molecular line profiles of dense gas tracers are not particularly sensitive to this assumption. We have adopted this value for the outer radius throughout the extinction modeling. Indeed, the column densities are also insensitive to this assumption since the density falls off steeply with radius. For a star at the infall radius of the best-fitting inside-out collapse model (Fit B), doubling the outer radius of the cloud increases the predicted extinction by only 7.5%, which is an unimportant amount with respect to the derived scaling factors.

An overestimate of the distance to B335 would also result in predicted column densities that are too small. This distance uncertainty may be the dominant source of systematic error in the study. The distance of 250 pc was adopted from optical measurements of stellar

reddening versus distance by Tomita et al. (1979), and this distance is uncertain at the 50% level. If B335 were closer, then the extinction would be larger at the same angular radius. To account for the full scaling factor would require that the distance be $\sim$ 3–5 times closer, only about 50–80 pc, which seems unreasonable. Also, for a given level of observed extinction, the inferred mass of the globule is proportional to the square of its distance (since the angle subtended by B335 is fixed). For the outer boundary assumption of Zhou et al. (1990), the mass inferred from our extinction data is

$$M_{\rm B335} \simeq 14 \left(\frac{d}{250{\rm pc}}\right)^2 {\rm M}_\odot \ . \tag{2.12}$$

The 14 $M_\odot$ for a distance of 250 pc may be large for a small globule, but reducing the distance by the whole scaling factor lowers the mass to less than 1 $M_\odot$ for the inside-out collapse model, and a little over 1 $M_\odot$ for the Bonnor-Ebert sphere. This seems small given that the globule must be forming a star with a substantial fraction of a solar mass, and losing a lot of mass through outflow in the process. Furthermore, in the context of the inside-out collapse model, a reduction in the distance also results in a smaller mass for the protostellar core, as well as a shorter time since the onset of collapse (both are proportional to the distance for a given sound speed and infall radius). In short, a closer distance for B335 would ameliorate the discrepancy between the observed and predicted extinction, but it is not clear if this could account for the entire difference.

A final uncertainty is the conversion from column density to color excess using the gas-to-dust ratio and reddening law. Significant variations in the reddening law have not been observed, and they are unlikely to explain much of the observed discrepancy in the color excess (although we briefly return to this point in the appendix). By contrast, the gas-to-

dust ratio has been observed to vary in the Galaxy, with variations of ~ 2 not uncommon along different lines of sight (Bohlin et al. 1978). If the gas-to-dust ratio in B335 were lower than the standard value for the interstellar medium, or the reddening law steeper, then this would cause us to underestimate the extinction. Potentially, the full scaling factor could be accounted for by this uncertainty, or perhaps by some combination of a closer distance and a modified gas-to-dust ratio. For example, if the true distance to B335 were actually 100 pc, and the gas-to-dust ratio were about one half of the standard value (i.e. $R = 1 \times 10^{21}\,\mathrm{cm}^{-2}\,/\mathrm{mag}$), then these two factors would fully account for the discrepancy between observed extinction and the predictions of either model, and also give a reasonable mass for the globule of $M \simeq 2\ \mathrm{M}_{\odot}$. If molecular hydrogen were to deplete onto dust grains, this could cause such a decrease in the gas-to-dust ratio at high density. However, H_2 is not thought to undergo significant freeze-out in this way (Sandford & Allamandola 1993), and a decrease in the gas-to-dust ratio is at odds with evidence that suggests an increase in high extinction regions (e.g. Bohlin et al. 1978, de Geus & Burton 1991, and Ciolek & Mouschovias 1996).

2.3.9 Comparison with Dust Emission Studies

The density distribution in protostellar cores may also be studied through dust emission. If the emission is observed at long enough wavelength that the Rayleigh-Jeans approximation applies, then, in the optically thin regime, the intensity at impact parameter b is proportional to the integral along the line-of-sight of the product of the density and the temperature. Assuming that the intensity, temperature and density obey power law distri-

butions in radius, then the power law index of the density distribution $\rho \propto r^{-p}$ is simply given by $p = m + 1 - q$, where m is the observed power law index of the intensity profile, and q the power law index of the temperature profile. The mass may also be derived from the radial intensity distribution, given an assumed mass opacity. Unfortunately, the mass opacity of dust at millimeter and submillimeter wavelengths is uncertain, by a factor of five or more (Ossenkopf & Henning 1994).

For B335, dust emission at submillimeter and millimeter wavelengths has been studied recently by Shirley et al. (2000) and Motte & André (2001). Shirley et al. (2000) constructed images at 850 μm and 450 μm at resolutions of $15''$ and $8''$, respectively, using SCUBA at the JCMT. At both wavelengths, these observations are sensitive to emission out to an angular radius of roughly $52''$. They adopt a temperature profile with power law index $q = 0.4$ for a region where the envelope is optically thin to the bulk of the infrared radiation (e.g. Emerson 1988; Butner et al. 1990). They fit the circularly averaged maps at each wavelength, extending from inner cutoffs at angular radii of $24''$ for the 850 μm profile and $12''$ for the 450 μm profile. They derive power law indices of $p = 1.74 \pm 0.4$ and $p = 1.65 \pm 0.17$ from the 850 μm and 450 μm emission, respectively. They estimate a mass for B335 of 1.2 $M_\odot$ using the total 850 μm flux in a $120''$ area and assuming a sphere of constant density. Motte and André (2001) constructed a 1.3 mm continuum image of B335 with $11''$ resolution using the IRAM 30m telescope, detecting emission out to an angular radius of $120''$. They adopt an isothermal temperature distribution and calculate a density power law index of $p = 2.2 \pm 0.4$. In this model, the total mass is $2.5\,M_\odot$. They note an asymmetry in the emission, with the emission being elongated perpendicular to the outflow

axis. As in this extinction study, they perform fits to the off-outflow regions, and as a result increase the uncertainty in their fitted density index by 0.2 (included in the quoted uncertainty).

Taking account the uncertainties, the density power law indices derived from the millimeter and submillimeter emission agree both with each other and with the results from dust extinction analysis (Fit A, $p = 1.91 \pm 0.07$). However, the extinction method provides a direct measurement of the distribution that suffers none of the added uncertainties associated with the temperature profile in the core.

2.4 Summary

We present a near-infrared extinction study of the protostellar collapse candidate B335 using deep integrations from HST/NICMOS supplemented by data from the W.M. Keck Observatory. In summary:

1. We determine transformations between the NICMOS filters F160W and F222M and the standard H and K bands in the CIT photometric system for a range of (H − K) color from 0 to 3. At the accuracy of our data, the derived transformations do not have significant slopes or color terms.

2. The NICMOS mosaic image of the central 72″ region of B335 shows a dramatic fall off in the number of stars detected towards the protostar location, where the extinction increases due to the central concentration of dense core material. The NICMOS mosaic image contains a total of 119 stars detected in both filters, the innermost of

which is at a radius of $14''$. The photometry shows a steep gradient in the (H − K) colors toward the central protostar. In addition, there is a strong asymmetry in the colors superimposed on the overall gradient that coincides with the bipolar outflow.

3. We compare a series of models of dense core stucture to the extinction data, including the previously proposed models of inside-out collapse derived from molecular line observations. The *shape* of the E(H−K) radial profile is well matched by the inside-out collapse model, in particular the density fall-off as r^{-2} for the envelope and a flattening within the purported infall zone. An unstable Bonnor-Ebert sphere with dimensionless outer radius $\xi_{\rm max} = 12.5 \pm 2.6$ provides an equally good description of the density profile, and is indistinguishable from the collapse model over the range in radius where there are stars to fit. The inside-out collapse model is not unique. The power law index for the density distribution derived from extinction is consistent with recent determinations from dust emission measurements at millimeter and submillimeter wavelengths.

4. The bipolar outflow appears to be responsible for the dominant asymmetry in the extinction data. Stars whose line of sight fall within 45° of the outflow axis show lower extinction than those further away from the outflow. The effect of the outflow on the extinction data is reproduced very well by models that consider a hollowed out bipolar cone of constant opening angle. In the context of the inside-out collapse models, the observed asymmetry is too large to be explained by either rotation, or a weak magnetic field.

5. The entire extinction dataset can be well fitted by a model that includes infall, bipolar

outflow, and an additional $20\% \times \mathrm{E(H-K)}$ dispersion that mimics residual turbulent motions. The best fit outflow semi-opening angle is $\alpha = 41 \pm 2^{\circ}$ and the best fit infall radius is $R_{\rm inf} = 26 \pm 3''$. The fitted value of the infall radius is consistent with those derived from molecular line studies of B335, and supports the inside-out collapse interpretation of the density structure. The fitted opening angle for the bipolar outflow is somewhat larger than has been observed in high velocity CO emission, perhaps because the molecular line studies do not recover the full outflow width due to confusion with ambient emission at low velocities.

6. The normalization of the observed color excess is a factor of $\mathcal{F} \sim 5$ higher than the value predicted using the nominal 250 pc distance to B335, and the standard gas-to-dust ratio and near-infrared reddening law. The discepancy can conceivably be explained by a combination of a closer distance and a lower gas-to-dust ratio.

Acknowledgements

Partial support for this work was provided by NASA through grant number HST-GO-07843.01-A from the Space Telescope Science Institute, which is operated by AURA, Inc., under NASA contract NAS5-26555 We thank Bob Goodrich and Randy Campbell for invaluable assistance with the observations obtained at the W.M. Keck Observatory. DWAH thanks Brian McLeod for his help in running the NICREDUCE software, and Alex Wilson for his assistance with IDL graphics.

Appendix 2.A

SIMULATED EXTINCTION OBSERVATIONS

This appendix contains the tools and general recipe for constructing the simulated observations of B335 presented in Sections 2.3.7 & 2.3.8.

2.A.1 The Background Luminosity Function

We construct a composite luminosity function for the background population by combining the data from fields away from the extinction of the B335 dense core. In deriving the luminosity function, the photometry for each field was cut at a very high completeness level, where the number of stars per unit magnitude range peaks. (This is a very conservative estimate of limiting magnitude.) To avoid any issues concerning how the stars should be binned, the cutoff was determined by finding where the gradient of the cumulative luminosity function was steepest. For the dataset from the fifth NICMOS strip field, which includes 202 detected stars at H and 85 detected stars at K, the cut-off magnitudes are 20.7 at H, and 18.7 at K. For the combined dataset of the four Keck off-fields, which includes 242 detected stars at H and 246 detected stars at K, the cut-off magnitudes were 18.8 for both filters.

The empirical H-band luminosity function was calculated in three parts out to the NICMOS high completeness limit (H = 20.7). For the bright end (H < 12.85), only stars from the NICMOS fifth strip field are included, as stars brighter than this limit were satu-

rated in the Keck images. For the mid-range ($12.85 < \mathrm{H} < 18.8$), stars from both datasets contribute to the function. For the faint end ($18.8 < \mathrm{H} < 20.7$), above the Keck high completeness limit, only stars in the NICMOS fifth strip field were included. In each part, the number of stars was divided by the relevant observed area to build up the cumulative luminosity function. In the part where the NICMOS and Keck data overlap ($12.85 < \mathrm{H} < 18.8$), the two datasets show good agreement. The K band luminosity function was constructed following the same procedure, and it is effectively the same as for the H band, offset by the mean color of $\mathrm{H} - \mathrm{K} = 0.13$ magnitudes.

2.A.1.1 Luminosity Function Extrapolation

The central regions of B335 were observed to a deeper limiting magnitude than the strip or the $10'$ off fields, by about 4 magnitudes (H band) at the mosaic center, and about 3 magnitudes at the edge (see Figure 2.2). Although the stars in these central regions of B335 are highly extincted, the empirical background luminosity function must be extrapolated in order to simulate the deepest observations. Since the least extincted star in the NICMOS mosaic has $\mathrm{H} - \mathrm{K} = 0.47 \pm 0.08$, corresponding to an extinction of $A_{\mathrm{H}} = 1.3 \pm 0.2$, the luminosity function must be extrapolated by about 2 magnitudes at H in the simulations.

The form of the H cumulative luminosity function suggests that a broken power law provides a good description. The function was fitted by minimizing the χ^2 of the fit to the

bright-end of the luminosity function. The resulting function is given by:

$$N(m < H) = 5.4 \text{ stars arcmin}^{-2} \times \begin{cases} (\mathrm{H} \,/\, 14.17)^{2.95} & \text{for H} \leq 14.17 \\ (\mathrm{H} \,/\, 14.17)^{9.56} & \text{for H} > 14.17 \end{cases} \tag{2.13}$$

2.A.2 A Recipe for Constucting Simulations

Simulated observations of B335 were constructed by superimposing a model cloud on a field of background stars with the appropriate characteristics. The column density was calculated at the position of each background star and converted into two observable quantities: (1) an extinction at H band, and (2) a color excess E(H − K). These conversions are based on the gas-to-dust ratio, and reddening law. (A brief discussion on the uncertainties of these quantities is given in Section 2.2.1.)

To summarize, the recipe for constructing simulated observations has the following steps:

1. Generate a background star field by selecting randomly from the broken-power-law cumulative luminosity function in concert with the Gaussian color distribution of the background population. The broken-power-law luminosity function is extended to H = 25, just beyond the limiting magnitude at the center of the NICMOS mosaic (Note that model background stars intrinsically fainter than H = 23 are not recovered in the simulated observations of the fitted models from Table 2.1 — the function is extended to H = 25 simply to ensure completeness). Positions for each star are assigned randomly within a region $8' \times 2'$, to encompass the area of the NICMOS observations.

2. Select a model density distribution to describe B335.

3. Calculate the column density for each star in the region.

4. Convert the column density to an extinction at H band, $A_{\rm H}$, and a color excess E(H − K) using an assumed gas-to-dust ratio, R, and a reddening law, $A_{\rm H}/A_{\rm V}$. The "standard" prescription is (Bohlin et al. 1978, Rieke & Lebofsky 1985):

$$A_{\rm H} = 0.88 \left(\frac{N({\rm H}+{\rm H_2})}{1\times10^{22}\ {\rm cm}^{-2}}\right)\left(\frac{2\times10^{21}\ {\rm cm}^{-2}{\rm mag}_V^{-1}}{\rm R}\right)\left(\frac{A_{\rm H}/A_{\rm V}}{0.175}\right) \quad (2.14)$$

$$E({\rm H}-{\rm K}) = A_{\rm H}\ /\ 2.78\ . \quad (2.15)$$

(In the simulations, the reddening law was allowed to vary up to 15–25% steeper than the standard law in order to more exactly reproduce the observed starcounts. A fluctuation upward in the star counts at the one standard deviation level explains the inferred steeper reddening law.)

5. Modify the magnitudes and colors of each background star appropriately.

6. Simulate the NICMOS observations by applying the spatially dependent detection limits (Figure 2.2).

Chapter 3

Inner Structure of Protostellar Collapse Candidate B335 Derived from Millimeter-Wave Interferometry[1]

Daniel W.A. Harvey, David J. Wilner, Philip C. Myers, Mario Tafalla, & Diego Mardones

2003a, *The Astrophysical Journal*, **583**, 809

---

[1]Based on observations carried out with the IRAM Plateau de Bure Interferometer. IRAM is supported by INSU/CNRS (France), MPG (Germany) and IGN (Spain).

Abstract

We present a study of the density structure of the protostellar collapse candidate B335 using continuum observations from the IRAM Plateau de Bure Interferometer made at wavelengths of 1.2 mm and 3.0 mm. We analyze these data, which probe spatial scales from 5000 AU to 500 AU, directly in the visibility domain by comparison to synthetic observations constructed from models that assume different physical conditions. This approach allows for much more stringent constraints to be derived from the data than from analysis of images. A single radial power law in density provides a good description of the data, with best fit power law density index $p = 1.65 \pm 0.05$. Through simulations, we quantify the sensitivity of this result to various model uncertainties, including assumptions of temperature distribution, outer boundary, dust opacity spectral index, and an unresolved central component. The largest uncertainty comes from the unknown presence of a centralized point source. The maximal point source with 1.2 mm flux of $F = 12 \pm 7$ mJy reduces the power law density index to $p = 1.47 \pm 0.07$. The remaining sources of systematic uncertainty, of which the most important is the radial dependence of the temperature distribution, likely contribute a total uncertainty at the level of $\delta p \lesssim 0.2$. Taking account the uncertainties, we find strong evidence that the power law index of the density distribution within 5000 AU is significantly less than the value at larger radii, close to 2.0 from previous studies of dust emission and extinction. Images made from the data show clear departures from spherical symmetry, with the globule being slightly extended perpendicular to the outflow axis. The inclusion of a crude model of the outflow as a hollowed bipolar cone of constant opening angle improves the fit and leaves the resulting density power law index unchanged. These results conform

well to the generic paradigm of isolated, low-mass star formation which predicts a power law density index close to $p = 1.5$ for an inner region of gravitational free fall onto the protostar. However, the standard inside-out collapse model does not fit the data as successfully as a simple $p = 1.5$ power law because of the relative shallowness of the predicted density profile just within the infall radius.

3.1 Introduction

The dense core in the B335 dark globule is generally recognized as the best protostellar collapse candidate. This dense core is nearby (250 pc, Tomita, Saito & Ohtani 1979), isolated, and nearly spherical. It contains a deeply embedded low luminosity young stellar object (3 $L_\odot$) discovered at far-infrared wavelengths by Keene et al. (1983) and detected by IRAS only at $\lambda \geq 60$ μm. Detailed radiative transfer models based on the theory of inside-out collapse (Shu 1977) provide very good fits to spectral line profiles of the dense gas tracers CS and H_2CO observed at $10''$–$30''$ resolution (Zhou et al. 1993; Choi et al. 1995).

Recent studies have raised serious doubts about the inside-out collapse interpretation of the molecular line profiles. Observations of the CS(5-4) line at higher angular resolution, about 500 AU, show that the high velocity emission arises from the inner part of a bipolar outflow, not from the gravitational acceleration of dense gas close to the protostar (Wilner et al. 2000). In addition, studies of starless cores show that some molecular species, in particular CS, are frozen out onto grains at densities characteristic of the inner regions of B335 (Caselli et al. 2002, Tafalla et al. 2002). If protostellar heating does not promptly

desorb CS molecules from icy grain mantles, then this species likely makes a poor probe of the gas kinematics in the presumed infall zone.

Since the density field is strongly coupled to the velocity field, observations of dust emission and absorption provide an alternative means to infer the dynamical state of the dense core. Harvey et al. (2001) describe deep near-infrared extinction measurements toward B335 that show a density profile consistent with the inside-out collapse theory, in particular an r^{-2} density profile for the outer envelope and an inner turnover towards free-fall. The best fit model has an infall radius of 6500 AU ($26''$), similar to that derived from molecular line studies (Zhou et al. 1993; Choi et al. 1995). The extinction data also show the dramatic effect of the bipolar outflow driven by the protostar. However, extinction measurements could not be made interior to 3500 AU ($14''$), where no background stars are visible, even with NICMOS on HST. As a result, the extinction data could not distinguish the inside-out collapse model from, e.g. a highly unstable Bonnor-Ebert sphere, whose density profiles depart significantly from each other only at radii $\lesssim$ 2500 AU.

Observations of long wavelength dust emission provide another method for probing density structure. This technique is nearly as direct as observations of dust extinction. The intensity of the emission provides an integral along the line-of-sight of the product of the density, temperature, and opacity of the dust. By modeling the dust temperature and specific mass opacity, the observed intensities may be used to constrain the density distribution. The analysis of dust emission complements extinction work because the dust emission method becomes most effective in the high column density inner regions of dense cores where dust extinction becomes large and difficult to penetrate.

Dust emission has been used very successfully to measure density structure of dense cores using bolometer cameras at millimeter and submillimeter wavelengths on large single dish telescopes, including the IRAM 30 meter (Ward-Thompson, Motte & Andre 1999, Motte & Andre 2001) and the JCMT (Ward-Thompson et al. 1994; Visser, Richer & Chandler 2001, Shirley et al. 2000). Unfortunately, the central regions of the nearest protostellar cores are generally comparable in size to the beamwidths of these telescopes and are poorly resolved. The density structure at smaller scales can only be probed with interferometers. With interferometer observations, the density structure may be strongly constrained through analysis of dust emission directly in the visibility domain. So far, detailed modeling of millimeter continuum visibility data in this context has been rarely applied (Keene & Masson 1990, Hogerheijde et al. 1999, Mundy, Looney & Welch 2000)

B335 has been imaged with millimeter interferometers in several previous studies (Chandler & Sargent 1993, Hirano et al. 1992, Saito et al. 1999). In this paper, we present observations of dust continuum emission from B335 at both 3 mm and 1.2 mm obtained with the IRAM Plateau de Bure Interferometer (PdBI) that obtain considerably better sensitivity. These observations sample well the density profile of B335 from size scales of ~ 5000 AU to ~ 500 AU, affording an order of magnitude better resolution than has been possible with single dish telescopes. The visibilities can discriminate the behaviour of the various physical models that all match the near infrared extinction in the outer regions of B335.

3.2 Observations

Continuum emission from B335 was observed with the IRAM PdBI simultaneously with the CS(5-4) line emission reported by Wilner et al. (2000). In brief, a single pointing was observed using 5 antennas in the D configuration giving baseline lengths from the shadowing limit of 15 meters to nearly 80 meters. The tuning was single (lower) sideband at 100 GHz (3.0 mm) and double sideband at 245 GHz (1.2 mm). The half power field of view is $50''$ at 3.0 mm and $20''$ at 1.2 mm. The absolute flux scale was determined through observations of the standard source MWC349, assumed to be 1.09 Jy at 3.0 mm at 1.82 Jy at 1.2 mm, with estimated uncertainties of 20% and 10%, respectively. Continuum visibility records at the two wavelengths were formed for each 60 second integration of the digital correlator (3×160 MHz at 1.2 mm, 1×160 MHz at 3.0 mm), excluding a few channels contaminated by molecular line emission, which resulted in 2372 records at 3.0 mm and 4824 records at 1.2 mm (after flagging occasional bad records). In addition to amplitude and phase, each record also contains a variance measure, determined from the system temperatures and antenna gains.

3.3 Constructing Model Visibilities

We analyze the dense core structure using the interferometer measurements directly, in the visibility domain, without producing images. While this approach is computationally intensive, it recognizes the limitations of standard Fourier inversion and deconvolution techniques, and allows a much more direct comparison with models than analyzing images,

avoiding the problems caused by synthesized beam characteristics.

The B335 visibilities are compared to theoretical models of protostellar envelope structure by constructing synthetic visibilities, taking account of (1) the dust continuum radiative transfer, and (2) the specifics of the observations, including the exact (u, v) sampling and primary beam attenuation. The analysis of dust emission requires more complexity than dust extinction, because the models must include assumptions about the temperature distribution and specific mass opacity in addition to the model density field. Since we cannot consider an exhaustive list of protostellar envelope models, we instead fix attention on a few widely promoted density fields, including simple power law descriptions, inside-out collapse, and the Bonnor-Ebert sphere. These models all successfully match the near-infrared extinction data in the outer regions of B335, beyond ~ 5000 AU, but they predict substantial differences in the inner regions that are sampled by the interferometer.

3.3.1 Analytic Description for Power Law Distributions

The measured visibilities are given by the Fourier transform of the antenna weighted intensity distribution emergent from the globule. In our analysis, we must numerically model visibilities for comparison with the data. However, several simplifying assumptions exist that provide an analytic solution that affords some intuitive understanding of how the various physical quantities affect the visibilities.

For optically thin dust emission, the observed intensity at impact parameter b from a

spherically symmetric globule is given by

$$I_\nu(b) = 2\int_b^{R_{\rm out}} B_\nu(T_d(r))\,\kappa_\nu(r)\,\rho(r)\,\frac{r}{\sqrt{r^2-b^2}}\,dr \tag{3.1}$$

where $R_{\rm out}$ is the outer radius of the globule, $T_d(r)$ the dust temperature, $\rho(r)$ the density, κ_ν the specific dust opacity, and $B_\nu(T)$ is the Planck function. If the density, and temperature follow simple radial power laws, $\rho \propto r^{-p}$, $T \propto r^{-q}$, and the opacity is a power law in frequency that does not vary along the line-of-sight, $\kappa_\nu \propto \nu^\beta$, then if the emission is assumed to be in the Rayleigh-Jeans (R-J) regime ($h\nu/kT << 1$) from a globule with infinite outer boundary, the emergent intensity also has a simple power law form, i.e. $I(\nu,b) \propto \nu^{2+\beta} b^{-(p+q-1)}$ (Adams 1991). If we neglect the attenuation resulting from the antenna pattern of the interferometer, then the visibility distribution is also a power law, i.e. $V(\nu,u) \propto \nu^{2+\beta} u^{(p+q-3)}$, where u is the baseline length. With these approximations, the slope of the visibility profile — like the intensity profile — is determined solely by the sum of the power law indices assumed for the temperature and density. Note that a more steep density falloff with radius results in a less steep decrease in visibility with increasing baseline length. The relative brightness of the emission at different frequencies is determined by β, the dust opacity index.

3.3.2 Numerical Calculation of Model Visibilities

The synthetic visibility datasets used to compare with the observations are produced by a series of programs written in the Interactive Data Language (IDL) developed by Research Systems Inc.

The first step consists of simulating the emergent intensity distribution. Given inputs of model density and temperature distributions, and an adopted specific mass opacity, the program calculates the intensity image consisting of a 512×512 pixel array at resolution $0\farcs5$ per pixel, using the full Planck function for the emissivity, and integrates the radiative transfer equation through the model globule. These parameters determine the shape of the emergent intensity, and also the relative brightness at 1.2 mm and 3.0 mm (from the frequency dependence of the opacity). In general, each model is normalized by matching to the 1.3 mm flux measurement of Shirley et al. (2000), $F = 0.57 \pm 0.09$ Jy within a circular aperture (top-hat) of $40''$ diameter. The matching is achieved by iteratively scaling the product $\kappa_\nu \rho$ (κ_ν is the opacity, ρ the density). We adopt an outer boundary of $R_{\rm out} = 0.15$ pc in the models; this is well constrained both by the extinction measurements (Harvey et al. 2001) and by molecular line observations (e.g. Zhou et al. 1990). Modifying the outer boundary assumption by as much as 50% was also found to have almost no discernable effect on our results.

The next step is to simulate observations of the model intensity images. The program approximates the antenna pattern of the IRAM dishes as a Gaussian of FWHM $50''$ (100 GHz/ν). Varying illumination, focus and pointing during the observations will cause the actual antenna pattern of the IRAM dishes to depart slightly from a pure Gaussian, but we expect this deviation to be small enough to have little impact on our analysis. We must account for the fact that the position of the peak millimeter emission is not exactly at the field center. To reduce the number of parameters to be fit, we fix the offset from the center as determined from a simple Gaussian fit to the 1.2 mm data: ΔR.A.,

ΔDec. $= (2\farcs23 \pm 0\farcs08, -0\farcs79 \pm 0\farcs12)$, giving coordinates for the peak of α = 19:37:00.89, δ = 7:34:10.0. Experimenting with offsets $\sim 0.1''$ different from these values showed no discernable change in the fitting results. The program performs an inverse FFT (to choose the positive sign in the exponential), and adjusts phase to take account of the offset position. This procedure results in an array of the visibility function sampled on a regular grid of u and v. The program then interpolates both the real and imaginary parts of the visibility to the exact (u, v) points sampled by the IRAM PdBI observations for comparison with the data.

3.3.3 Model Selections

As detailed above, the model visibilities are derived from the assumed (1) mass density distribution $\rho(r)$, (2) dust temperature distribution $T_d(r)$, and (3) specific mass opacity of the dust κ_ν. We consider the expected form of these quantities, and their uncertainties.

Density

The ultimate goal is to constrain the density distribution of B335, given realistic choices for the temperature and opacity. The most basic models are simple power laws with radius, with the aim to constrain the power law index p in the inner region. As an extension we also consider the physical models that arose in the Harvey et al. extinction study: (1) a Bonnor-Ebert sphere with $\xi_{max} = 12.5$, and (2) an inside-out collapse model with $R_{\rm inf} = 0.03$ pc ($25''$ at 250 pc). We also consider the effect of the bipolar outflow on the millimeter data, adopting the crude hollow cone description that successfully matched the near-infrared

extinction data.

Temperature

For a optically thin dust envelope heated by a central source, the dust temperature distribution is expected to follow a power law with index determined by the frequency dependence of the opacity, i.e. $T_d(r) \propto L^{q/2} r^{-q}$, where $q = 2/(4+\beta)$ (Doty & Leung 1994). Breakdowns in this approximation will occur at small radii where the envelope becomes optically thick to the bulk of the short wavelength emission (or there is a circumstellar disk), and at large radii where heating from the Interstellar Radiation Field (ISRF) becomes important.

For B335, the inner breakdown of the power law approximation is expected at radii $\lesssim$ 100 AU, and would manifest as a steeply increasing temperature gradient. For the IRAM PdBI observations, the longest baseline of $\sim$ 60 kλ corresponds to a linear resolution of $\sim$ 900 AU. Hence, any optically thick region at small radii, or the presence of a disk, would appear as an unresolved component in these data. The nature and extent of the breakdown at large radii depends on the local strength of the ISRF. The modelling of Shirley et al. (2002) suggests that for typical envelope density distributions $\rho \propto r^{-p}$, with $p \sim$ 1–2, the temperature follows very closely a power law description until falling to just under 10 K, where it flattens until at large radii external heating induces a rise to $\sim$ 12–15 K. The detailed models of Shirley et al. (2002) for B335, using $p = 1.8$ and an opacity index $\beta = 1.8$, indicate that the temperature falls to about 10 K at a radius of $\sim$ 5000 AU. For the model PdBI visibilities, any (small) variations in temperature beyond this radius have little effect because the mass density has already decreased to $\sim 8 \times 10^4$ cm^{-3} (only 6%

of its value at 1000 AU), and the interferometer begins to filter emission on angular scales much larger than the FWHM at 1.2 mm, $\sim 20''$ (~ 5000 AU). For our standard model, we adopt the simple power law, with a minimum temperature of 10 K, i.e.

$$T_d(r) = \begin{cases} 10\ (5000\ \mathrm{AU}/r)^{0.4}\ \mathrm{K} & \text{for r} \leq 5000\ \mathrm{AU} \\ 10\ \mathrm{K} & \text{for r} > 5000\ \mathrm{AU} \end{cases} \tag{3.2}$$

In Section 3.5.1 we investigate the uncertainties in the density profile that result from the temperature distribution in the model fitting process.

Mass Opacity

The mass opacity of dust grains in the millimeter region of the spectrum in protostellar envelopes is uncertain, but generally assumed to follow a power law with frequency, $\kappa_\nu \propto \nu^\beta$. The power law index varies depending on the dust properties, but tends to be bounded by a small range, roughly 1–2 (Ossenkopf & Henning 1994). For our standard model, we follow Looney, Mundy & Welch (2000) and adopt $\kappa_\nu = 0.1(\nu/1200\ \mathrm{GHz})\ \mathrm{cm}^2\ \mathrm{g}^{-1}$, a power law with dust emissivity index β equal to unity. Since the globule is optically thin at the wavelengths of the PdBI observations, especially at 3.0 mm, the power law index in the models can be adjusted to produce the best simultaneous match at the two observed wavelengths.

3.4 Fitting Model Parameters and Evaluating Fit Quality

The basic procedure is to maximize the probability distribution:

$$P(\text{Model} \mid \text{data}) = \prod_i e^{-(Z_i - f(x_i;p,m))^2/2\sigma_i^2} \times e^{-(m-m_0)^2/2\sigma_m^2} \tag{3.3}$$

where the Z_i are the visibility data points with uncertainty σ_i, $f(x_i;p,m)$ are the model data points, p a free parameter in the models, and m a model parameter about which we have a constraint (namely that it is a Gaussian random variable with mean m_0 and standard deviation σ_m). Maximizing the probability distribution is equivalent to minimizing the logarithm of its inverse. Taking account the fact that the Z_i are by nature complex visibilities, we want to minimize a modified χ^2:

$$\tilde{\chi}^2 = \sum_i \frac{|Z_i - f(u,v;p,m)|^2}{\sigma_i^2} + \frac{(m-m_0)^2}{\sigma_m^2} \tag{3.4}$$

It is useful to be more explicit about the parameters p & m. The free parameter p is used to describe the shape of the model, e.g. the index of the power-law density distribution. The parameter m allows us to include observational uncertainties, e.g. the 20% uncertainty in the normalization of the model derived by matching the 1.3 mm flux measured by Shirley et al. (2000). This is achieved by allowing the 1.2 mm model visibilties to be scaled by a constrained parameter m, a Gaussian random variable with mean 1.0 and standard deviation 20%. For the 3.0 mm model visibilities, we use two different approaches: (1) scale the 3.0 mm data by the same factor m as the 1.2 mm data to force a dust opacity index of unity; (2) allow the 3.0 mm data to be freely scaled, to measure the dust opacity index and as a general check for consistency (by interpreting the derived value β in the context of the realistic range described above).

We select a model description and perform a fit for the model parameters by minimizing the modified χ^2 distribution that includes data at both wavelengths. Since the models are non-linear in the fitting parameters, we analyze the uncertainty in the best-fit model parameters using a Monte Carlo technique known as the *bootstrap* method (Press et al. 1992, p. 691). To describe this method, consider the dataset S used in the fitting. The first step is to construct a new dataset of equal size S', by randomly selecting N times from the original dataset. This new sample is then analyzed in the same way as the original dataset, and the fitted model parameters recorded. This process is then repeated n times, where n is sufficiently large that the resulting distribution of best-fit model parameters is insensitive to its exact value (for our models, typically $n = 200$). If the fitting parameters may be successfully constrained by the data, then the distribution of best-fit parameters is very close to Gaussian, and the standard deviation of the distribution provides an estimate for the uncertainty of the parameters that best fit the original dataset.

The bootstrap method proves especially powerful for this analysis because small variations in the value of the modified χ^2 as defined above do not necessarily represent small variations in fit quality. The visibility dataset comprises a very large number of very low signal-to-noise measurements, which has the effect that the χ^2 wells are extremely shallow, and two models may seem almost equally good, despite the fact that there is ample signal to distinguish them. This occurs because the individual visibilities do not distinguish between the two models (represented by the χ^2 well being shallow) but the combination of all the individual visibilities does (represented by a lower χ^2 corresponding to a better fit). This issue could be circumvented by binning the visibilities e.g. radially, to increase the

signal-to-noise, and then performing a χ^2 fit to the binned values. We avoid this solution because the binning loses information on the asymmetry of the globule that is hidden in the dataset by the vectorial nature of visibility data. For the spherically symmetric models, we bin the data for graphical comparison with the models.

The shallowness of the χ^2 wells results in the minimum values of the reduced χ^2 for various models all having similar absolute values, in the range $\chi^2_\nu = 1.4$–1.5. While a lower value of χ^2_ν may be interpreted as providing a better fit, the small range of variation confuses the differences in the fit quality. Therefore, we adopt graphical techniques to express the superiority of one model fit over another.

3.5 Results and Analysis

Table 1 summarizes the results from the χ^2 fits to several spherically symmetric models, as well as axisymmetric models. For fits marked '#a', the normalization of the 3.0 mm visibilities is constrained by fixing the dust opacity index β to unity. For fits marked '#b', the dust opacity index is included as an additional fitting parameter.

3.5.1 Spherically Symmetric Models (Fits I–IV)

Although the B335 dense core shows clear departures from spherical symmetry when viewed both in dust extinction and molecular emission, for simplicity and insight we start by investigating spherically symmetric density models. In Fits Ia & Ib, we use a power law model for the density distribution. In Fit IIa, we use a power law density model but

Table 3.1. Summary of the Density Model Fits

Fit	Density Model	Dust Index	Fitted Model Parameter(s)	χ^2_ν
Ia	Power law: $\rho \propto r^{-p}$	$\beta = 1$	$p = 1.61 \pm 0.06$; $M = 1.10 \pm 0.13$	1.4647
Ib	As Fit Ia	β =Free	$p = 1.65 \pm 0.05$; $\beta = 0.81 \pm 0.12$	1.4646
IIa	Power law + point flux F	$\beta = 1$	$p = 1.47 \pm 0.07$; $F = 12 \pm 7$ mJy; $M = 1.24 \pm 0.15$	1.4645
IIIa	Bonner-Ebert, $\xi_{\rm max} = 12.5$	$\beta = 1$	...	1.5025
IVa	Inside-out, $R_{\rm inf} = 0.03$ pc	$\beta = 1$	...	1.4674
Va	Power law + outflow	$\beta = 1$	$p = 1.60 \pm 0.06$; $\alpha = 38° \pm 5°$; $M = 1.10 \pm 0.13$	1.4625
Vb	As Fit Va	β =Free	$p = 1.65 \pm 0.05$; $\alpha = 40° \pm 5°$; $\beta = 0.74 \pm 0.10$	1.4622

include an additional point source component to the intensity distribution. We also consider Bonnor-Ebert spheres (Fit IIIa; Bonnor 1956, Ebert 1955), and the Shu (1977) inside-out collapse model (Fit IVa).

Single Power Laws

In the simplest model, the density distribution is described by a single power law. The best-fitting model has a power law index of $p = 1.65 \pm 0.05$ (Fit Ib) with a dust opacity index $\beta = 0.81 \pm 0.12$ that is consistent with unity. Fit Ia, which assumes $\beta = 1$, gives a density power law index that agrees within uncertainties with that for Fit Ib. Figure 3.1 shows a plot of binned visibility amplitude vs. (u, v) distance for both wavelengths. The binning is logarithmic and oversamples the data by a factor of 2; filled symbols and non-filled symbols are not completely independent. The amplitudes are the vectorial mean of the complex visibilities in each bin (corrected for the offset phase center), the error bars represent one

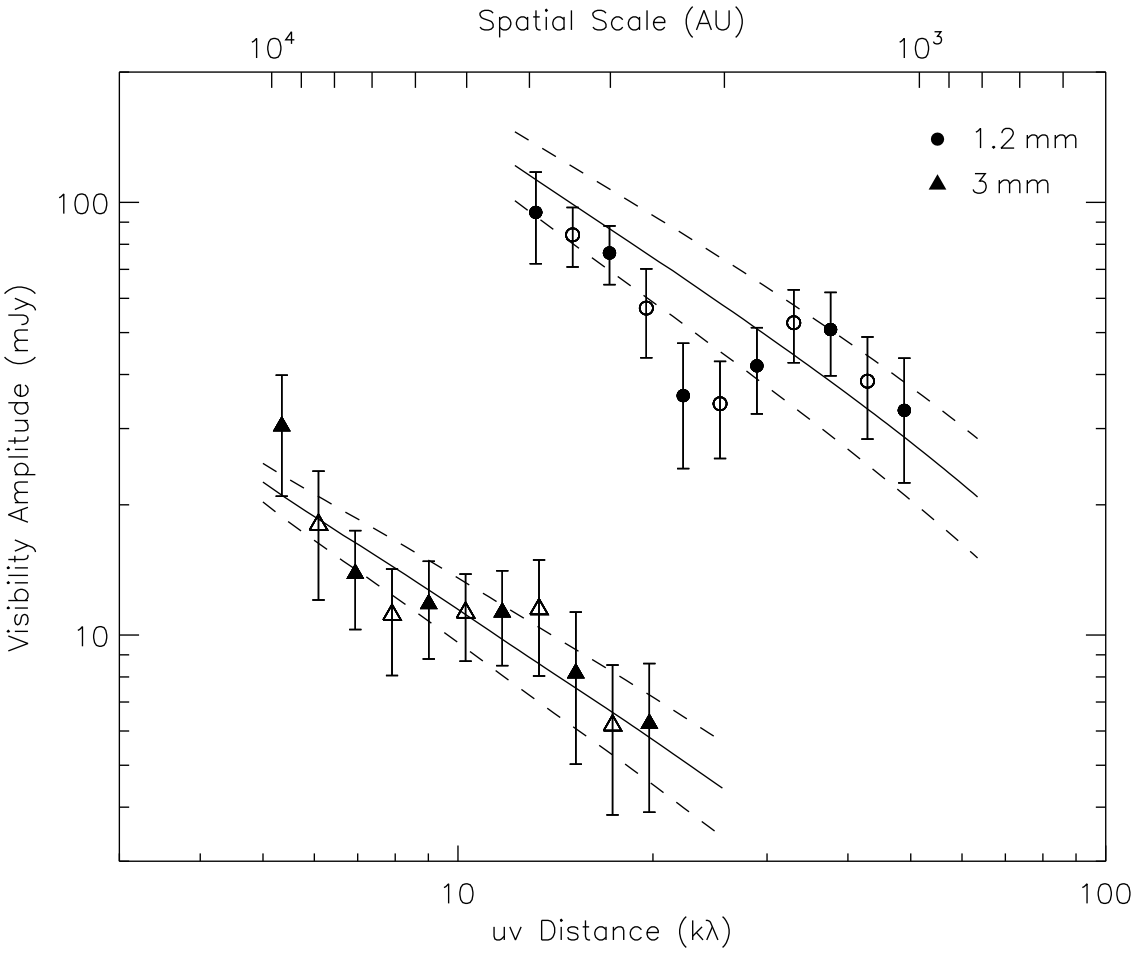

Fig. 3.1.— Binned visibility amplitudes against (u, v) distance at 3.0 mm (triangles) and 1.2 mm (circles) for the PdBI observations of B335 together with the unscaled curves for the best fitting single power law model $p = 1.65$ (solid line), and power law models that deviate by 2 σ, $p = 1.55$ (lower dashed line) and $p = 1.75$ (upper dashed line). Note that the bins oversample the data and the filled symbols are not completely independent from non-filled symbols. The spatial scale on the top is defined as 250 pc $\times \lambda/D$, where D is the baseline length.

standard deviation in the mean. For the dust emission at both wavelengths, the decrease in visibility amplitude with baseline length may be well described by a power law. The plots also show the visibility curves for the best fit model ($p = 1.65$) and models that deviate by $\pm 2\sigma$ ($p = 1.55$ and $p = 1.75$). These models have not been scaled by the fitting parameters since this term contributes to the χ^2 and its exclusion allows the differing quality of each fit to be better seen (note that the $\pm 2\sigma$ models require a scaling at 1.2 mm of 1.19 and 0.75 for $p = 1.55$ and $p = 1.75$, respectively).

Sensitivity to Temperature Assumptions

These results use the temperature distribution described in Section 3.3.3, which is based on a physical argument. To understand the sensitivity of the density power law results to the temperature, we investigate how subtle quantitative changes affect the results by repeating the fitting procedure with temperature distributions that (1) have different (constant) temperature in the outer envelope, and (2) have different power law indices.

We find that the fitted density power law index is insensitive to (small) changes in the envelope temperature: variations of ± 2 K lead to variations in the inferred density slope of much less than the quoted uncertainty. The main reason is that the antenna FWHM is only $20''$ at 1.2 mm (which has the higher signal-to-noise ratio of the two wavelengths), and the data are not very sensitive to the temperature structure at larger radii. Therefore, uncertainties in the strength of the ISRF are relatively unimportant in this study.

Changes in the power law index of the inner temperature distribution produce more significant changes in the fitting results. The globule envelope is optically thin at both

wavelengths; if the R-J approximation were also to hold, then the inferred density power law index p would be related to the temperature power law index q by the relation $p + q$ = constant. However, the R-J approximation breaks down, especially at 1.2 mm, with the consequence that p is more sensitive to changes in q. We find that varying q by ± 0.1 leads to variations in p at the level of $\simeq \mp 0.15$.

Sensitivity to an Unresolved Central Component

As already noted, there may exist a central region of B335 for which the envelope will be optically thick at infrared wavelengths, causing the temperature profile to depart from a simple power law. In this region, the temperature is expected to climb very sharply with radius, resulting in increased emission at long baselines beyond the extrapolation of a simple power law. The presence of an unresolved disk, effectively a warm central point source, would have a similar effect. While the PdBI data samples insufficient baseline lengths to directly measure the flux of any such compact component, it will, if present, flatten the visibility profiles of the various models and therefore affect the fitted density power law index. Fit IIa quantifies the effect using the combination of the simple power law for density, temperature and mass opacity from Fit Ia, but including an additional point source component with $F \propto \nu^3$ (i.e. the spectrum of a source where the majority of the emission is optically thin at 1.2 mm, with a dust opacity index of unity). For a point source flux $F = 12 \pm 7$ mJy at 1.2 mm, the most allowed by the measurements at long baselines, the fitted density index is reduced to $p = 1.47 \pm 0.07$. This point source flux corresponds to an implied disk mass of $M \simeq 2 \times 10^{-3}\,\mathrm{M}_\odot\,(60\ \mathrm{K}/T_{\mathrm{disk}})$ for our adopted opacity law. This is

at the lower end of the 0.002–0.3 $M_\odot$ range of disk masses that have been observed around T Tauri stars by Beckwith et al. 1990. Since accretion disks result from conservation of angular momentum during the collapse process, the small inferred mass of the disk may be related to the fact that B335 has a relatively low rotation rate (Frerking, Langer & Wilson 1987). However, accretion disks may also be connected with the driving source of bipolar outflows, and the B335 outflow is not unusual, with size, momentum and energy typical for a low mass protostar (Goldsmith et al. 1984).

When a compact source of emission is included in the analysis, the fitted density power law index is reduced by roughly -0.2. Thus, possible point source "contamination" is the dominant source of systematic uncertainty in the fitted density structure. This is also the case in single dish measurements, where a point source can add a systematic uncertainty of up to about -0.5 to the inferred density index (e.g. Shirley et al. 2002).

Table 3.2 summarizes various sources of systematic error and the level of uncertainty that the variations contribute to the fitted density power law index in the spherically symmetric models.

Comparison With Previous Studies

The best fit density power law index of $p = 1.65$ is slightly less steep than the value of $p = 1.8$ found by Shirley et al. (2002) from SCUBA data. It is perhaps significant that the results from the two instruments are consistent to within the uncertainties considering the resolution of the JCMT at 850 μm is $15''$, roughly encompassing the entire range of radii probed by the the IRAM PdBI. However, even taking account all sources of uncertainty, the

Table 3.2. Summary of systematic uncertainties in the fitted density power-law index p

Model Parameter	Variation	Resulting δp Systematic Error
Temperature power-law index, q	$\delta q \lesssim \pm 0.1$	$\lesssim \mp 0.15$
Outer envelope temperature (ISRF)	$\delta T \lesssim \pm 2$ K	$\lesssim \pm 0.05$
Central point source, flux F	$F = 12 \pm 7$ mJy	-0.18 ∓ 0.1
Dust opacity spectral index β	$\beta = 1 \rightarrow \beta =$ free	$\simeq 0.05$
Outer boundary of B335, $R_{\rm out}$	$\delta R_{\rm out}/R_{\rm out} \lesssim 50\%$	$\lesssim 0.01$
Outflow cone geometry, $\alpha = \alpha(r)$	$\delta\alpha(r) \lesssim \pm 20°$ [1]	$\lesssim \mp 0.08$

[1] Refers to an outflow geometry where the opening angle changes monotonically by 20° over the 500–5000 AU range in radius to which the data is sensitive.

best-fit power law index of $p = 1.65$ is significantly less steep than the $p = 2.0$ power law index of the hydrostatic isothermal sphere that so successfully matches the outer envelope of B335 in near-infrared extinction (Harvey et al. 2001) and dust emission shape (Shirley et al. 2002) This result suggests that the density profile becomes less steep in the inner regions ($r \lesssim 25''$), a conclusion also suggested by the extinction data, where two models with this character (inside-out collapse and the Bonnor-Ebert sphere) provided better fits than a single power law.

Broken Power Laws, Inside-Out Collapse, Bonner-Ebert Sphere

We have also investigated models with density distributions that flatten in the inner region: (1) a broken power law, with fixed index of $p = 2$ in the envelope, with model parameters

the break radius and inner power law index; (2) an inside-out collapse model with model parameter the infall radius (this is approximately a special case of the broken power law); and (3) a Bonnor-Ebert sphere, where the model parameter is the dimensionless outer radius of the sphere $\xi_{\rm max}$. None of these models fit the data nearly as well as a single power law.

For the broken power law model, it proved impossible to obtain robust results for the two fitted parameters, which are coupled and have comparable effects in the simulated datasets. Decreasing the break radius, or increasing the power law index in the inner region; each steepens the apparent density profile, and it is not possible to distinguish between the two effects.

The inside-out collapse model and the Bonnor-Ebert sphere that matched the extinction data both provide poor fits to the visibility data that sample the envelope closer to the protostar. Figure 3.2 shows a comparison between the binned visibility amplitude vs. (u, v) distance and the curves produced from these models: the inside-out collapse model with $R_{\rm inf} = 0.03$ pc, and the Bonnor-Ebert sphere with $\xi_{\rm max} = 12.5$. There are large discrepancies between these models and the data. Because these models so poorly describe the data, the χ^2 statistic provides a poor discriminant of model parameters. At the χ^2 distribution minimum, the bootstrap calculation bounces between the end points of the grid at each iteration, no matter how wide a range of model parameters are considered. Essentially, the data prefer a model with a single power law index $p \simeq 1.65$, and neither the inside-out collapse model nor the Bonner-Ebert sphere model can produce an equivalent slope over a sufficiently large enough range in spatial scales.

The inclusion of a point source component does not rectify the problems in fitting

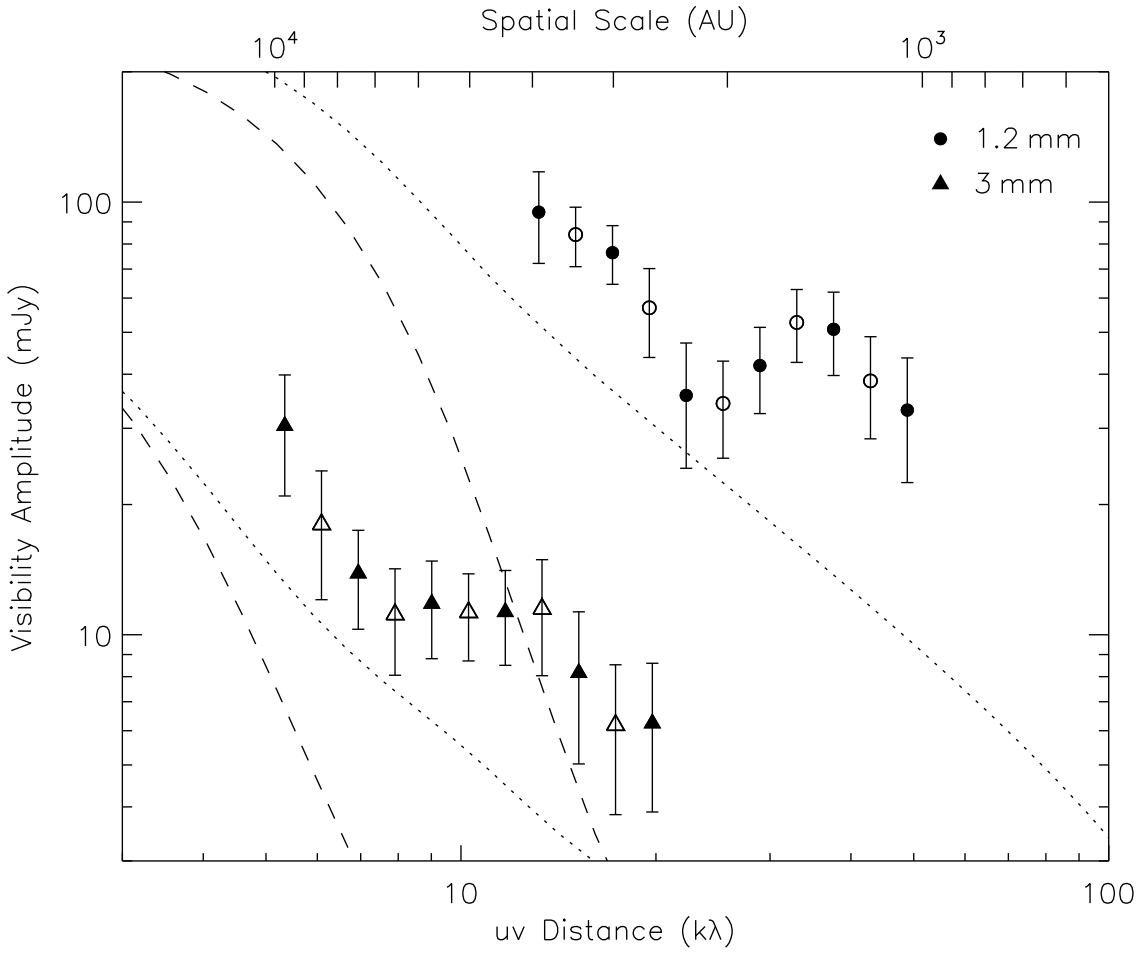

Fig. 3.2.— Same as Figure 3.1, but with theoretical curves for the Bonnor-Ebert sphere with $\xi_{\rm max} = 12.5$ (dashed line) and the inside-out collapse model with $R_{\rm inf} = 0.03$ pc (dotted line). Neither of these models can successfully match the data.

with these two physical models, despite effectively reducing the slope of the fitted density distribution. The Bonner-Ebert sphere has a relatively flat density distribution at small radii, and therefore the visibilities drop sharply at long baselines. Adding a point source to the Bonnor-Ebert sphere model adds intensity at long baselines but still cannot produce a good fit over the large range in spatial scale sampled by the data. For the inside-out collapse model, the fit fails to constrain the infall radius because this parameter does not affect the slope of the density distribution in the region where the data provide constraints (e.g. $R_{\rm inf} \gtrsim 0.024$ pc $= 20''$ at 250 pc).

A combination of the inside-out collapse model with a point source also produces a poorer fit to the data than does a simple power law with a point source. The χ^2 of this model is equivalent to power laws that are nearly 3σ away from the best fit (i.e. the fit quality is equivalent to the power law models with $p = 1.30$ or $p = 1.65$, when the best fit is for $p = 1.47 \pm 0.07$). This seems a surprising result, since the standard impression of the inside-out collapse model is that it behaves like a power law with index very close to 1.5 in the infalling region. But, while this is asymptotically true at very small radii, the local power law index of the inside-out collapse solution in fact decreases as one moves outwards in the infalling region, attaining a minimal value close to unity just within the infall radius. This means that for the same total flux within a $40''$ diameter, the inside-out model has greater intensity at larger radii than does a simple $p = 1.5$ power law. The effect is that while the slopes of the two visibility profiles are similar in the spatial range where the PdBI data are sensitive, the primary beam attenuation (FWHM $\simeq 20''$ at 1.2 mm) causes the inside-out model visibilities to be 25% fainter than the single power law model.

The required increase in the scaling parameter, m, to best match the data is significant and contributes to the increased value of χ^2, resulting in a worse fit for the inside-out collapse model. Essentially, the inside-out collapse model cannot simultaneously match the Shirley et al. (2000) flux measurement and the normalization of our observed visibility profile.

3.5.2 Axisymmetric Models (Fit V)

In Figure 3.3, the leftmost panels show images of B335 made from the 1.2 mm (top) and 3 mm (bottom) visibilities. These images show that the B335 dense core is not spherically symmetric at this size scale, but rather is more like an oblate spheroid, flattened along the axis of the bipolar outflow (nearly East-West on the sky). In Figure 3.3, the second column of panels shows images of the best fit spherically symmetric models, made by processing the synthetic visibilities in the same way as the data. The aspect ratio of the emission is clearly different between the models and the data. The asymmetry may be caused by the action of the outflow, or it may reflect a flattening in the intial configuration of the core.

For the dust extinction data at scales $\gtrsim 3500$ AU, the asymmetry was well reproduced by a model that assumed that the outflow had hollowed out a bipolar cone, with best fit constant semi-opening angle $\alpha = 41° \pm 4°$. To extend the analysis of the visibility data, we have added the same simple representation of the bipolar outflow to the power law density distribution models to determine if this model can also successfully explain the asymmetry in the observed dust emission. In these models, we assume no unresolved point source of significant flux, having already quantified the effect of this additional component in Section 3.5.1. We also assume that the temperature remains a simple radial power law.

This is an extreme simplification as the emptied outflow cavities provide a less obscured view to the hotter inner region, and as a result the temperature of dust near to the boundary of the outflow cavity will likely have been underestimated.

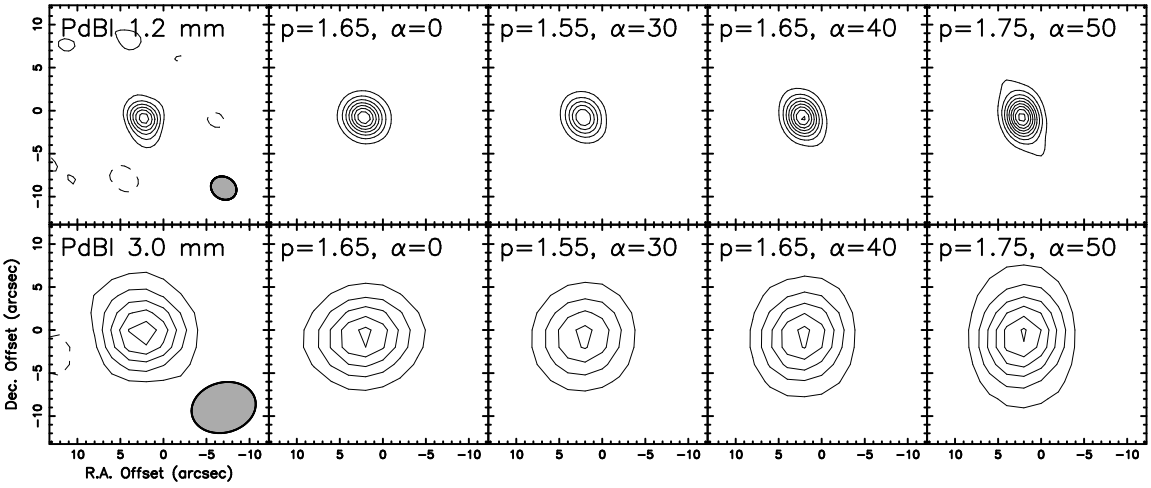

Fig. 3.3.— Images of B335 at 1.2 mm (top) and at 3.0 mm (bottom). The leftmost column shows images made from the PdBI data; other columns show images made from synthetic datasets produced from the various protostellar envelope models, including the best fit spherically symmetric power law model, $p = 1.65$, and the best-fit asymmetric model, $p = 1.65$, $\alpha = 40°$, bracketed by asymmetric models with parameter values that differ by 2σ, i.e. $p = 1.55$ and $\alpha = 30°$, $p = 1.75$ and $\alpha = 50°$. The contour levels are $(2, 4, 6, 8, ...)\times$ the rms noise of the imaged data at each wavelength, 3.0 mJy for the 1.2 mm panels and 0.8 mJy for the 3.0 mm panels. The synthesized beam sizes are shown in the lower right corners of the imaged data in the first column.

Fit V (a & b) repeats the recipe of the χ^2 analysis, using a density model that comprises a radial power law with index p and a hollow-cone outflow with constant semi-opening angle α. As with Fit Ia, Fit Va assumes a dust opacity index of unity, whereas Fit Vb includes the dust opacity index as an additional parameter. As listed in Table 1, the two fits give

nearly identical results, both with each other and with the outcome of Fit I. The best fit power law index (Fit Vb) is $p = 1.65 \pm 0.05$, with outflow semi-opening angle $\alpha = 40° \pm 5°$, and dust opacity index $\beta = 0.74 \pm 0.10$.

In Figure 3.3, the additional columns of panels show images at both wavelengths made from the synthetic visibilities of the best fit model, and those with parameter values that differ by 2σ from the best fit, i.e. $p = 1.55$, $\alpha = 30°$ and $p = 1.75$, $\alpha = 50°$. The best fit spherically symmetric model is also shown to demonstrate the effect of adding the outflow cones. The quality of the match to the data is visible in (1) the extent of the apparent asymmetry, and (2) the number and spacing of the intensity contours. Note that the density gradient parameterized by p and the degree of asymmetry parameterized by α are nearly independent. The outflow model with $p = 1.65$ and $\alpha = 40°$ provides the best match to the imaged data, and has lower reduced χ^2 despite the additional fitting parameter.

The best fit density power law index is essentially unchanged from the spherically symmetric analysis. That these results should be so similar is partly a consequence of the adopted outflow geometry. The main effect of the outflow cone is to change the normalization of the intensity profile along the direction through the cone, but not to change the shape or power law index of the profile. This would not be the case for an outflow model without a constant opening angle. For instance, for a model where the opening angle decreases with distance from the protostar (e.g. a parabola), the intensity profile along the outflow axis becomes less steep as relatively less material is removed from the core at larger radii. The fitted power law index in such a model would be higher than for the simple cone model. As an example, consider an outflow geometry where the semi-opening angle is 50° at

500 AU, decreasing to 30° at 5000 AU; in this model, the intensity profile along the outflow axis has power law index that is ~ 0.15 less steep than for the constant opening angle case, or the profile along an axis perpendicular to the flow. While we have not analyzed this class of model in detail, since the outflow covers less than two quadrants of the sky, spatial averaging of the regions affected by the outflow and the regions that are unaffected suggests an uncertainty of roughly $\delta p \lesssim 0.15/2 \sim 0.08$, a small effect on fitted power laws.

The good agreement in the fitted opening angles for the simple cone model in this work and the extinction study of Harvey et al. (2001) may not be especially significant. While the consistency is encouraging, it most likely reflects the fact that the crude outflow model creates a detectable degree of oblate flattening only for semi-opening angles near 45°. For much largers opening angles, too much of the dense core is removed by the outflow and the core becomes disk like; for much smaller angles, the effect on the core is small, except in a small region at the poles.

3.5.3 Discussion

The analysis presented in the previous sections provides strong evidence that the density distribution power law index is less than 2.0 in the central 5000 AU ($20''$) region where the PdBI observations are sensitive. The best fit single power law for the density distribution has index of $p = 1.65 \pm 0.05$. This value should be considered an upper limit since including a central point source — the dominant contributor of systematic uncertainty — can reduce the value to $p = 1.47 \pm 0.07$. The remaining sources of systematic uncertainty considered, of which the most important is the radial dependence of the temperature distribution, likely

contribute a total uncertainty at the level $\delta p \lesssim 0.2$.

The Harvey et al. (2001) extinction study demonstrated a density index of very close to 2.0 ($p = 1.91 \pm 0.07$) over a 3500–25000 AU range in radius, indicative of an isothermal hydrostatic envelope, a result consistent with several different analyses of dust emission from single dish observations that probe similar spatial scales (Shirley et al. 2002, Motte & André 2001). The new interferometric dust emission data, which probes smaller scales, provides strong evidence that the density profile becomes less steep in the inner 5000 AU of B335. This conclusion agrees with the hints from detailed modelling of dust extinction indicative of a turnover in the density profile at a radius of about 6500 AU, as well as application of the Shu (1977) inside-out collapse model to molecular line observations (Zhou et al. 1993, Choi et al. 1995).

The inferred density profile of the B335 core conforms closely to the predictions in standard theories of isolated star formation (Shu 1977, Larson 1969, Penston, 1969) where an envelope with density power law index of $p = 2.0$ surrounds an inner region with a $p = 1.5$ distribution characteristic of material freely falling under the force of gravity. However, even with the contribution of a unresolved point source component, the specific Shu (1977) inside-out collapse model provides a worse fit to the data than does a simple power law. The local density index within the turnover (infall) radius in the inside-out collapse model is significantly less steep than $p = 1.5$, ranging from roughly unity to 1.5. Consequently, the inside-out collapse model cannot successfully match both the normalization of the visibility profile in the IRAM PdBI observations and the total flux within a large aperture measured with a single dish by Shirley et al. (2000). The constraint provided by the single

dish measurement — effectively the visibility information at zero-spacing that cannot be measured directly by the interferometer — is crucial to this analysis; without it, the density distribution power law index can be constrained only to within $\delta p \sim \pm 0.3$, not including contributions from systematic errors.

The images of B335 presented in Figure 3.3 demonstrate clear departures from spherical symmetry. The inner part of the globule appears significantly extended perpendicular to the outflow axis. This is in contrast to images of dust emission with lower angular resolution that show nearly spherical symmetry. While there are no robust predictions for the effect of the outflow on the density distribution, combining the power law density model with a very simple bipolar cone to describe the outflow improves the match to the data, but does not alter significantly the inferred shape of the radial variation in density.

Observations of B335 at longer baselines are needed to constrain the flux from any point source component that may be present at the center of the dense core. Such a component might be expected in the form of a circumstellar disk. Indeed, the maximal 1.2 mm flux of an unresolved component ($\sim$ 12 mJy) lies on the low end of the range expected for the B335 disk based on the subarcsecond submillimeter fluxes for Class 0 sources observed with the CSO-JCMT interferometer (Brown et al. 2000), perhaps related to the relatively low rotation rate of B335 (see Zhou 1995).

In the future, high resolution observations of B335 at submillimeter wavelengths may help to mitigate the uncertainties associated with the temperature distribution. Spatial information on the optically thin emission distribution at a third wavelength that is sufficiently short to be outside the Rayleigh-Jeans regime for the majority of the dense core

should allow for partly breaking the degeneracy between temperature, density and opacity. Such observations may be obtained with the Submillimeter Array (SMA), now under construction, or the Atacama Large Millimeter Array (ALMA).

3.5.4 A Physical Density Distribution for B335

Throughout the analysis presented so far, attention has been paid only to the power law index of the density distribution; the normalization has been absorbed in satisfying the constraint placed by the single dish 1.3 mm flux measurement of Shirley et al. (2000). To allow the results to be used in future modeling of B335, we now discuss the physical scale of the density distribution. The present study, in concert with the Harvey et al. (2001) extinction work, affords the unique position to propose a density distribution that satisfies both dust emission and extinction data over a range in radius from 500 AU to 25,000 AU.

For the adopted temperature distribution and mass opacity at 1.2 mm, the density within $r \lesssim 20''$ (5000 AU) is:

$$n(r) \simeq \begin{cases} 8.1 \times 10^5 \text{ cm}^{-3} \left(\frac{r}{10^3 \text{ AU}}\right)^{-1.65} & \text{for no point source} \\ 7.6 \times 10^5 \text{ cm}^{-3} \left(\frac{r}{10^3 \text{ AU}}\right)^{-1.47} & \text{for 12 mJy point source} \end{cases} \tag{3.5}$$

where n is the total number density in the gas ($n = n(H_2) + n(He) + \ldots = \rho/(\mu m_H)$, $\mu = 2.29$). Note that including the outflow as a hollow cone with semi-opening angle 40° increases by 14% the coefficient of the density distribution power law (and leaves the index unchanged).

For the envelope beyond $r \gtrsim 26''$ (6500 AU), the Harvey et al. (2001) extinction work

suggested an isothermal, hydrostatic, structure with r^{-2}, consistent with the results of the dust emission studies of Shirley et al. (2002) and Motte & André (2001). This envelope density distribution can be adopted into our model without affecting the inferred structure in the inner regions, since emission from the envelope is a negligible contribution at small impact parameters ($\lesssim 20''$), and is filtered out at large impact parameters by the antenna pattern ($20''$ FWHM at 1.2 mm). However, the correct normalization of the density distribution in the outer envelope relative to the inner regions is difficult to assess because the uncertainties involved in the extinction work (gas-to-dust ratio, reddening law) are different from those that arise in the dust emission studies (specific mass opacity, temperature structure), and the previous dust emission studies do not resolve the inner regions.

The analysis of the interferometer dust continuum data allows us to draw some conclusions about the behaviour of the density profile in the transition region between the two regimes, and hence to infer a consistent scale for the envelope. In order for any model to simultaneously match the normalization of the observed visibility profile and the Shirley et al. (2000) measurement of the flux within $r < 20''$, the local power law index in the transition region cannot decrease from the value measured in the inner region. The power law index must remain constant or become steeper. A simple continuation of the inner power law until reaching the envelope implies a density distribution for $r > 26''$ (6500 AU):

$$n(r) \simeq \begin{cases} 1.6 \times 10^4 \text{ cm}^{-3} \left(\frac{r}{10^4 \text{ AU}}\right)^{-2.0} & \text{for no point source} \\ 2.2 \times 10^4 \text{ cm}^{-3} \left(\frac{r}{10^4 \text{ AU}}\right)^{-2.0} & \text{for 12 mJy point source} \end{cases} \tag{3.6}$$

For the case of no point source, this composite density distribution gives an average power

law index of $p = 1.90$ over the 3500–25000 AU radius range sampled by the dust extinction data, precisely reproducing the extinction result ($p = 1.91 \pm 0.07$), and it gives an average power law index of $p = 1.80$ over the 1000–25000 AU radius range, which reproduces the result of Shirley et al. (2002). Remarkably, the normalization of this envelope distribution is also within 6% of the singular isothermal sphere.

3.6 Summary

We present a study of the density distribution of the protostellar collapse candidate B335 using continuum observations at 1.2 mm and 3.0 mm made with the IRAM PdBI. In summary:

1. We perform a detailed analysis of the interferometer measurements directly in the visibility domain, not in the image domain. Though computationally intensive, this approach avoids the limitations of standard Fourier inversion and deconvolution algorithms.

2. The PdBI visibility data strongly constrain the density distribution at radii from $\sim$ 500 AU to $\sim$ 5000 AU from the protostar. Within this inner region, the density distribution is well described by a single power law. The best fit power law index $p = 1.65 \pm 0.05$ (1 σ) is significantly less steep than values close to $p = 2.0$ derived for larger radii from analyses of dust emission and extinction. We consider the effects of various sources of systematic uncertainty on the derived value of p. Including a central source of point-like emission in the model, as might come from an unresolved accretion disk, reduces the power law index to $p = 1.47 \pm 0.07$. The remaining sources

of systematic uncertainty, of which the most important is the radial dependence of the temperature distribution, likely contribute a total uncertainty at the level of $\delta p \lesssim 0.2$.

3. The inferred density profile for B335, with a power law index close to $r^{-1.5}$ near the protostar within an r^{-2} envelope, matches the generic paradigm of gravitational collapse for isolated, low mass star formation. However, the specific inside-out collapse solution of Shu (1977) does not produce as good a fit to the dust emission data in the inner region as does a simple single power law, largely because of the shallow slope ($p \sim 1$) of the inside-out collapse solution just within the infall radius.

4. Images made from the visibility data show clear departures from spherical symmetry, with the inner part of the B335 core elongated perpendicular to the outflow axis. Including the outflow in the model fitting as a hollowed bipolar cone improves the match to the data and does not significantly change the derived radial density power law index from the value obtained in the spherically symmetric analysis. An outflow geometry where the opening angle decreases with distance from the protostar location would result in a slightly larger power law index, roughly $\delta p \lesssim 0.05$.

5. Observations that probe the subarcsecond millimeter continuum structure of B335 are needed to constrain the central point source contribution to the dust emission.

Acknowledgements

DWAH thanks Jonathan Jenkins for many useful discussions concerning statistics. We acknowledge the IRAM staff from the Plateau de Bure and from Grenoble for carrying out

the observations and for their help during the data reduction. We are especially grateful to Roberto Neri for his assistance. Partial support for this work was provided by NASA Origins of Solar Systems Program Grant NAG5-6266.

Chapter 4

Disk Properties and Density Structure of the Star-Forming Dense Core B335 [1]

Daniel W.A. Harvey, David J. Wilner, Philip C. Myers, & Mario Tafalla, 2003c *The Astrophysical Journal*, **in press**, astro-ph/0307105

---

[1]Based on observations carried out with the IRAM Plateau de Bure Interferometer. IRAM is supported by INSU/CNRS (France), MPG (Germany) and IGN (Spain).

Abstract

We present subarcsecond resolution dust continuum observations of the protostellar collapse candidate B335 made with the IRAM Plateau de Bure Interferometer at wavelengths of 1.2 and 3.0 mm. These observations probe to < 100 AU size scales and reveal a compact source component that we identify with a circumstellar disk. We analyze these data in concert with previous lower resolution interferometer observations and find a best fit density structure for B335 that consists of a power law envelope with index $p = 1.55 \pm 0.04$ ($r \lesssim 5000$ AU) together with a disk ($r < 100$ AU) of flux $F_{1.2\mathrm{mm}} = 21 \pm 2$ mJy. We estimate a systematic uncertainty in the power law index $\delta p \lesssim 0.15$, where the largest error comes from the assumed form of the dust temperature falloff with radius. This determination of the inner density structure of B335 has a precision unique amongst protostellar cores, and it is consistent with the $r^{-1.5}$ profile of gravitational free-fall, in accord with basic expectations for the formation of a star. The flux (and implied mass) of the compact component in B335 is typical of the disks around T-Tauri stars.

4.1 Introduction

The dense core in the B335 dark globule is generally recognized as the best protostellar collapse candidate. This dense core is nearby (250 pc, Tomita, Saito & Ohtani 1979), isolated, and nearly spherical. It contains a deeply embedded low luminosity young stellar object (3 $L_\odot$) discovered at far-infrared wavelengths by Keene et al. (1983) and detected by IRAS only at $\lambda \geq 60$ μm.

Detailed radiative transfer models based on the theory of inside-out collapse (Shu 1977) provide very good fits to spectral line profiles of the dense gas tracers CS and H_2CO observed at $10''$ to $30''$ resolution (Zhou et al. 1993; Choi et al. 1995), though recent studies have raised doubts about the inside-out collapse interpretation. Observations by Wilner et al. (2000) of the CS(5-4) line at higher angular resolution, $\sim 2''.5$ ($\sim$500 AU), show that the high velocity emission arises from the inner part of a bipolar outflow, not from the gravitational acceleration of gas close to the protostar. However, studies of starless cores show that some molecular species, in particular CS, are frozen out onto grains at densities characteristic of the inner regions of B335 (Caselli et al. 2002, Tafalla et al. 2002). If heating does not promptly desorb CS molecules from grain mantles, then this species likely makes a poor probe of the kinematics in the presumed infall zone.

Since the density field is strongly coupled to the velocity field, observations of long wavelength dust emission provide an alternative means to infer the dynamical state of the dense core. The intensity of the dust emission provides an integral along the line-of-sight of the product of the density and dust temperature. By modeling the dust temperature and specific mass opacity, the observed intensities can be used to constrain the density distribution. This approach has been applied extensively using large single-dish telescopes (e.g. Ward-Thompson, Motte & Andre 1999, Motte & Andre 2001, Visser, Richer & Chandler 2001, Shirley et al. 2000). But the central regions of the nearest protostellar cores are generally comparable in size to the beamwidths of single-dish telescopes and remain poorly resolved. The density structure at smaller scales must be probed using interferometers. So far, detailed modeling of millimeter interferometer data in this context has been rare

(Keene & Masson 1990, Hogerheijde et al. 1999, Harvey et al. 2003a, Looney, Mundy & Welch 2003).

Harvey et al. (2003a) recently analyzed observations of dust continuum emission at 1.2 mm and 3.0 mm from B335 on scales from 5000 to 500 AU. A single radial power law in density provided a good description of the data, with best fit power law density index $p = 1.65 \pm 0.05$. However, this result is subject to the major systematic uncertainty of the unknown contribution from a central compact source, whose presence would bias the derived density profile to be too steep. Such a compact source might be expected in B335 if the protostar is surrounded by an accretion disk. Here, we present new IRAM PdBI observations that probe directly the subarcsecond millimeter continuum structure of B335. These observations detect a compact source component and provide a measure of the previously uncertain level of point source "contamination" to the envelope emission, thereby allowing the inner density structure of B335 to be constrained with unprecedented precision.

4.2 Observations

Continuum emission from B335 was observed at 1.2 mm (246.5 GHz) and 3.0 mm (100 GHz) with the six antenna IRAM PdBI in a modified A configuration on 2003 March 05. Table 4.1 lists the observational parameters. The visibilities span a baseline range from 23 to 400 meters, the longest baselines available. This range overlaps with the earlier D configuration observations described by Harvey et al. (2003a), thereby enabling cross calibration.

Table 4.1. Summary of instrumental parameters

Parameter	1.3 mm	3.0 mm
Observation date	2003 Mar. 05	
Configuration	modified A (six antennas)	
Baseline range	23–400 m	
Pointing center (J2000)	$19^h37^m00\overset{s}{.}74$, $+7°34'10\overset{''}{.}8$	
Phase calibrators	J1751+096 & J1925+211	
Bandpass calibrator	3C 273	
Flux calibrator	MWC 349	
Primary beam FWHM	$20''$	$50''$
Observing frequency	246.5 GHz	100.0 GHz
RMS Noise	1.9 mJy	0.7 mJy

The pointing center and observing frequencies were chosen to be identical to the D configuration observations, to facilitate the joint analysis of the two datasets. The half-power field of view for the PdBI is $20''$ (5000 AU) at 1.2 mm and $50''$ (12500 AU) at 3 mm. The absolute flux scale was set using observations of the standard source MWC 349, assumed to be 1.77 Jy at 1.2 mm and 1.03 Jy at 3 mm. The estimated uncertainty in the flux scales is roughly 20%. Frequent observations of nearby calibrators J1751+096 and J1925+211 were used to determine time-dependent complex gains. Continuum visibility records were formed for each 60 s integration of the digital correlator, with 560 MHz bandwidth at 1.2 mm, and 570 MHz bandwidth at 3 mm. The bandpass was measured with observations of the strong source 3C 273. The data were calibrated using the IRAM software package *CLIC* and com-

prise a total of 6000 records at each wavelength. In addition to amplitude and phase, each record contains a variance measure, determined from the system temperatures and antenna gains.

4.3 Results and Analysis

We use the techniques developed by Harvey et al. (2003a) to analyze the structure of B335 using the interferometer measurements directly in the visibility domain, without producing images. While this approach is computationally intensive, it recognizes the limitations of standard Fourier inversion and deconvolution techniques, and it avoids many difficulties that may arise from the synthesized beam characteristics.

4.3.1 Presence of a Compact Component

Figure 4.1 shows the visibility data at 1.2 mm (*diamonds*) and 3.0 mm (*squares*), after binning logarithmically in (u, v) distance. The 1.2 mm data show a visibility profile that flattens with increasing baseline lengths beyond ~ 60 kλ. The start of this change in slope is also apparent in the 3.0 mm data. We interpret the flattening in the profiles as the separation between the extended envelope that dominates the flux at short baselines from a compact source component that persists to the longest baselines.

To determine the central position, and to test whether the compact component is resolved, we fit an elliptical Gaussian to the long baseline visibilities, $|(u, v)| > 100$ kλ. The fitted Gaussian is offset from the pointing center by $(2\farcs27 \pm 0\farcs01, -0\farcs93 \pm 0\farcs02)$, giving

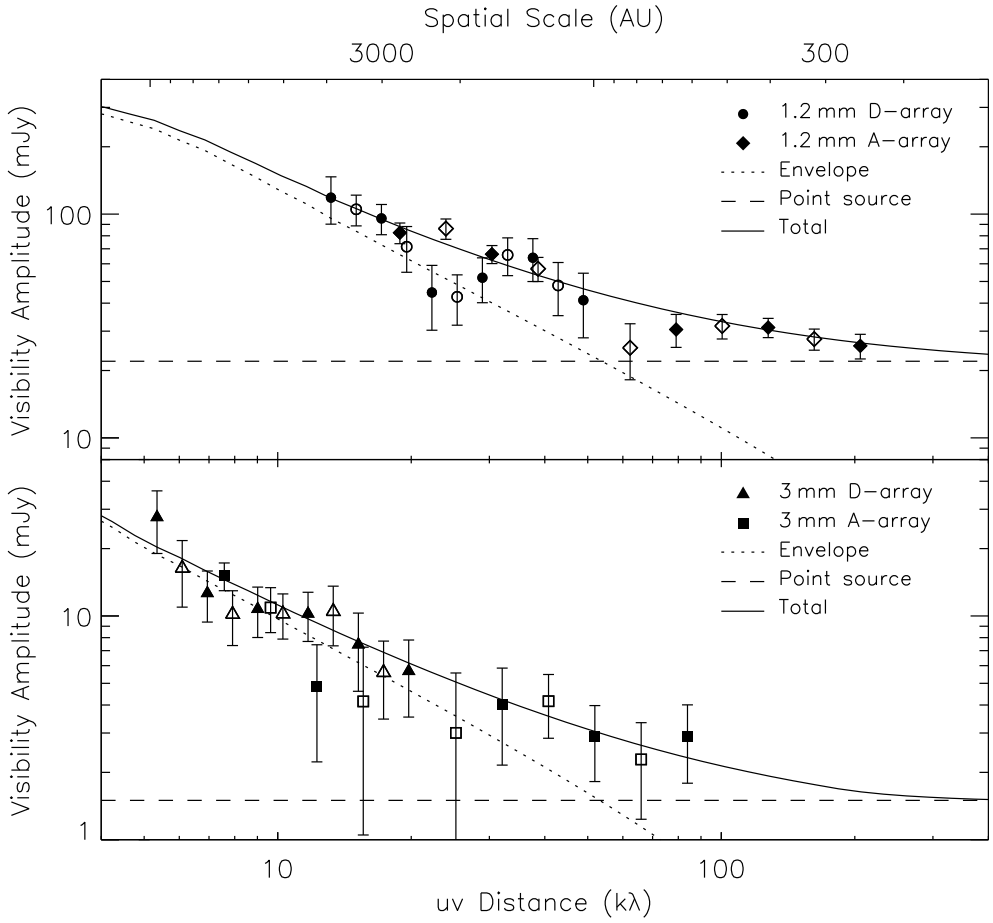

Fig. 4.1.— Binned visibility amplitude vs. (u, v) distance at 1.2 mm (upper panel) and 3.0 mm (lower panel) for the new IRAM PdBI observations of B335 together with the previous observations reported by Harvey et al. (2003). The derived calibration scalings have been applied to the two datasets. Note that for each dataset the bins oversample the data, and therefore the filled symbols are not completely independent from the open symbols. The best-fit model (solid line) comprises a power law density distribution in the inner part of the envelope with $p = 1.55 \pm 0.05$ (dotted line) and a point source of flux $F_{1.2\mathrm{mm}} = 21 \pm 2$ mJy at 1.2 mm (dashed line).

coordinates for the peak $\alpha = 19^{\rm h}37^{\rm m}00\overset{\rm s}{.}89$, $\delta = 7°34'10\overset{''}{.}9$ (J2000) consistent with earlier determinations of the protostar position. The uncertainty in the absolute position is likely considerably worse than the formal errors from this fit, since no extra effort was made to ensure especially accurate astrometry. The fitted Gaussian FWHM is $0\overset{''}{.}36 \pm 0\overset{''}{.}11 \times 0\overset{''}{.}19 \pm 0\overset{''}{.}06$, with position angle $14° \pm 15°$, which corresponds to semi-major axis 45 ± 14 AU and semi-minor axis 24 ± 8 AU. The formal errors on the fitted size are at the 3σ level, and they are at the level of the seeing disk size $\sim 0\overset{''}{.}1$ estimated from Gaussian fits to the phase calibrators.

Figure 4.2 shows an image made from the 1.2 mm long baseline visibilities in the standard way, which highlights the compact source component. We attribute essentially all of this compact flux component to thermal dust emission. Reipurth et al. (2002) detected a subarcsecond scale radio source at 3.6 cm at this position, elongated in the outflow direction, with variable flux < 0.4 mJy. However, assuming the free-free emission from this ionized radio jet has a typical flat spectral index, it makes a negligble contribution to the emission at 1.2 mm. The shape of the sythesized beam matches the shape of the fitted Gaussian, but since the fit is to the raw visibility data, the sythesized beam does not directly affect the results, aside from there being inherently more resolution (longer baselines) East-West than North-South. The orientation of the fitted Gaussian is consistent with a source that is elongated perpendicular to the axis of the bipolar outflow seen on larger scales (essentially East-West, e.g. Hirano et al. 1992). We therefore identify the compact component as a circumstellar disk. We caution that the fitted compact source size is only marginally resolved, and that the envelope emission may yet contaminate the signal, even on these subarcsecond

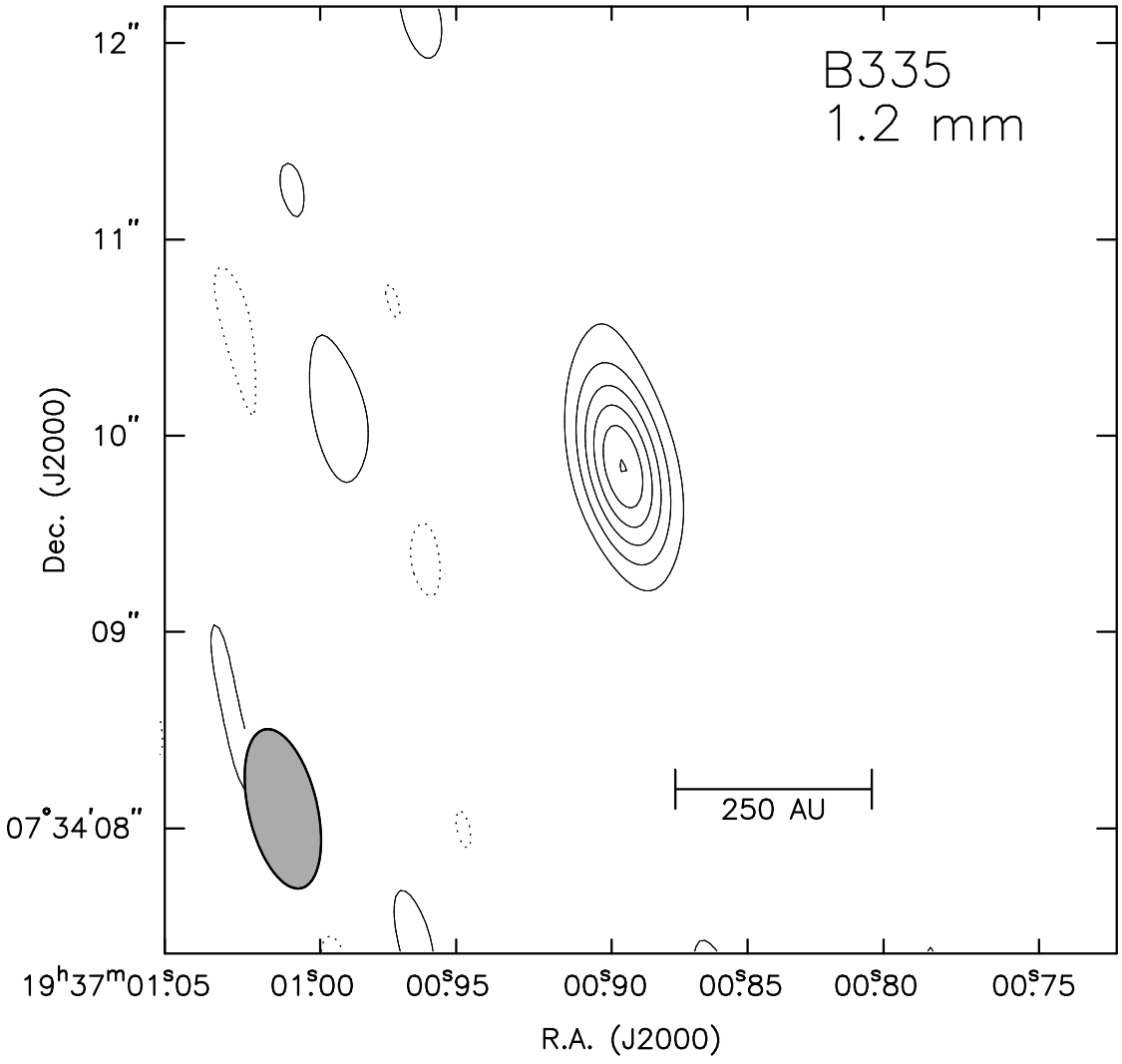

Fig. 4.2.— B335 image at 1.2 mm made from long baseline visibilities, $|(u,v)| > 100$ kλ. The contour levels are $\pm 2, 4, 6, ... \times 2.1$ mJy. Negative contours are dotted. The ellipse in the lower left corner shows the $0\farcs83 \times 0\farcs35$ p.a. 13° synthesized beam. There is significant flux in a nearly pointlike component with maximum dimension similar to that of known circumstellar disks.

size scales. In addition, if the compact component is a disk, then its outer radius is likely larger than the fitted Gaussian FWHM size, perhaps by a factor of up to ~ 2, because the emission profile of a disk with realistic density and temperature distributions is more centrally peaked than a Gaussian (Mundy et al. 1996, Wilner et al. 1996). This suggests a conservative upper limit of 100 AU for the disk radius.

4.3.2 Calculation of Model Visibilities

We compare the B335 visibilities from both antenna configurations to theoretical models of protostellar structure by constructing synthetic visibilities, taking account of (1) the dust continuum radiative transfer, and (2) the specifics of the observations, including the exact (u, v) sampling and primary beam attenuation. In brief, 1024×1024 pixel model intensity images (resolution $0\farcs1$ pixel^{-1} at 1.2 mm, $0\farcs2$ pixel^{-1} at 3 mm) are calculated using the full Planck function for the emissivity and integrating the radiative transfer equation through the model globule. Each model is normalized to a flux at 1.3 mm of 570 ± 90 mJy within a circular aperture (top-hat) of radius $20''$ based on the measurement of Shirley et al. (2000). This normalization effectively provides a measurement at zero-spacing of the interferometer and is essential for determining the envelope structure. Without this information, the model visibility profiles would float freely in normalization and the constraints that can be placed on the density structure are therefore much weaker (see e.g. Looney et al. (2003) where models with $p = 2$ and $p = 1.5$ generally cannot be distinguished.) Observations are simulated by performing an FFT, assuming a Gaussian shape for the primary beams (1.2 mm FWHM $20''$, 3 mm FWHM $50''$). The (u, v) sampling is achieved by interpolating

the real and imaginary parts of the resulting visibility grid. The center is fixed to match the position of the compact component from the elliptical Gaussian fit to the long baseline 1.2 mm data.

Compact Component.— The compact component of dust emission in B335 evident at long baselines is likely due to a circumstellar disk. Since the size of the compact component from the Gaussian fit ($\lesssim 0\farcs36$) is smaller than the fringe spacing on the longest baseline ($\sim 0\farcs6$), we calculate the contribution of this compact component to the visibilities by modeling it as an unresolved point-like source. We assume the compact component to contribute a flux $F_\nu \propto \nu^3$, for a disk that is optically thin at millimeter wavelengths with a dust opacity index β of unity (e.g. Beckwith et al. 1990). If instead the disk were partly optically thick at these wavelengths, then its spectral index might be closer to 2. Experiments with the fitting procedure showed that both the inferred 1.2 mm flux of the compact component and the envelope density distribution are not sensitive to this spectral index assumption, and we adopt the optically thin model. This lack of dependence on the disk spectral index occurs because the flux of the compact component at 3 mm is not tightly constrained due to the lower spatial resolution at this longer wavelength (see Figure 4.1).

Envelope Density Models.— We fix attention on the spherically symmetric broken power law models for the protostellar envelope density distribution, based on the success of this description in matching the previous lower resolution data. The effect on the inferred density profiles of departures from spherical symmetry caused by the bipolar outflow was investigated by Harvey et al. (2003a) and found to be small compared to other sources of systematic uncertainty (e.g. the dust temperature distribution). The density models are of

the form:

$$\rho_d(r) = \rho(R_0) \begin{cases} (r/R_0)^{-p} & \text{for } r \leq R_0 \\ (r/R_0)^{-2} & \text{for } R_0 < r \leq R_{\rm out} \end{cases} \tag{4.1}$$

The fixed outer power law index of 2.0, turn-over radius of $R_0 = 6500$ AU ($26''$), and outer radius of $R_{\rm out} = 0.15$ pc are based on the near-infrared dust extinction measurements of Harvey et al. (2001). The results are not sensitive to the outer boundary assumption due to the small field of view of the PdBI antennas.

Envelope Dust Temperature.— The models necessarily include assumptions about the dust temperature distribution, in addition to the density field. Based on the study of Shirley et al. (2002), we adopt the following for the temperature:

$$T_d(r) = \begin{cases} 10\ (r/R_T)^{-0.4}\ \text{K} & \text{for } r \leq R_T \\ 10\ \text{K} & \text{for } r > R_T \end{cases} \tag{4.2}$$

i.e the temperature falls as a power law, reaching a constant value of $T = 10$ K for radii beyond $R_T = 5000$ AU. This is a close approximation to the results of detailed calculations of balanced heating and cooling. For B335, an inner breakdown to this behavior is expected within a radius of $\lesssim 100$ AU, where the temperature gradient rises sharply due to the envelope becoming optically thick to infrared radiation. This scale is at the resolution limit of the new data, so emission from this warm central region would appear as an unresolved point source in our visibility data. Since the compact component of the flux is constrained by the long baseline data, this possible breakdown in the temperature distribution does not affect the inferred density profile of the envelope (for $r > 100$ AU), although it may contaminate the flux that we attribute to a circumstellar disk. To investigate the degree of

envelope contamination, we assume that the envelope density distribution extends to the center, and that the temperature increases steeply within a radius of 60 AU (Shirley et al. 2002). In this case the mass of the warm region is only 5×10^{-4} $M_{\odot}$. To contaminate the compact flux by 50% requires the temperature to increase within this region by $\sim$ 230 K above the assumed distribution, equivalent to an average temperature in the region of $\gtrsim$ 300 K. If the envelope density distribution is disrupted so that it does not extend to the protostar location, then it is even harder for the envelope to contaminate the disk flux.

Envelope Dust Opacity. — We assume that the dust opacity does not change with radius, although this approximation will likely break down in the innermost regions of the envelope where the temperature becomes high enough that the ice mantles evaporate (Ossenkopf & Henning 1994). For the dust opacity at millimeter wavelengths, we assume a power law $\kappa_{\nu} \propto \nu^{\beta}$ with index $\beta = 1$ (e.g. Looney, Mundy, & Welch 2000). In the absence of absolute calibration uncertainties, the spectral index β would control the relative normalization of the 1.2 mm and 3 mm profiles. In practice, the relative normalization of the 1.2 mm and 3 mm profiles from each of the antenna configuration are consistent with the assumed index, taking account the systematic uncertainties in the calibrations.

4.3.3 Fitting Model Parameters and Evaluating Fit Quality

We analyze the individual visibility records, and avoid binning the data to prevent loss of information. We maximize the probability distribution of a simultaneous fit to both

datasets, by minimizing a modified χ^2 of the form:

$$\tilde{\chi}^2 = \sum_{\lambda} \sum_{k=A,D} \left[\frac{(M_{\lambda,k} - 1)^2}{\sigma(M_{\lambda,k})^2} + \sum_i \frac{|Z_i - M_{\lambda,k} Z_i^{\rm mod}(p)|^2}{\sigma_i^2} \right] \tag{4.3}$$

where the Z_i are the visibility data points with uncertainty σ_i, and the $Z_i^{\rm mod}(p)$ are the data points for a model with power law index p. The sum extends over both wavelengths, and over observations from both array configurations. The parameters $M_{\lambda,k}$ allow us to include the observational uncertainties, namely the uncertainty in the flux calibration of each dataset (each wavelength from each configuration), and the $\sim$ 15% uncertainty in the Shirley et al. (2000) measurement used in the flux normalization. This is achieved by allowing the model visibilities to be scaled by the constrained parameter $M_{\lambda,k}$, assumed to be a Gaussian random variable with mean 1.0 and standard deviation $\sigma(M_{\lambda,k})$. We adopt $\sigma(M_{1.2{\rm mm},k}) = 0.25$ for the two 1.2 mm datasets, making the assumption of two independent Gaussian distributions contributing to the probability distribution of each scaling factor. While this is not quite accurate (since the normalization is part of both $M_{1.2{\rm mm},A}$ and $M_{1.2{\rm mm},D}$), this formulation reduces the number of fitted parameters and provides for realistic values of the scaling factors. These scaling factors essentially provide for the best possible cross-calibration for the observations from the two antenna configurations. For the two 3 mm datasets, we allow the scaling parameters to be free, by adopting $\sigma(M_{3{\rm mm},k}) \to \infty$, essentially to account for the uncertain dust opacity spectral index.

Since the models are non-linear in the fitting parameters, we analyze the uncertainty in the best-fit model parameters using the Monte Carlo technique known as the *bootstrap* (Press et al. 1992). In brief, the dataset is resampled n times, each time the fitting process is repeated and the best-fit parameters recorded, until the distribution of best-fit parameters

is well sampled. The width of the distribution provides an estimate of the uncertainty in the parameters that best fit the original dataset.

The best fit model has envelope density power law index $p = 1.55 \pm 0.04$ and a point source component of flux $F_{1.2\mathrm{mm}} = 21 \pm 2$ mJy. The constrained scaling parameters at 1.2 mm are $M_{1.2\mathrm{mm},A} = 1.4 \pm 0.1$ and $M_{1.2\mathrm{mm},D} = 0.77 \pm 0.06$. The free scaling parameters at 3 mm are $M_{3\mathrm{mm},A} = 1.4 \pm 0.2$ and $M_{3\mathrm{mm},D} = 1.09 \pm 0.15$. The unscaled best-fit model is offset to higher normalization than the D configuration 1.2 mm data, and to lower normalization than the A configuration 1.2 mm data. We interpret these results as most likely due to the uncertainties in the overall flux calibration of the two datasets, low for the former and high for the latter. The magnitudes of the scaling factors are consistent with this interpretation. In this context, the free scalings for the 3 mm datasets are close enough to unity that the data are consistent with an assumed dust opacity spectral index of unity. Figure 4.1 shows a plot of the various visibility datasets, renormalized by $1/M_{\lambda,k}$, binned in (u, v) distance, along with the best fit model, and the two components of the best fit model.

4.4 Discussion

4.4.1 Implications for B335 Envelope Structure

We find that the density profile of B335 has power law index $p = 1.55 \pm 0.04$ within the inner ~ 5000 AU. This result is remarkably consistent with the $p = 1.50$ expectation for free-fall collapse. The overall density structure of B335 can be obtained by combining the

inner behavior determined in the present study with the steeper outer falloff determined from near-infrared extinction work (Harvey et al. 2001) and low resolution millimeter and submillimeter studies (Shirley et al. 2000, Motte & André 2001). The extinction data showed an average power law index of $p = 1.91 \pm 0.07$ over the region 3500-25,000 AU, consistent with the $p = 2$ index characteristic of a hydrostatic region supported by thermal pressure (the index is not significantly affected by the small overlap with the region in which the index decreases). Joining these two regions together, for the adopted temperature distribution and mass opacity at 1.2 mm, the density distribution of molecular hydrogen is:

$$n_{H_2}(r) \simeq 3.3 \times 10^4 \text{ cm}^{-3} \begin{cases} \left(\frac{r}{6500 \text{ AU}}\right)^{-1.5} & 100 \text{ AU} \leq r \leq 6500 \text{ AU} \\ \left(\frac{r}{6500 \text{ AU}}\right)^{-2.0} & 6500 \text{ AU} < r \leq 25,000 \text{ AU} \end{cases} \tag{4.4}$$

The corresponding enclosed mass distribution is:

$$M(r) \simeq \begin{cases} 0.58\text{M}_\odot \left(\frac{r}{6500 \text{ AU}}\right)^{1.5} & 100 \text{ AU} \leq r \leq 6500 \text{ AU} \\ 0.58\text{M}_\odot + 0.87\text{M}_\odot \left(\frac{r}{6500 \text{ AU}} - 1\right) & 6500 \text{ AU} < r \leq 25,000 \text{ AU} \end{cases} \tag{4.5}$$

If one accounts for the asymmetry of the B335 core by modeling the outflow with a bipolar hollow cone, then the normalization of the density distribution away from the outflow must be increased by a small factor, $\sim 14\%$ for a 40° semi-opening angle.

This determination of the inner density structure of B335 has a precision that is unique amongst protostellar cores, and it provides the best evidence yet for the standard picture of isolated star formation, whereby the inner regions of an initially hydrostatic isothermal envelope collapse onto the center in near free-fall conditions (Shu, Adams & Lizano 1987). As noted by Harvey et al. (2003a), while the B335 density distribution is qualitatively

similar to the density distribution of the inside-out collapse model, the two distributions are quantitatively different in the inner regions. In the inside-out collapse model, the local density gradient within the infall radius is significantly less steep than $p = 1.5$, ranging from roughly unity to 1.5. Such a shallow density profile is ruled out by the dust emission analysis.

The new long baselines observations reveal the contribution of the central compact source to the total dust emission and thereby remove the previously dominant source of systematic error from the envelope density structure determination (see Harvey et al. 2003a). The remaining sources of systematic error, of which the most important is the detailed shape of the temperature distribution, likely contribute a systematic uncertainty of $\delta p \lesssim 0.15$. In the future, high resolution observations of B335 at submillimeter wavelengths may help to mitigate the uncertainties associated with the temperature distribution. Spatially resolved information on the optically thin emission distribution at a third wavelength that is sufficiently short to be outside the Rayleigh-Jeans regime for the majority of the dense core should allow for partly breaking the degeneracy between temperature, density and opacity. Such observations may be obtained with the Submillimeter Array (SMA) on Mauna Kea, which is soon to be commissioned, and eventually the Atacama Large Millimeter Array (ALMA) in Chile, now under construction. It is also clearly desirable to make high resolution spectral line observations of species not subject to depletion and unaffected by the bipolar outflow in order to best probe the dense core dynamics.

4.4.2 Disk Properties

The fitted flux of $F_{1.2\mathrm{mm}} = 21 \pm 2$ mJy from the B335 disk is typical of the (distance corrected) ~ 5 to 300 mJy range of fluxes from disks around the T Tauri stars observed by Beckwith et al. (1990) and Osterloh & Beckwith (1995). The disk flux is at the low end of the range for the disks in the Class 0 sources observed in the Perseus region by Brown et al. (2000) using the CSO-JCMT interferometer at 0.87 mm and by Looney, Mundy, & Welch (2003) using BIMA at 2.7 mm (for $\beta \approx 1$). However, the Perseus sample is highly biased, as the sources were chosen on the basis of their large millimeter fluxes.

The ~ 45 AU FWHM spatial scale of the compact component in B335 at 1.2 mm is similar to the sizes measured for the Perseus Class 0 disks (Brown et al. 2000), though it is not clear how accurately the Gaussian size measurement predicts the actual B335 disk radius. Given that disks result from conservation of angular momentum during the collapse process, a small disk radius and disk flux might be expected in B335 because of its relatively low rotation rate (Frerking, Langer & Wilson 1987, Zhou 1995). In the context of the Terebey, Shu & Cassen (1984) model of inside-out collapse with rotation, the centrifugal radius for B335 is predicted to be only 3 AU, or $0\farcs012$, far too small to resolve. However, such a small disk could not produce the observed 1.2 mm flux without an unfeasibly high dust temperature of $\gtrsim 1000$ K. The radius of the B335 disk is clearly much larger than predicted by the simple model of inside-out collapse with rotation.

The flux from the disk provides a measure of the disk mass, though the large uncertainty in the normalization of the dust opacity dominates the mass calculation. Assuming

$\kappa_{1.2\ \mathrm{mm}} = 0.02\ \mathrm{cm}^2\ \mathrm{g}^{-1}$, a simple estimate is $M_{\mathrm{disk}} = 0.004\,\mathrm{M}_\odot(50\ \mathrm{K}/\langle T_{\mathrm{disk}}\rangle)$, where $\langle T_{\mathrm{disk}}\rangle$ is the mass weighted mean temperature. Theoretical expectation for a flared, radiatively heated disk, suggest $\langle T_{\mathrm{disk}}\rangle \simeq 50$ K (Beckwith 1999), though fits to the spectra of the T Tauri disks in Beckwith et al. (1990) give temperatures that are generally lower by a factor of 2 to 3, and disk mass estimates that are higher by the same factor (occupying a range ~ 0.002 to 0.3 $\mathrm{M}_\odot$). For B335, the appropriate mean temperature may be higher than for a disk around a T-Tauri star because of the surrounding envelope with substantial optical depth in the infrared that inhibits cooling (Natta 1993). But since the B335 disk flux is typical of T Tauri stars, it seems likely that the disk mass is not unusually small or large. Given the link between accretion disks and bipolar outflows, perhaps this is not surprising given that B335 exhibits a bipolar outflow that is not at all unusual, with size, momentum and energy typical for a low mass protostar (Goldsmith et al. 1984).

4.5 Summary

We present new subarcsecond resolution dust continuum observations of the protostellar collapse candidate B335 made with the IRAM PdBI at wavelengths of 1.2 and 3.0 mm. We analyze these data together with previous PdBI observations reported by Harvey et al. (2003a) that provide short-baseline information. In summary:

1. The PdBI visibility datasets span baseline ranges from 15 to 400 meters, and the longest baselines marginally resolve a compact component distinct from the highly resolved protostellar envelope. We identify this compact component with a circumstellar

disk, although emission from a warm inner region of the envelope may also contribute to this flux. We place a conservative upper limit on the disk radius of $\simeq$ 100 AU, given the uncertainties in the details of its temperature and density structure.

2. We analyze the visibility data by comparison with synthetic observations constructed from models with a variety of physical conditions. We simultaneously constrain the envelope density distribution at radii from $\sim$ 100 to $\sim$ 5000 AU together with a point-like component to account for the disk. The best fit model has an envelope density power law index $p = 1.55 \pm 0.04$ within this region, with point source flux $F_{1.2\mathrm{mm}} = 21 \pm 2$ mJy (1 σ). Systematic uncertainties dominate the random uncertainties for the inferred density structure and contribute an estimated uncertainty of $\delta p \lesssim 0.15$. The dominant source of systematic error is most likely the simple treatment of the dust temperature distribution. Observations at submillimeter wavelengths may help to mitigate the uncertainties associated with the temperature distribution.

3. The density structure of the B335 core indicates an $r^{-1.5}$ inner region in gravitational free-fall surrounded by an r^{-2} envelope. However, the specific inside-out collapse solution of Shu (1977) does not reproduce the data because of the shallow slope ($p \sim 1$) of the inside-out collapse solution just within the infall radius.

4. The fitted characteristics of the compact source suggest the B335 disk is typical of disks observed around T Tauri stars, with radius $r \lesssim 100$ AU and mass $M \simeq 0.004\ \mathrm{M}_\odot\ (50\ \mathrm{K}/T_{\mathrm{disk}})$.

Acknowledgements

We thank Diego Mardones for his efforts on the D-configuration dataset. We acknowledge the IRAM staff from the Plateau de Bure and Grenoble for carrying out all the observations and for their help during the data reduction. Partial support for this work was provided by NASA Origins of Solar Systems Program Grant NAG5-11777,

Chapter 5

Limits on Radio Continuum Emission from a Sample of Candidate Contracting Starless Cores

Daniel W.A Harvey, David J. Wilner, James Di Francesco, Chang-Won Lee, Philip C. Myers, & Jonathan P. Williams 2002, *The Astronomical Journal*, **123**, 3025

Abstract

We used the NRAO Very Large Array to search for 3.6 cm continuum emission from embedded protostars in a sample of 8 nearby "starless" cores that show spectroscopic evidence for infalling motions in molecular emission lines. We detect a total of 13 compact sources in the eight observed fields to 5 σ limiting flux levels of typically 0.09 mJy. None of these sources lie within $1'$ of the central positions of the cores, and they are all likely background objects. Based on an extrapolation of the empirical correlation between the bolometric luminosity and 3.6 cm luminosity for the youngest protostars, these null-detections place upper limits of $\sim 0.1\ L_\odot (d/140\ \mathrm{pc})^2$ on the luminosities of protostellar sources embedded within these cores. These limits, together with the extended nature of the inward motions inferred from molecular line mapping (Lee et al. 2001), are inconsistent with the inside-out collapse model of singular isothermal spheres and suggest a less centrally condensed phase of core evolution during the earliest stages of star formation.

5.1 Introduction

Star formation occurs within molecular clouds, behind large column densities of obscuring dust that hinders observations of its earliest evolutionary stages. The "Class 0" objects, which are not detected at wavelengths shorter than the submillimeter, represent the youngest protostars observed, with inferred ages of $\sim 10^4$ years (see André, Ward-Thompson & Barsony 1993, André & Montmerle 1994). Even younger protostars need to be identified to improve our understanding of the first stages of protostellar collapse.

The "starless" dense cores, density enhancements within molecular clouds that show no evidence for embedded protostars, may represent an evolutionary stage of the star formation process prior to that of the Class 0 objects. Lee et al. (1999) recently surveyed more than 200 nearby starless cores in spectral lines of dense gas tracers. Seventeen cores were identified with evidence for infalling motions, as suggested by the presence of redshifted self-absorption in line profiles. These rare infall candidates provide an excellent chance to locate the very youngest protostars, whose low luminosity and reddened spectral energy distributions might have escaped detection at far-infrared wavelengths by the Infrared Astronomy Satellite (IRAS).

A possible method to identify extremely young protostellar objects makes use of the well-documented occurrence of simultaneous mass accretion (infall) with mass expulsion (outflow) during star formation. From a sample of 29 Class 0 and Class I protostellar sources, Anglada (1995) noted a strong correlation between 3.6 cm radio continuum luminosity and bolometric luminosity. The radio continuum emission arises from the shock-ionized inner regions of a collimated outflow, while the bolometric luminosity arises predominately from accretion (e.g. Rodriguez et al. 1982, Lada 1985). If outflow is inextricably linked to accretion, the presence of a very young protostar within a so-called "starless core" with evidence for infalling motions can be deduced from the detection of compact radio continuum emission. Using a variant of this concept, Visser (2000) found evidence for three candidate protostars in a sample of 40 Lynds starless cores by detecting high velocity ^{12}CO(2–1) emission from previously unknown outflows.

We present here observations of eight starless cores made with the Very Large Array

(VLA) of the National Radio Astronomy Observatory[1] to search for indications of embedded protostars through the detection of compact radio continuum emission from their nascent outflows. The eight cores observed are the nearest objects (< 250 pc) from the survey of Lee et al. (1999) that show redshifted self-absorption in at least two molecular spectral lines.

5.2 Observations and Data Reduction

The VLA observations of starless cores were made on 1999 March 6 and 1999 April 27 in the D configuration at 3.6 cm (8.46 GHz). The use of the VLA in its most compact configuration and at its most sensitive wavelength maximizes the instrument's utility for detecting faint sources of radio continuum emission. Table 5.1 lists the target cores, calibrators, synthesized beam sizes, and the rms noise levels achieved in the images. The central pointing positions for the cores were taken from Lee et al. (1999). The uncertainties in these positions with respect to the column density peaks are at the $\sim 15''$ level. For the March observations of 4 cores at 4–5 hours Right Ascension (in the Taurus region), 3C 48 was used as the flux calibrator (3.15 Jy at 3.6 cm). For the April observations of 4 cores at 15–20 hours R.A. 3C 286 was used as the flux calibrator (5.20 Jy at 3.6 cm). The flux calibration is expected to be accurate to better than 10%. Standard procedures in the AIPS software package were used for all data calibration and imaging.

For each field, sources were located within the $5\farcm3$ primary beam half power diameter

[1]The National Radio Astronomy Observatory is operated by Associated Universities Inc., under contract with the National Science Foundation.

Table 5.1. Dense Cores Observed at 3.6 cm

	Phase Center				RMS
				Beam	Noise
Source	α (J2000)	δ (J2000)	Calibrator	($''\times''$)	(μJy)
L183	$15^h54^m06.5^s$	$-02°51'39''$	1543−079	11.6×9.8	15
L158	16 47 23.2	−13 59 21	1543−079	13.5×9.8	16
L234E–S	16 48 08.6	−10 57 24	1707+018	12.9×9.9	18
L694–2	19 41 04.5	+10 57 02	1950+081	11.9×9.1	20
L1521F	04 28 39.8	+26 51 35	0432+416	10.3×9.1	22
TMC2	04 32 48.7	+24 24 12	0432+416	10.4×9.1	18
TMC1	04 41 33.0	+25 44 44	0432+416	10.4×9.1	17
CB23	04 43 31.5	+29 39 11	0432+416	10.3×9.1	18

using the AIPS routine *Search and Destroy*, with a flux threshold of 5× the rms noise in the cleaned image. Table 5.2 lists the positions and fluxes of the 13 detected sources from the 8 fields. These sources generally fall within the regions of extended molecular line emission, but none are located within $1'$ of the adopted positions for the column density peaks. This choice of criterion for positional coincidence is arbitrary, but it is likely that all the detected sources are background objects. Nevertheless, more millimeter/sub-millimeter observations must be done to locate the column density peaks with better accuracy, to substantiate the significance of the observed displacements. It remains conceivable that one or more of the 3.6 cm sources may be tracing smaller clumps of material embedded within the cores; this possibility could be tested by future higher resolution observations. The observed source counts are consistent with expectations for a background population. Based on a detection threshold of 0.09 mJy, the source properties from Condon (1984), and the calculation in the appendix of Anglada et al. (1998), on average 1.0 background sources are expected per field, for a total of 8 ± 3 sources, which is consistent within 2 σ of the detected number. For the strongest source, L1521F (1), a reliable match is found in the NRAO VLA Sky Survey (NVSS) point source catalog. The NVSS flux measurement at 21 cm (1.4 GHz) implies a radio spectral index for this source of -0.70 ± 0.02, which suggests synchrotron emission from a background radio galaxy. This source is also the only resolved member of the sample (the resolution of the cleaned images is $\sim 10''$). The remaining unresolved sources show no matches in the SIMBAD astronomical database.

Table 5.2. Sources Detected at 3.6 cm

Source	Position[a] α (J2000)	Position[a] δ (J2000)	Flux[b] (mJy)	Angular Displacement[c] ($''$)
L158 (1)	$16^h47^m16.7^s$	$-14°00'57''$	0.27	135
(2)	16 47 24.0	−14 01 15	0.37	115
L234E–S (1)	16 48 05.0	−10 59 20	0.55	128
(2)	16 48 06.5	−10 56 07	0.25	83
L694–2 (1)	19 40 57.2	+10 57 30	2.60	111
L1521F (1)	04 28 41.2	+26 53 55	10.75	142
TMC2 (1)	04 32 42.6	+24 23 24	0.24	96
(2)	04 32 54.2	+24 22 43	0.13	116
TMC1 (1)	04 41 25.4	+25 42 53	0.67	151
(2)	04 41 25.7	+25 43 49	0.75	113
(3)	04 41 39.0	+25 43 24	0.36	114
CB23 (1)	04 43 34.9	+29 38 05	0.14	79
(2)	04 43 35.0	+29 37 13	0.26	127

[a]Position errors are $\sim 1''$

[b]Corrected for primary beam attenuation

[c]From Phase Center in Table 5.1

5.3 Discussion

5.3.1 Bolometric Luminosity Limits

The lack of positional coincidence between any of the detected radio continuum sources and the centers of the starless cores suggests that none of these sources are associated with the cores. Hence, the observations allow us to place upper limits on the 3.6 cm radio continuum luminosity of any compact sources present in the cores, and thus, upper limits on their bolometric luminosities following Anglada (1995). Figure 5.1 shows the radio continuum and bolometric luminosity data for the 29 sources compiled by Anglada, together with a least-squares fit. The fitted correlation

$$\log\,[\,S_{3.6\,\mathrm{cm}}\,d^2\;(\mathrm{mJy\;kpc^2})\,]\;=\;(-2.1\pm0.1)\;+\;(0.7\pm0.1)\;\log\,[L_{\mathrm{bol}}\;(\mathrm{L_\odot})\,]$$

allows the observed trend to be extrapolated to lower luminosities, the regime of our sensitive VLA observations. While there is no observational support for the validity of this extrapolation, there are no changes expected in the relevant mechanisms at lower luminosity levels that would suggest a breakdown of the correlation.

For the 4 Taurus cores (L1521F, TMC2, TMC1, CB23) at a distance of 140 pc (Elias 1978), the correlation and 5 σ upper limits on the radio continuum luminosity imply bolometric luminosity limits of $L \lesssim 0.1$ L$_\odot$. For the three Ophiuchus cores (L183, L158, L234E–S) at a distance of 165 pc (Chini 1981), the implied limits are $L \lesssim 0.2$ L$_\odot$. For L694–2, at an assumed distance of 250 pc that derives from an association with the cloud complex harboring the B335 core (Tomita, Saito & Ohtani 1978), the implied bolometric luminosity limit is $L \lesssim 0.7$ L$_\odot$. Figure 5.1 shows the upper limits for the 3.6 cm luminosities as arrows.

The uncertainty in these limits due to the uncertainty in the fitted correlation is $\sim 50\%$.

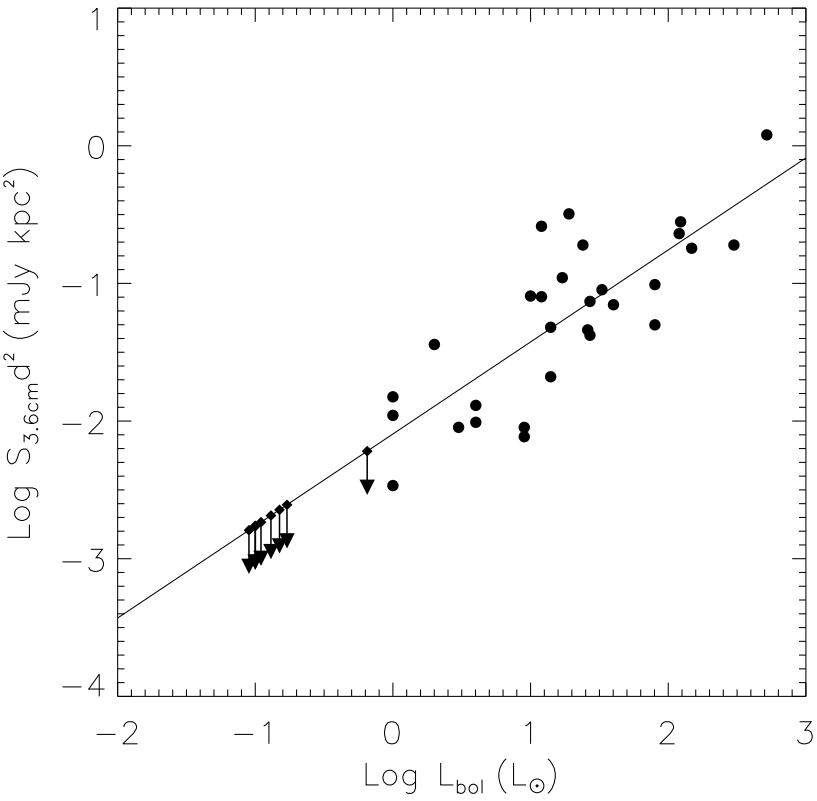

Fig. 5.1.— Log-log plot of 3.6 cm luminosity against bolometric luminosity for 29 outflow sources from Anglada (1995). A linear least-squares fit (r=0.79) indicated by the line has been used to extrapolate the observed trend to the sensitivity of our VLA observations. The fitted line has been used to calculate approximate upper limits on the bolometric luminosity of any protostar that might remain undetected in our observations. These upper limits are marked with arrows.

5.3.2 Comparison with IRAS Limits

In some circumstances, the limits on protostar luminosity implied by the VLA null-detections represent a substantial improvement on limits implied by the lack of an IRAS point source. For objects like starless cores that may be characterized by low temperatures, the limit from the longest wavelength IRAS band (100 μm) most strongly constrains luminosity. For isolated objects at high Galactic latitudes ($|b| > 50°$), the IRAS Point Source Catalog has a 50%-completeness limit of 1.0 Jy at 100 μm (Beichman et al. 1988). Nearer to the plane of the Galaxy, in more complicated regions such as Ophiuchus or Orion, the limits are often much higher due to extended "Cirrus" emission, and confusion with other sources. For example, VLA 1623, the prototypical Class 0 object, escaped detection by IRAS despite a fairly warm dust temperature ($T \simeq 20$ K) and substantial bolometric luminosity $L \sim 0.5$–2.5 $L_\odot$ (Andrè, Ward-Thompson & Barsony 1993). For this core, crowding with nearby sources causes the IRAS limiting flux to be raised to 45 Jy (Ward-Thompson 1993).

To calculate appropriate IRAS limits on bolometric luminosity, we assume that the spectral energy distributions of Class 0 objects and dense cores may be modeled reasonably well by modified graybodies of the form:

$$F_\nu = B_\nu(T_{dust})(1 - \exp[-\tau_\nu])\Omega_S \ ,$$

where $B_\nu(T_{dust})$ denotes the Planck function at frequency ν for a dust temperature T_{dust}, τ_ν is the dust optical depth, and Ω_S the solid angle subtended by the source (Gordon 1988, Ward-Thompson, André & Kirk 2001). The optical depth is proportional to the mass opacity of the dust, which is generally assumed to follow a power law with frequency. The

power law index is uncertain for the dust in dense cores, but bounded to a small range (Ossenkopf & Henning 1994). Here, we adopt $\tau_\nu \propto \nu^{1.5}$, as found for VLA 1623 by Andrè et al. 1993. The solid angle subtended by the source is constrained to be $\lesssim 2'$ in diameter, the resolution of IRAS at 100 μm. The maximum bolometric luminosity of such a graybody that may be hidden below a 1.0 Jy IRAS completeness limit is temperature dependent, roughly 1 $L_\odot$ for $T_{dust} = 10$ K, and falling to 0.1 $L_\odot$ for $T_{dust} = 14$ K, for a source at Taurus distance that is optically thin for $\lambda \gtrsim 100$ μm. This result is similar to the 0.05–0.1 $L_\odot$ limit for Taurus obtained by Myers et al. (1987), although the analysis presented here is more applicable to Class 0 objects.

Since the cores in this study are often viewed superposed against a parent molecular cloud, the 100 μm point source completeness limit may be worse than the nominal value of 1 Jy for isolated objects. For a ~ 3 Jy limit, a source as bright as 0.3 $L_\odot$ at 140 pc would have been undetected by IRAS even with a dust temperature of 14 K. The presence of even a small amount of (visible) warm dust would strongly increase the emission at the shorter wavelengths, and substantially lower the bolometric luminosity that could be hidden from IRAS. But such warm dust would be located close to the protostar, in the central regions of the core, in which case the solid angle subtended by the warm component would be small, and it would be shielded from view by absorption in the intervening layers of cold dust. To illustrate this scenario, consider an example of a cold core (14 K) that surrounds a warm dust component (40 K) that represents $\sim 1\%$ of the total dust mass. If this core has an optical thickness that is only one-tenth that of VLA 1623, making it optically thick for $\lambda \lesssim 20$ μm, then it could produce a bolometric luminosity of 0.1 $L_\odot (d/140 \text{ pc})^2$ but remain

undetected by IRAS with a 100 μm detection limit of $\sim$ 3 Jy. In these circumstances, the limits on protostar luminosity implied by the VLA null-detections are at least comparable to, and in many cases significantly lower than the corresponding IRAS limits.

5.3.3 Implications for the Infall Process

The null-detection of an embedded point source in a contracting core has implications for the nature of the infall process. Tafalla et al. (1998) presented a detailed discussion of these implications pertaining to L1544, a starless core in Taurus with evidence for infalling motions and comparable 3.6 cm radio continuum limits (Williams et al. 1999). In short, the low luminosities and extended sizes of the observed regions of inward motions are inconsistent with the widely applied model of inside-out collapse of a singular isothermal sphere (Shu 1977). In this model, collapse leads to the formation of a central point source with luminosity $L \sim a^6 t/GR_*$, where a is the effective sound speed, t is the time since the onset of collapse, and R_* is the protostellar radius (Shu, Adams, & Lizano 1987). Taking $R_* \simeq 3R_\odot$ (Stahler 1988) and $a \simeq 0.19$ km s^{-1} ($T \simeq 10$ K), the model predicts $L \sim 3\,(t/10^5\,\mathrm{yr})$ L$_\odot$. Infall onto a disk would reduce this luminosity (Kenyon et al. 1993), but these very young objects undetected by IRAS show no evidence for disks, nor are large disks predicted at such early times (Terebey, Shu & Cassen 1984). In the context of the Shu model, and using the Anglada correlation between radio continuum luminosity and bolometric luminosity, for an embedded source at Taurus distance to remain undetected by our VLA observations would require $t \lesssim 4 \times 10^3$ years, corresponding to an infall radius of only $R_{\mathrm{inf}} \lesssim 8 \times 10^{-4}$ pc. For a source at Ophiuchus distance, the corresponding values are

$t \lesssim 7 \times 10^3$ years, and $R_{\rm inf} \lesssim 1 \times 10^{-3}$ pc, while at the greater distance of L694–2, the values are $t \lesssim 2 \times 10^5$ years, and $R_{\rm inf} \lesssim 0.04$ pc. Lee et al. (2001) have computed sizes for the infalling regions in six of the eight cores that were observed in this study (TMC2, TMC1, L183, L158, L234E–S, and L694–2) by analyzing the extent of redshifted self-absorption in lines of CS and N_2H^+. The estimated infall radii range from 0.07 pc for L158 up to 0.17 pc for TMC1, and are typically 0.1 pc. The method used to calculate these radii is fairly simple, and more detailed modelling may refine the exact values. Nevertheless, the observed infall radii are very much larger than the limits on radii derived from the strict luminosity constraints found here assuming the inside-out collapse scenario. Moreover, the ambipolar diffusion process in a strongly sub-critical core apparently cannot explain the high velocities of infalling material observed in these cores (Lee et al. 2001; Ciolek & Mouschovias 1995). The cores studied here represent a sample whose inward motions are inconsistent with the standard theories of low mass star formation.

5.4 Summary

We used the VLA to search for 3.6 cm radio continuum emission from embedded outflows in eight "starless cores" that show evidence for infalling motions in the profiles of molecular spectral lines (Lee et al. 1999). We detected a total of 13 compact sources of radio continuum emission. None of the sources are within an arcminute of the column density peaks, and the source counts are consistent with expectations for a background population. Based on these apparent null-detections and an observed correlation between outflow luminosity and bolometric luminosity from protostellar objects, we place approximate upper limits on the

luminosities of any embedded protostars (with uncertainty $\sim 50\%$) of $\lesssim 0.1\ L_\odot (d/140\ \mathrm{pc})^2$. These limits, together with the extended nature of the inward motions inferred from molecular line mapping (Lee et al. 2001), are inconsistent with the inside-out collapse model of singular isothermal spheres and suggest a less centrally condensed phase of core evolution during the earliest stages of star formation.

Acknowledgements

This research has made use of the SIMBAD database, operated at CDS, Strasbourg, France.

Chapter 6

Envelope Structure of Starless Core L694-2 Derived from a Near-Infrared Extinction Map

Daniel W.A. Harvey, David J.W̃ilner, Charles J.L̃ada, Philip C. Myers, & João F. Alves 2003b, *The Astrophysical Journal*, in press, astro-ph/0308143

Abstract

We present a near-infrared extinction study of the dark globule L694-2, a starless core that shows strong evidence for inward motions in the profiles of molecular spectral lines. The J,H, and K band data were taken using the European Southern Observatory New Technology Telescope. The best fit simple spherical power law model has index $p = 2.6 \pm 0.2$, over the ~ 0.036–0.1 pc range in radius sampled in extinction. This power law slope is steeper than the value of $p = 2$ for a singular isothermal sphere, the initial condition of the inside-out model for protostellar collapse. Including an additional component of extinction along the line of sight further steepens the inferred profile. A fit for a Bonnor-Ebert sphere model results in a super-critical value of the dimensionless radius $\xi_{\rm max} = 25 \pm 3$. This unstable configuration of material in the L694–2 core may be related to the observed inward motions. The Bonnor-Ebert model matches the *shape* of the observed density profile, but significantly underestimates the *amount* of extinction observed in the L694–2 core (by a factor of ~ 4). This discrepancy in normalization has also been found for the nearby protostellar core B335 (Harvey et al. 2001). A cylindrical model with scale height $H = 0.0164 \pm 0.002$ pc ($13.5'' \pm 5''$) viewed at a small inclination to the axis of the cylinder provides an equally good radial profile as a power law model, and it also reproduces the asymmetry of the L694–2 core remarkably well. In addition, this model provides a possible basis for understanding the discrepancy in the normalization of the Bonnor-Ebert model, namely that L694–2 has prolate structure, with the full extent (mass) of the core being missed by analysis that assumes symmetry between the profiles of the core in the plane of the sky and along the line-of-sight. If the core is sufficiently magnetized then fragmentation may be avoided, and

later evolution might produce a protostar similar to B335.

6.1 Introduction

Molecular line surveys of nearby dark clouds have identified a large sample of dense cores (e.g. Benson & Myers 1989), of which roughly half are associated with young stellar objects detected by the IRAS (Beichman et al. 1986). The properties of these cores have been adopted in the standard model of isolated star formation whereby a slowly rotating, nearly spherical core makes a star/disk system via "inside-out" collapse (Shu, Adams & Lizano 1987). In this picture, a "starless" dense core represents the earliest stage of the star formation process. The physical conditions in this early stage have a profound impact on the evolution of protostars towards the main sequence. The initial density structure, particularly in the innermost regions, affects the collapse dynamics and the time dependence of the mass accretion rate (Foster & Chevalier 1993), and therefore many of the observable properties of protostars, including luminosity.

While the standard theory has proved very successful in many predictions (see the review of Shu et al. 1993), its weakest foundation arguably lies in the adopted initial conditions (André, Ward-Thompson & Barsony 2000). In the simplest case where a spherical starless core loses turbulent and magnetic support and relaxes to a balance between gravity and thermal pressure, an r^{-2} density distribution is established and the core collapses from the inside-out with a constant mass accretion rate (Shu 1977). Alternatively, if collapse begins before the density distribution fully relaxes, then a central region of relatively con-

stant density remains and the mass accretion rate is an order of magnitude larger at early times (Foster & Chevalier 1993). This phenomenon has been identified with the youngest "Class 0" protostars, which exhibit especially powerful outflows (Henriksen, Andre & Bontemps 1997; Andre, Ward-Thompson & Barsony 2000). In another case, a starless core with a logotropic equation of state develops a nearly r^{-1} density law and the mass accretion rate during collapse increases rapidly with time (McLaughlin & Pudritz 1997).

Better observations of starless cores are needed to measure appropriate initial conditions. Molecular hydrogen, the main mass constituent, cannot be observed directly in these cold (T<10 K) dense regions. The most robust tracer of mass is provided by dust. (Molecular line emission is compromised by excitation effects and severe depletion.)

Most of the detailed information on starless core structure comes from observations of dust emission, using data from submillimeter bolometer cameras (e.g. Ward-Thompson, Motte & Andre 1999, Shirley et al. 2000, Visser, Richer & Chandler 2001). The intensity of the dust emission provides an integral along the line-of-sight of the product of the dust temperature and density. An important conclusion from these studies is that starless cores appear to show flat density profiles in their inner regions, with extended envelopes that fall off rapidly in power law fashion. However, the regions of relatively constant density are poorly resolved by the low angular resolution available in the submillimeter. Moreover, the interpretation of the flat central density gradients has been called into question: more sophisticated analysis including self-consistent temperature calculations predict much smaller regions of flattening, or no flattening at all, in large part because the cores are cooler in their deep interiors than assumed previously (Evans et al. 2001, Walmsley et al. 2001).

Observations of dust extinction provide a more reliable measure of column density than observations of dust emission, mainly because extinction is not sensitive to gradients of dust temperature. Historically, this method has been impossible to apply to small regions of high extinction because of poor sensitivity and a paucity of background stars, even in the infrared where the extinction is much less than in the optical (e.g. Bok & Cordwell 1973, Jones et al. 1980, 1984). The development of large format near-infrared array cameras has sparked renewed interest in the technique (Lada et al. 1994, Alves et al. 1998, Alves, Lada & Lada 1999, 2001, Harvey et al. 2001).

Harvey et al. (2001) describe deep near-infrared extinction measurements toward B355, arguably the best protostellar collapse candidate, using the Hubble Space Telescope (HST). The B335 system contains a deeply embedded young stellar object, and exhibits molecular line profiles well fit by inside-out collapse (Zhou et al. 1993, Choi et al. 1995). The shape of the density profile determined from the deep extinction data provide the best evidence yet in support of inside-out collapse theory. Alves, Lada & Lada (2001) used the color excess method to study the starless core B68 with data from the the European Southern Observatory (ESO) New Technology Telescope (NTT). The B68 system is much less centrally condensed than B335, with lower peak column density, and it was easily penetrated with the sensitivity available from the ground. The extinction map of B68 suggests a hydrostatic equilibrium structure, with density distribution best described by the equations of a pressure confined, self-gravitating, isothermal sphere (Ebert 1955, Bonnor 1956).

The examples of B68 and B335 represent milestones in the early evolution of low-mass stars, but they do not show the density structure of a forming dense core, or the density

structure at the onset of collapse. The recent identification of contracting starless cores presents an opportunity to study this important intermediate evolutionary phase. There are now at least 7 "strong" infall candidates among the starless cores, based on observations of molecular line profiles with redshifted self-absorption in a systematic search of more than 200 targets (Lee, Myers & Tafalla 1999). Molecular line maps of these objects provide strong evidence of inward motions, with speed ~ 0.1 km s^{-1} over a radius of ~ 0.1 pc (Lee, Myers & Tafalla 2001). The physical basis for these motions is unclear. The speeds are subsonic and may be associated with condensation through ambipolar diffusion, or perhaps a magnetically diluted gravitational collapse (Ciolek & Basu 2000). Alternatively, pressure driven motions due to the dissipation of turbulence may be responsible (Myers & Lazarian 1998).

L694–2 is the best of these sources for extinction work, since it is viewed against a very high density of background stars near the Galactic plane ($l = 44.9°$, $b = -6.6°$), and at the same time there is no significant reddening by additional clouds along this line-of-sight. This isolated, round, dense core is situated close to the protostar B335 in the sky, probably associated with the same molecular cloud complex. This association suggests a distance of 250 pc (Tomita, Saito & Ohtani 1979), consistent with recent estimates of 230 ± 30 pc (Kawamura et al. 2001). But unlike B335, L694–2 is starless, with no evidence of an embedded luminosity source from IRAS or any indication of bipolar outflow (Visser 2000, Harvey et al. 2002). Analysis of dust emission suggests a steep outer profile with flattening of the density gradient within a radius of a few thousand AU (Visser 2000), but suffers from the probably inaccurate assumption of an isothermal temperature distribution (Evans

et al. 2001) In this paper we present a near-infrared color excess study of L694–2, using observations made at the ESO NTT. These data probe the density distribution between radii of 0.03 pc (6000 AU) to the outer edge of the globule at $\sim$ 0.15 pc, where the core merges into a more extended distribution of gas.

6.2 Observations and Data Reduction

6.2.1 The Near-Infrared Color Excess Technique

We provide here a brief review of the Near-Infrared Color Excess technique for measuring the structure of a dense core. For a more detailed description of the method, the reader is referred to Lada et al. (1994) and Harvey et al. (2001).

The basic method is to measure the near-infrared color excess for stars background to a dense core:

$$\mathrm{E(H-K)} = (\mathrm{H-K})_{\mathrm{observed}} - (\mathrm{H-K})_{*} \ , \tag{6.1}$$

where $(\mathrm{H-K})_{*}$ is the intrinsic color of the star. The color excess is directly proportional to the dust column density. Thus color excess may be converted to gas column density via the near-infrared extinction law and an assumed gas-to-dust ratio. These column density estimates can be used to determine the overall density structure of the obscuring core.

In practice, the method does not require a knowledge of the intrinsic colors of the individual extincted stars. The proximity of the near-infrared filters to the Rayleigh-Jeans region of the spectrum for main sequence and giant stars means that the intrinsic colors

are small, $0 < (H - K)_* < 0.3$ (Koornneef 1983). A statistical correction to their observed colors may be obtained empirically from the background stellar population (provided it is sufficiently spatially uniform).

6.2.2 NTT Observations

Observations of L694–2 were made on 2001 June 8 using the Son of Isaac (SofI) infrared camera on the ESO NTT. The SofI camera has 1024×1024 pixels with size $0\farcs29$, giving a $5'$ field of view. Each basic observation consisted of a mosaic of ten dithered sub-images, each with a total exposure time of 30 seconds, made up of 5 co-adds of 6 seconds. Dithering offsets were randomly chosen within a $40''$ box. Observations were made with filters J, H, and K_s[1]. Figure 6.1 shows a Digital Sky Survey (DSS) image of the L694–2 region with the NTT observed field indicated.

The data reduction and calibration was done in IRAF following the standard dark/flat/sky subtraction procedures, using a running flat. The typical seeing during the night was $0\farcs7$.

Photometry

Stars were identified in each image using the *SExtractor* program. Photometry was performed for all non-saturated stars using the *apphot* package in IRAF. A series of 3, 4, and 5 pixel apertures was used for every star. Aperture corrections were calculated for each aper-

[1]The K_s filter is medium-band version of the standard K filter, that avoids both the atmospheric absorption feature at 1.9 μm and radiation from the thermal background beyond 2.3 μm

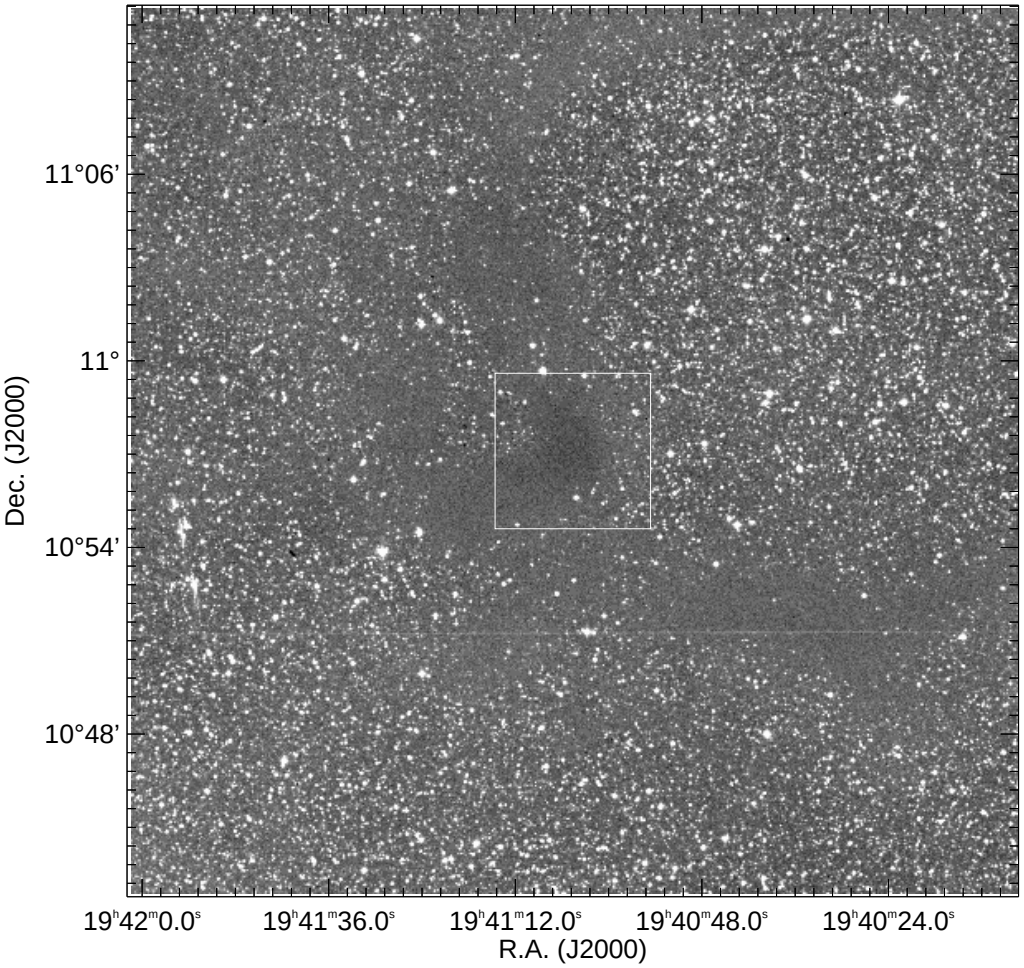

Fig. 6.1.— Digital Sky Survey POSS II image (Red plate) of the region containing L694–2. The field observed with the NTT is shown as a white box. The core appears to be a dense knot in an extended and filamentary distribution of molecular gas.

ture based on the seeing in the image using a regression to aperture corrections calculated for 23 previous observations with the NTT (Huard, private communication). While the 4-pixel aperture was used to produce the final photometry catalogues, the combination of the three measurements was used to eliminate spurious detections and blended stars (roughly 4% at H, K_s), based on whether the measurements were consistent with the predicted uncertainties at a 1.5 σ level.

Due to a not perfect alignment of the Large Field objective on the NTT, stellar images are radially elongated in the Northern part of the field of view. This elongation affects a strip of about 150 pixels and smoothly disappears moving toward the center of the field. Although this distortion does not create astrometric problems, it does mean that aperture photometry with a constant aperture correction will lead to systematic errors in the magnitudes of the stars in the affected region. We have dealt with this effect by applying additional spatially dependent aperture corrections. Each image was divided into a 4×4 grid, and we calculated the ratio of the median FWHM in each region to the median FWHM in the Southern (bottom) half of the image. The results were consistent between the three filters, and the most conservative (smallest) value was taken for each region in the grid. The resulting grid of spatially dependent seeing FWHMs was used to calculate the appropriate additional aperture corrections in each region. The additional correction are zero in the Southern half of the images, and are largest in the four Northern-most regions, where the FWHM of the point-spread function is typically 20% larger. In all cases, the corrections are less than 0.06 magnitudes in size for the 4-pixel aperture, and the colors are even more robust, with largest correction of only $H - K_s = -0.013$.

The World Coordinate System in the images was fixed using the *imwcs* routine written by Doug Mink and stars from the US Naval Observatory A2.0 Catalog (Monet et al. 1998). The coordinate system is accurate to within an arcsec in RA and Dec. Finally, correct zeropoints were calculated using 182 matches in the 2 Micron All Sky Survey (2MASS) point source catalog. The registration with the 2MASS zeropoints is accurate to $\sim 1\%$ in each filter. The 2MASS zeropoints are themselves accurate to a similar level.

The limiting magnitudes are 19.5 at J, 18.9 at H, and 18.5 at K_s, corresponding to a 0.25 magnitude error limit (signal to noise of 4) and a completeness of roughly 80%. The final photometry catalog contains 1451 stars detected at both H and K_s.

6.2.3 Reddening Law and Conversion between CIT and SofI/NTT Colors

Carpenter (2001) provides extensive conversion relations between 2MASS colors and magnitudes with those for other filter systems. Of particular interest to us here are the conversion to the ESO filter system (as used for our observations) and the California Institute of Technology (CIT) filter system (as used during our extinction study of B335). Conversion relations are also presented in Bessell & Brett (1988). Unfortunately, both the Carpenter and Bessell & Brett conversions are derived over a very small range in H – K colors, generally $H - K \lesssim 0.5$, and perhaps can not be trusted for the reddest stars in our catalog.

For the purposes of the present study, we divide our attention to two issues concerning the photometric systems: 1) how the intrinsic $H - K_s$ colors of stars in our catalog relates to their H – K on the CIT system; 2) how the color-excess $E(H - K_s)$ is related to $E(H - K)$ on the CIT system. The 2MASS conversion relations are sufficient to address (1), while (2)

can be investigated by studying a color-color diagram of the stars in our study. At the low colors ($H - K < 0.3$) intrinsic to main sequence and giant stars, the conversions from our instrumental colors to the 2MASS system are negligibly small compared to the systematic uncertainties ($\lesssim 0.01$), due to our registration with 2MASS zeropoints. For the intrinsic colors (ie $J - H < 0.6$, $H - K < 0.3$), the transformations between our colors and the CIT system are therefore:

$$(J - H) = 1.076(J - H)_{CIT} - 0.043 \quad (6.2)$$

$$(H - K_s) = 1.026(H - K)_{CIT} + 0.028 \quad (6.3)$$

with an uncertainty of ~ 0.01.

Figure 6.2 shows a color-color diagram for the subset of stars in the catalog with signal-to-noise of > 10 in each filter. The solid lines on the plot show the loci of unreddened main sequence and giant stars, while the two dashed lines show the expected reddening zone for these stars, using the standard reddening relations (Rieke & Lebofsky 1985), assuming $E(J-H) = 1.076E(J-H)_{CIT}$ and $E(H-K_s) = 1.026E(H-K)_{CIT}$ — an extrapolation of the low-color transformations. The reddening vectors follow the stellar colors remarkably well, even out to a color of $H - K \sim 1.5$. This suggests that the reddening law can be modified easily to a form $A_V/E(H - K_s)$ using $A_V/E(H - K_s) \simeq 1.026 * (A_V/E(H - K)) = 16.3$, while introducing little extra systematic error compared to that intrinsic to the reddening law itself.

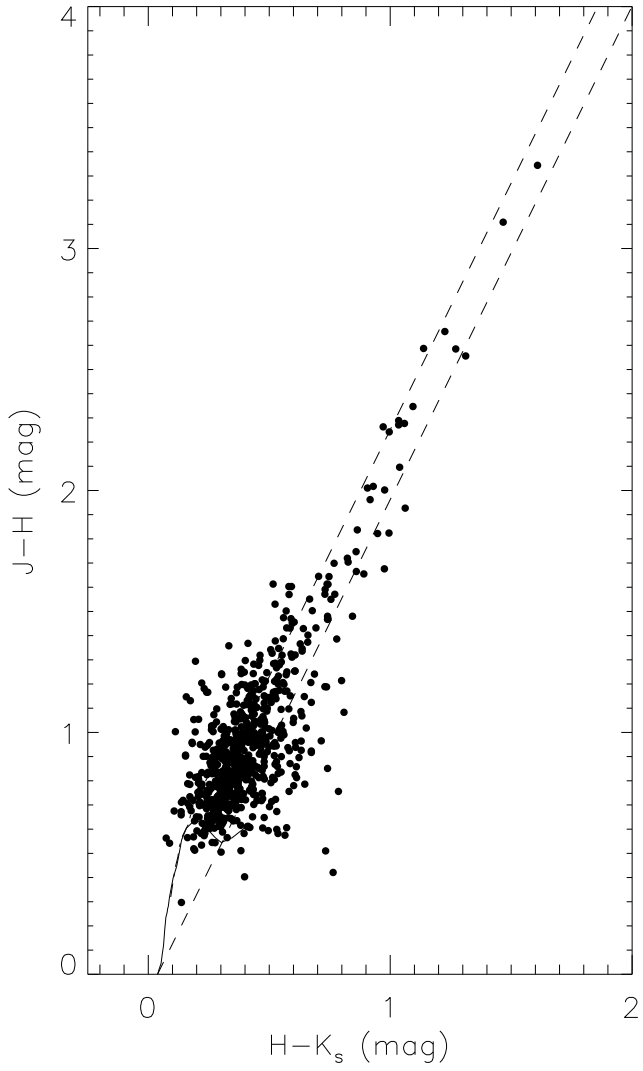

Fig. 6.2.— JHK$_s$ color-color diagram for the stars near L694–2 with signal-to-noise > 10. See text for discussion.

6.3 Results and Analysis

6.3.1 The Background Population Mean Color and Dispersion

The DSS image of L694–2 in Figure 6.1 shows that the core is associated with an extended filamentary structure of extinction. This lower level extinction extends away from the core towards the South-East and the North. To characterize the background population, we therefore study the stellar properties in the Western half of the images, considering only stars that are more than 2.′5 from the peak of the mm-wave emission. This minimum radius was chosen on the basis of minimizing any remaining extinction, but retaining enough stars to draw reliable conclusions about the background properties. This "background" region contains a total of 221 stars detected at both H and K_s. These stars have mean color of $\overline{H - K_s} = 0.35$ and standard deviation of $\sigma(H - K_s) = 0.21$.

The mean color is somewhat larger than expected for an unreddened stellar population, since the intrinsic colors of main sequence and giant stars span the narrow range $0 < H-K < 0.3$, and suggests that the stars in question are not entirely free from extinction. This conclusion is also supported by comparison with our results for the stellar background near B335, a globule that lies very close to L694 on the sky ($< 4^\circ$ away), and is probably even associated with the same parent molecular cloud. The mean color and standard deviation for the stellar population at a distance of between 2.′5 and 3' from the B335 center are $\overline{H - K} = 0.26$ and $\sigma(H-K) = 0.21$, which transform to $\overline{H - K_s} = 0.29$ and $\sigma(H-K_s) = 0.22$. Those values are very similar to the results found here. Off field images in the B335 vicinity showed that the true background properties became $\overline{H - K} = 0.13$ and $\sigma(H - K) = 0.16$,

corresponding to $\overline{\mathrm{H}-\mathrm{K}_s} = 0.16$ and $\sigma(\mathrm{H}-\mathrm{K}_s) = 0.17$. As a test for similarity between the L694 and B335 background, we have compared the luminosity functions for the L694 "background" with the deep H-band luminosity function that was calculated in the B335 study ($N(m < H) = 5.4(H/14.17)^{9.56}$ stars arcmin^{-2}, for $H > 14.17$). The luminosity functions are entirely indistinguishable to within the counting noise. We therefore conclude that the B335 background properties represent a reliable measure of the background to L694, and adopt those properties in favor of the values calculated for the stars near the Western edge of the L694 image.

6.3.2 Color Excess Distribution near L694–2

Figure 6.3 conveys much of the information from the NTT/SofI observations of L694–2. The left-hand plot is a pseudoimage in that the two axes are spatial, the apparent brightness of a star at H-band determines its "size", and the value of its $\mathrm{H}-\mathrm{K}_s$ color determines its "color". The upper right-hand plot displays the radial dependence of the $\mathrm{H}-\mathrm{K}_s$ colors out to $200''$ (0.24 pc at 250 pc distance) from the center. The lower right-hand plot shows the radial colors convolved with an annular Kernel that is a Gaussian of logarithmic width 10% in radius, in order to better highlight the profile of the H – K colors. Superposed are the standard deviation (dashed line), and standard error (dotted line) at each convolved point, the former indicating the spread of colors at each radius, and the latter indicating the uncertainty in the mean color at each radius. The origin in every plot is given by the position of peak emission in the $\mathrm{N_2H^+}$(1–0) spectral line measured at the Berkeley Illinois Maryland Array (BIMA) by Jonathon Williams and collaborators (unpublished

observations): R.A.=19:41:04.44, Dec.=10:57:00.9 (J2000). The uncertainty in the position of this peak is around 2″. As can be seen from the pseudoimage, the region of highest column density is extended towards the South-East corner of the image. The region is marked in the image with dashed lines. This structure is also visible in the DSS image of the region in Figure 6.1, and is associated with an extended filamentary structure of gas. To prevent confusion, stars within this region have been omitted from the radial-color plot. Of the 1451 stars in the image detected at H & K with $S/N > 4$, 199 stars have impact parameters smaller than 83″ or 0.1 pc, of which 14 lie in the "bar" region. The detected star closest to the N_2H^+ peak is at 28″ (0.034 pc) distance. This star is also the reddest in the sample and has color $H - K_s = 2.17$, corresponding to over 30 mag of equivalent visual extinction. In addition there is a star at impact parameter 30″ (0.036 pc) that is well detected at $K_s = 16.05 \pm 0.03$, but too red to be detected at H. Based on the assumed H-band limit of 18.9, where the magnitude error is ~ 0.25, this star provides a lower limit of $H - K_s > 2.81 \pm 0.25$ ($A_V > 40$).

The major features of Figure 6.3 are: (1) a strong gradient in the H – K colors as one approaches the N_2H^+ peak; (2) many fewer stars detected close to the center; (3) a central region of column density that is so high that it cannot be penetrated; (4) reddening in the stars changing behavior and flattening off beyond about 83″ or 0.1 pc, apparently the boundary/edge of the dense core and a more extended distribution of gas; and (5) regions of high color excess that extend to the image edge in the South-East, and part-way to the image edge in the North — the shape of these regions match the profile of L694–2 in the DSS image, and highlight the somewhat filamentary nature of the L694 region.

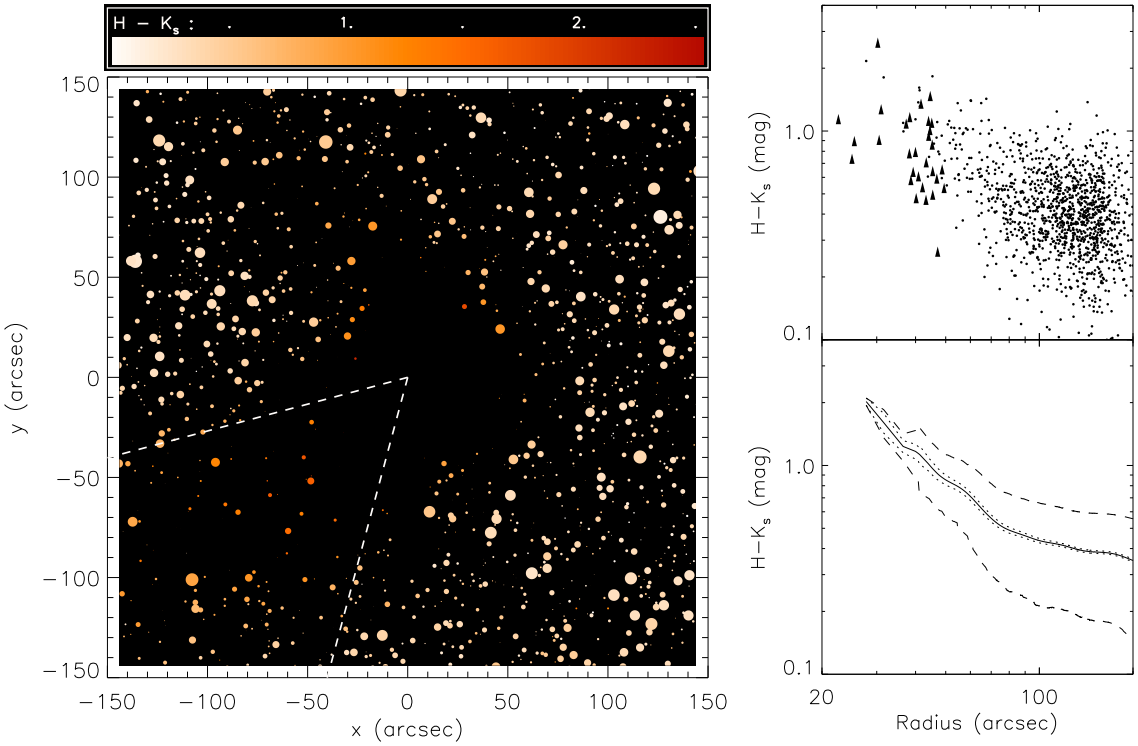

Fig. 6.3.— Left: Pseudoimage of the NTT/SofI observations; the axes are spatial, H magnitude determines a star's "size", and $H - K_s$ determines its color. The image contains 1451 stars detected in both filters. The dashed line indicates a bar-like structure of extinction that extends a significant distance from the core. Upper right: $H - K_s$ color against radius out to 200″ from the nominal center of L694–2. There is a steep gradient toward this location. Stars within the dashed region in the pseudoimage are omitted from the plot. Photometric error bars are not shown as they cause confusion with such a large number of stars. Lower limits on $H - K_s$ are marked as upward-pointing triangles. Lower right: smoothed $H - K_s$ color against radius out to 200″ from the nominal center of L694–2 (solid line), with ± one standard deviation (dashed line) and ± one standard error (dotted line). See text for further explanation.

6.3.3 Theoretical Models of the L694–2 Density Distribution

We describe several theoretical models for the density distribution of L694–2 and evaluate the success of these models in light of the extinction data. The models considered are not meant to comprise an exhaustive list. They include Bonnor-Ebert spheres, inside-out collapse, simple power law descriptions, and Plummer-like models. We also discuss filamentary models in the context of departures from spherical symmetry.

Inside-Out Collapse Models

There is a substantial literature of theoretical work by Frank Shu and colleagues describing the density structure of collapsing dense cloud cores, starting from the initial condition of a singular isothermal sphere (SIS). The density distribution of the SIS falls off as $\rho \propto r^{-2}$, where r is the radius, with the normalization of the density determined by the effective sound speed. For L694–2, Lee et al. (2001) have measured the FWHM of the N_2H^+ line to be 0.25 km s^{-1}. If we assume a central temperature of 9 K based on the models of Evans et al. (2001), then this suggests an effective sound speed of $a = 0.20$ km s^{-1} with a turbulent component of $a_{\rm turb} = 0.093$ km s^{-1}. The static initial condition in the inside-out collapse model is therefore given by:

$$\rho_{\rm static}(r) = \frac{a^2}{2\pi G r^2} \tag{6.4}$$

$$= 1.0 \times 10^{-20}\ {\rm g\,cm^{-3}} \left(\frac{a}{0.20\,{\rm km\,s^{-1}}}\right)^2 \left(\frac{r}{0.1\,{\rm pc}}\right)^{-2} \tag{6.5}$$

$$n_{H_2}(r) = 2.2 \times 10^3\ {\rm cm^{-3}} \left(\frac{a}{0.20\,{\rm km\,s^{-1}}}\right)^2 \left(\frac{r}{0.1\,{\rm pc}}\right)^{-2}, \tag{6.6}$$

where the conversion to a molecular hydrogen number density assumes a mean molecular weight of 2.3.

The simplest scenario is the spherically symmetric collapse (Shu 1977). In this model, a spherical wave of collapse propagates outwards from the center at the effective sound speed. The radial distance that the wave has traveled, sometimes called the infall radius, is the only additional parameter that defines the density distribution. Inside the infall radius, conditions approach free fall, with the density taking the asymptotic form $\rho \propto r^{-3/2}$. Harvey et al. (2001) describe deep near-infrared extinction measurements toward B355, arguably the best protostellar collapse candidate. This system, which contains a deeply embedded young stellar object, exhibits molecular line profiles well fit by inside-out collapse (Zhou et al. 1993, Choi et al. 1995). The shape of the density profile determined from the deep extinction data provide the best evidence yet in support of inside-out collapse theory, in particular the r^{-2} fall off for the envelope and inner turnover towards free-fall. Recent observations of dust emission from B335 using mm-wave interferometry have shown that the inner density distribution is very close to $\rho \propto r^{-3/2}$, although the way in which the density asymptotes to this behavior does not quite agree with the exact details of the inside-out collapse model (Harvey et al. 2003a).

In the inside-out collapse model, a central point source with luminosity $L \sim a^6 t/GR_*$ is formed. For L694–2, the limits on the luminosity of any embedded point source of $L \lesssim 0.3$ $L_\odot$, combined with the extended inward motions inferred from molecular line mapping (Lee et al. 2001), are inconsistent with the inside-out collapse model. Nevertheless we consider this model due to its success in describing the density structure of B335.

Bonnor-Ebert Models

Bonnor-Ebert models are pressure-confined isothermal spheres, for which the solution remains finite at the origin (Ebert 1955, Bonnor 1956). In common with the singular isothermal sphere, the initial condition for inside-out collapse, they are solutions of a modified Lane-Emden equation (Chandrasekhar 1967):

$$\frac{1}{\xi^2}\frac{d}{d\xi}\left(\xi^2\frac{d\psi}{d\xi}\right) = \exp\left(-\psi\right) \ , \tag{6.7}$$

where $\xi = (r/R_0)$ is the dimensionless-radius, $R_0 = a/\sqrt{4\pi G\rho_c}$ is the (physical) scale-radius, and $\psi(\xi) = -\ln(\rho/\rho_c)$ is a logarithmic density contrast, with ρ_c the (finite) central density. Unlike the singular solution, the Bonnor-Ebert solutions do not diverge at the origin. Instead, the boundary conditions are that the function ψ and its first derivative are zero at the origin.

The above equation can be solved by division into two first order equations which can then be tackled simultaneously using numerical techniques (in our case a 4th order Runge-Kutta method). There is a family of solutions characterized by a single parameter — the dimensionless outer radius of the sphere, $\xi_{\rm max}$. For a given sound speed and a particular choice of the shape of the density curve (i.e. $\xi_{\rm max}$), there is one additional degree of freedom: the physical scale of the model. This additional degree of freedom has often been removed by implementing an additional constraint, for example by fixing the outer radius, or the total mass of the globule. However, if such a constraint is applied, it is important to make some estimate of its uncertainty, and take that uncertainty into account in the fitting process in order to properly interpret both the systematic and random errors in $\xi_{\rm max}$.

Configurations with dimensionless outer radius $\xi_{\rm max} > 6.5$ are unstable to gravitational collapse (Bonnor 1956). The gravitational collapse of Bonnor-Ebert spheres has been studied numerically by Foster & Chevalier (1993). They find that collapse begins in the flat inner region, with the peak infall velocity at the "shoulder" of the density distribution. The flow asymptotically approaches the Larson-Penston solution at the origin at the time of and prior to the formation of a central core, as material from the flat region collapses into the center. These large early accretion rates last for a short time. If the cloud is initially very centrally condensed (i.e. $\xi_{\rm max} \gg 6.5$) the later stages of infall closely resemble Shu's inside-out collapse of a singular isothermal sphere.

Recently, Alves, Lada & Lada (2001) used the color excess method to study B68, a starless core, with data from the ESO NTT. The B68 system is much less centrally condensed than L964-2, and has much lower column density at the center (only about 30 magnitudes of equivalent visual extinction). The Alves et al. (2001) extinction map of B68 suggests that the density structure is well described by a Bonnor-Ebert sphere with dimensionless outer radius slightly in excess of critical: $\xi_{\rm max} = 6.9 \pm 0.2$. A highly super-critical Bonnor-Ebert sphere was found to fit the near-infrared extinction in protostellar collapse candidate B335 (Harvey et al. 2001). The model, with $\xi_{\rm max} = 12.5 \pm 2.6$ was indistinguishable from the inside-out collapse model over the range in radius where stars were detected, $r \gtrsim 14''$ (0.017 pc). Subsequent observations of dust emission with IRAM PdBI have shown power-law behavior ($p \sim 1.5$) in the inner region and rule out the Bonnor-Ebert model. However, the Bonnor-Ebert sphere is a hydrostatic model, and since the central regions of B335 are clearly not in equilibrium (presence of YSO, outflow, infall), it is not surprising that

the model does not accurately describe the inner density structure of B335. The physical interpretation of the inward motions detected in L694–2 by Lee et al. (2001) is unclear. If the motions represent a phase of condensation, then the density structure of the core may be well described by a supercritical Bonnor-Ebert model.

Power Law models

The singular isothermal sphere represents a special case of the family of power law models for density structure: $\rho(r) \propto r^{-p}$. Other special cases include the free-fall model ($p = 1.5$) and the logatropic model ($p = 1$), where the gas is governed by a logatropic equation of state (McLaughlin & Pudritz 1997).

Visser (2000) fitted a broken power law model to SCUBA observations of L694–2. The radial profile of the dust emission from the core was fit by an isothermal model that had a flat gradient in the inner regions ($\rho \propto r^{-0.8}$ for $r < 0.04$ pc or $32''$), surrounded by a steep $\rho \propto r^{-2.7}$ envelope. No uncertainty in these power-law indices is quoted, but nevertheless the profile represents a very unstable arrangement of material, and is consistent with the large inward motions detected by Lee et al. (2001). The analysis is based on an assumed constant temperature distribution. However, recent modeling suggests the dust temperature will decrease towards the center of a starless core (Evans et al. 2001). This decrease in the temperature may be what causes the flattening in the emission profile in the inner regions, and a density profile that does not turn-over at all cannot be ruled out. The turnover radius measured by Visser should perhaps be construed as an outer limit, since a more physical temperature profile would inevitably produce a smaller value.

Plummer-like Models

The Plummer-like model is an empirical model suggested by Whitworth & Ward-Thompson (2001) that captures the essential observed properties of pre-stellar cores with a minimum of free parameters. These properties include: 1) density distributions that combine flat inner profiles (ρ ~constant, to $\rho \propto r^{-1}$) with steep outer profiles (up to $\rho \propto r^{-4}$); 2) dynamical timescales that reproduce the short-lived (few$\times 10^4$ yr) high accretion-rate ($\gtrsim 10^{-5}$ M$_\odot$ yr^{-1}) nature of the class 0 protostellar phase, and the longer-lived (few$\times 10^5$ yr) slower accretion-rate ($\lesssim 10^{-6}$ M$_\odot$ yr^{-1}) nature of the class I phase; 3) extended and roughly uniform velocity fields, $v \sim 0.1$ km s^{-1} over $r \sim 0.1$ pc.

The model assumes that when a prestellar core becomes unstable against collapse at time t=0, it is static and approximates to a Plummer-like density profile (Plummer 1911), of the form:

$$\rho(r, t = 0) = \rho_{\rm flat} \left[\frac{R_{\rm flat}}{(R_{\rm flat}^2 + r^2)^{1/2}} \right]^{\eta} \tag{6.8}$$

The initial density is therefore uniform for $r \ll R_{\rm flat}$, and falls off as $r^{-\eta}$ for $r \gg R_{\rm flat}$. This is similar to the broken-power law model fitted to L694–2 by Visser (2001).

Subsequent evolution of the model is calculated assuming a negligible internal pressure, with the cloud therefore undergoing free-fall collapse. Collapse proceeds analogously to the Foster & Chevalier simulations of collapsing Bonnor-Ebert spheres: a large initial accretion rate as material from the uniform density region collapses onto the origin (associated with the Class 0 phase), followed by a more sedate accretion of the steep envelope. During the collapse process the central density profile steepens, asymptotically approaching $r^{-3/2}$, but

the outermost profile stays virtually unchanged. The velocity distribution is at early times peaked at the shoulder of the density distribution, but the inward motions in the central regions eventually reaches and exceeds this value after one free-fall time.

Whitworth & Ward-Thompson (2001) propose a fixed value of $\eta = 4$ in the model in order to reproduce the relative lifetimes and accretion rates for the Class 0 and Class I phases, and point out that for $\eta \leq 3$ the mass of the protostellar core will diverge due to an infinite reservoir of mass. However, in reality any core is likely to be pressure-truncated at some point by its interaction with the interstellar medium (c.f. Bonnor-Ebert sphere), which circumvents this theoretical problem with $\eta \leq 3$. Moreover, the observed dust-emission profiles of L694–2 (Visser 2001), and starless core L1544 (Lee et al. 2003) are better reproduced with a value of $\eta = 3$.

The model is highly optimistic in that it attempts to reproduce the density and velocity structure of pre-stellar, Class 0 and Class I sources. The model provides a useful framework for interpreting observations of pre-stellar cores, particularly of the inward velocity fields which cannot be explained in the context of a true (hydrostatic) Bonnor-Ebert sphere. In the case of Class 0 objects, the model is unable to reproduce the density structure of B335, the best studied of such sources, which has outer density profile that is very close to that of an isothermal sphere $\rho \propto r^{-2}$, and is significantly more shallow than that of the Plummer-like model.

Filamentary Models

The complex containing L694–2 provides an example of filamentary structure that is common to many molecular cloud complexes (see e.g. Schneider & Elmegreen 1979). Such structure can be produced by a variety of physical processes. Mechanisms that are well known to trigger star formation, such as cloud-cloud collisions, compression by a shell of a supernova remnant, and encounters with an ionization front surrounding an OB star all produce sheet-like cloud structures. Magnetic support might also result in an initially flattened cloud (e.g. Mouschovias 1976). Filamentary structures will probably result from the fragmentation of such sheet-like clouds (e.g. Larson 1985, Nagai et al. 1998). Observations of starless cores suggest that they are generally elongated in approximately a 2:1 ratio (Myers et al. 1991). This provides obvious motivation for investigating filamentary models, and is consistent with the picture of dense core formation in which a parent molecular cloud becomes flattened into a sheet, and fragments into filaments which then fragment further into dense cores.

The equilibrium structure of polytropic and isothermal cylinders has been studied by Ostriker (1964). The density is a function of the radial coordinate only: $\rho(r) = \rho_c/(1 + r^2/8H^2)^2$, where $H = a/\sqrt{4\pi G\rho_c}$ is the scale height that is equivalent to the scale radius R_0 in the Bonnor-Ebert analysis. The density is uniform near the axis of the cylinder but decays ever more rapidly with increasing radius, asymptoting to a power law of index $p = 4$ for $r \gg H$. Half the mass is encircled at a radius of $r_m = \sqrt{8}H$. The filament is supported radially by pressure gradients, but is unstable in the direction along its axis. Contraction will proceed initially along this direction. For an isothermal filament, the length beyond

which it becomes unstable to fragmentation is roughly four times the half-mass radius (Larson 1972, Bastien 1983).

It is interesting to note that the density distribution of the isothermal cylinder is a special two dimensional case of the Plummer-like model, with $r_m = \sqrt{8}H = R_{\rm flat}$, $\eta = 4$ (the value proposed by Whitworth & Ward-Thompson 2001), and with a physical basis for the normalization of the density profile. A cylindrical model can therefore reproduce the observational properties of pre-stellar cores that provided the motivation for the Plummer-like models. In addition, because the isothermal cylinder and the Bonnor-Ebert sphere both represent equilibria between self-gravity and gas pressure, the spherically averaged density profile of an isothermal cylinder can also mimick closely that of a Bonnor-Ebert sphere, in particular a flat inner region with a steeply falling envelope (Boss & Hartmann 2001). The recent success of the Bonnor-Ebert and Plummer-like models therefore provides strong encouragement for studying this type of model.

6.3.4 Fitting Model Parameters and Evaluating Fit Quality

We evaluate the goodness of fit for these various model density distributions by calculating a reduced χ^2, defined as:

$$\chi^2_\nu = \frac{1}{N-m} \sum \left(\frac{\mathrm{E(H-K}_s)_i^{\rm NTT} - \mathrm{E(H-K}_s)_i^{\rm model}}{\sigma_i^{\rm NTT}} \right)^2 , \qquad (6.9)$$

where m is the number of free parameters in the model being fitted, and the sum extends over a particular subset of N stars taken from the total number detected in both H & K_s filters. The values of the observed color excess $\mathrm{E(H-K}_s)_i^{\rm NTT}$ and the uncertainty $\sigma_i^{\rm NTT}$ are

calculated using the properties of the unreddened stellar background population near B335 (see Section 6.3.1), assuming each star to have an intrinsic color of $(\overline{\mathrm{H}-\mathrm{K}_s})_{\mathrm{BG}} = 0.16$, with an uncertainty of $\sigma_{\mathrm{BG}} = 0.17$:

$$\begin{aligned} \mathrm{E}(\mathrm{H}-\mathrm{K}_s)_i^{\mathrm{NTT}} &= (\mathrm{H}-\mathrm{K}_s)_i^{\mathrm{NTT}} - (\overline{\mathrm{H}-\mathrm{K}_s})_{\mathrm{BG}} \\ &= (\mathrm{H}-\mathrm{K}_s)_i^{\mathrm{NTT}} - 0.16 \ , \end{aligned} \tag{6.10}$$

$$\begin{aligned} \sigma_i^{\mathrm{NTT}} &= \sqrt{\sigma_i^2 + \sigma_{\mathrm{BG}}^2} \\ &= \sqrt{\sigma_i^2 + 0.17^2} \ , \end{aligned} \tag{6.11}$$

where σ_i is the uncertainty in the observed (H – K) color of a given star. This procedure implicitly assumes that the photometric errors (σ_i) and the intrinsic (H – K) colors both have Gaussian distributions. This is an adequate approximation to the actual distribution of background colors, and sufficiently good that the fitting results are not sensitive to it.

In order to include stars at low impact parameter that provide lower limits on $\mathrm{E}(\mathrm{H}-\mathrm{K}_s)$ (ie stars that are detected at K but not at H), we modify the sum to include any "limit stars" for which the lower limit on $\mathrm{E}(\mathrm{H}-\mathrm{K}_s)$ is not met. The color excess and uncertainty of these measurements are given by: $\mathrm{E}(\mathrm{H}-\mathrm{K}_s)_i^{\mathrm{NTT}} = \mathrm{H}_{\mathrm{lim}} - \mathrm{K}_i - 0.16$, and $\sigma_i^{\mathrm{NTT}} = \sqrt{\sigma_i^2 + 0.17^2 + \sigma(\mathrm{H}_{\mathrm{lim}})^2}$, with $\sigma(\mathrm{H}_{\mathrm{lim}}) = 0.25$ for $\mathrm{H}_{\mathrm{lim}} = 18.9$.

Since these models are non-linear in the fitting parameters, we analyze the uncertainty in the best-fit model parameters using a Monte Carlo technique known as the *Bootstrap* method (Press et al. 1992). Table 1 summarizes the results from the various χ^2 analyses and these results are discussed below.

Table 1. Summary of the χ^2 Analyses Data

Fit	Model Density Distribution	Fit Region	Stars	Fitted Model Parameter(s)	χ^2_ν
Ia	Power Law: $\rho \propto r^{-p}$	$r < 83''$; No "wedge"	185	$p = 2.6 \pm 0.2$	1.114
Ib	Power Law	$r < 83''$; No "wedge"	185	$p = 3.7 \pm 0.3$	1.063
IIa	Scaled Bonnor-Ebert $\rho \propto \mathcal{F}\rho_{BE}$	$r < 83''$; No "wedge"	185	$\xi_{\rm max} = 25 \pm 3$; $R_{out} = 0.15 \pm 0.014$ pc; $\mathcal{F} = 4.3 \pm 0.3$	1.117
IIIb	Cylinder (end-on)	$r < 83''$; No "wedge"	185	$H = 0.0127 \pm 0.002$ pc; $L = 0.6 \pm 0.2$ pc	1.072
IVb	Scaled Cylinder (tilted)	$r < 83''$	199	$H = 0.0164 \pm 0.002$ pc; $L\sin(\phi) = 0.14 \pm 0.02$ pc; $\mathcal{F} = (1.1 \pm 0.1)(0.5\,{\rm pc}/L)$	1.190

Note. — For each Fit, we consider only stars within $83''$ of the nominal center of L694–2, to avoid contamination from the more extended distribution of gas. For Fits Ia–IIIb, stars that occupy a wedge of angular extent 60° centered along the South-East direction have not been considered in order to eliminate the elongation of the core in this direction from affecting the fit of these azimuthally symmetric models. Fits marked "#b" include an extra screen of extinction of $H - K_s = 0.19$.

6.3.5 Spherically Symmetric Analysis

The radial variation of the E(H − K_s) colors in Figure 6.3 (South-East excluded) shows a change in behavior near 83″ or 0.1 pc (at 250 pc distance), apparently the boundary/edge of the dense core and the more extended distribution of gas. This "edge" is smaller than the extent of the core's profile in dust emission measured by Visser (2000), but is consistent considering that the emission profile is an annular average that includes emission from the South-East extension of the dense core. To separate the behavior of the core from the more extended and diffuse gas, we restrict the fitting region to $r \leq 83''$ or 0.1 pc from the nominal center of the L694–2 core, and exclude the wedge of angular size 60° that is shown in the pseudo-image of Figure 6.3 as two dashed lines. The column density distributions for the various physical models invariably produce profiles that are either flat or concave-downwards when viewed on a log-log scale. The fact that the extended distribution of gas causes the color-excess profile to be concave-upwards beyond this edge, necessitates this conservative fitting region to prevent the extended extinction from biasing the density structure fit towards shallower profiles. This fitting region contains a total of 185 stars with measurements at both H & K_s. The origin for the spherically symmetric models is left as a free parameter in the following analysis.

Ideally one would like to separate the behavior of the core from the more extended gas distribution. An obvious approach would be to try to constrain a composite model that fits for the profile of the core, plus some additional constant screen of extinction along the line of sight. This would be akin to assuming that the more extended distribution of gas forms either a uniform level of extinction that covers all lines of sight, or perhaps a

second envelope in which the L694–2 core is embedded. Unfortunately this type of model is in general difficult to constrain. The variation in colors at a given impact parameter is sufficiently large that there is too much degeneracy between the model profile and the screen extinction at the edge of the globule. Essentially, small variations in the screen level can produce very substantial (order of magnitude) variations in the inferred color excess at the outer edge of the core. In the case of the power-law models this makes it impossible to constrain a power-law index and extinction screen simultaneously. We address this problem by performing the fitting analysis for a given model with two different screens of extinction: a screen of zero (fits marked "a" in Table 1), that provides a lower limit on the steepness of a given model; and a screen of $H - K_s = 0.19$ (fits marked "b") that duplicates the mean extinction level away from the core itself (see Section 6.3.1).

The power-law model that best fits the extinction over the effective range in radius 0.03 pc$< r <$0.10 pc ($30'' < r < 83''$) has index $p = 2.6 \pm 0.2$, with $\chi^2_\nu = 1.114$ (Fit Ia). The number density normalization of the model is $n_{H_2}(0.1 \text{ pc}) = 9.0 \times 10^3$ cm^{-3} (assuming standard reddening law and gas-to-dust ratio). The outer radius of the model is not constrained; the quoted fit is for an outer radius of 0.15 pc ($125''$), but any outer radius of > 0.1 pc ($83''$) produces a statistically indistinguishable result. The offset of the central position is ΔR.A.$= -4'' \pm 2''$, ΔDec.$= 4'' \pm 2''$ (corresponds to $x = 4''$, $y = 4''$ in the pseudo image in Figure 6.3). With an additional $H - K_s = 0.19$ screen of extinction the fitted slope is much steeper, $p = 3.6 \pm 0.3$, and the number density normalization at 0.1 pc radius is reduced to $n_{H_2}(0.1 \text{ pc}) = 5.5 \times 10^3$ cm^{-3} (Fit Ib). The fit is improved ($\chi^2_\nu = 1.063$), and the offset of the central position is unchanged to within 1 σ.

For the Bonnor-Ebert models, the column density near the edge of the globule is not so sensitive to the fitting parameters as in the power law case. For these models it is possible to obtain a robust fit for an arbitrary extinction screen, but the preferred fit is for an extinction screen of zero. In fact for the screen of $H - K_s = 0.19$, the fit fails to constrain a model: a Bonnor-Ebert profile cannot be constructed that produces a steep enough slope over a large enough range in radius in the context of this physical scenario. The best fit Bonnor-Ebert model has $\xi_{\rm max} = 25 \pm 3$ (Fit IIa), scale radius $R_0 = (6.0 \pm 0.5) \times 10^{-3}$ pc ($5.0'' \pm 0.4''$), and physical outer radius $R_{\rm out} = 0.15 \pm 0.014$ pc ($125'' \pm 12''$). The center-to-edge density contrast corresponding to the fitted $\xi_{\rm max}$ is 365 ± 90, well in excess of the critical value. The reduced χ^2 for this model is $\chi^2_\nu = 1.117$, with offset central position identical to that for the power-law model. Unlike the power law models, the Bonnor-Ebert model is based on theoretical argument, and has an intrinsic density scale that is related to the physical size of the model. For the sound speed of $a = 0.20$ km s^{-1}, and distance of 250 pc, the central number density of this model is $n_{H_2}(0) = 3.1 \times 10^5$ cm^{-3}, the mass is $M = 3.0$ M$_\odot$, and the external pressure is $P_{\rm ext} = 1.5 \times 10^{-12}$ dyne cm^{-2}. Note that the density, mass, and pressure, scale with sound speed and distance as: $n_{H_2} \propto a^2/R^2$, $M \propto a^2 R$, $P_{\rm ext} \propto a^4/R^2$, respectively. In order to reproduce the normalization of the observed color-excess, the Bonnor-Ebert model must be scaled by a factor of $\mathcal{F}$ =4.30. In the context of this model, the scaling factor must be related to the terms of our adopted conversion factors by:

$$\mathcal{F} = \left(\frac{a}{0.20\,{\rm km\,s^{-1}}}\right)^2 \left(\frac{d}{250\,{\rm pc}}\right)^{-1} \left(\frac{\rm Gas/Dust}{2 \times 10^{21}\,{\rm cm^{-2}\,mag_V^{-1}}}\right)^{-1} \left(\frac{A_V/{\rm E(H-K_s)}}{16.3}\right)^{-1} \quad (6.12)$$

The actual density, mass and pressure will therefore scale differently depending on how the

factor of 4.3 is distributed amongst these scalings. We discuss possible implications of this required scaling factor later. Some subtleties involved in the fitting of Bonnor-Ebert models are discussed in the Appendix.

Figure 6.4 shows the radial dependence of the $H - K_s$ colors (as in Figure 6.3) with the best fitting profiles for the power-law (solid line) and Bonnor-Ebert (dashed line) models from Fit Ia and Fit IIa respectively. The fitting region is marked with a dotted line. The adopted origin in the plot is based on the results of Fit IIa (almost identical to that of Fit Ia). The two models are indistinguishable over the $26'' < r < 83''$ (0.03 pc$< r <$0.10 pc) range in radius where there are stars to fit, as might be expected from their almost identical values of χ^2_ν. Only at radii $r \lesssim 20''$ (0.024 pc) do the two models begin to diverge significantly, due to the fact that the profile of a Bonnor-Ebert sphere begins to flatten at roughly ~ 3 times the scale radius R_0.

The inferred power-law index of $p \geq 2.6 \pm 0.2$ is far steeper than the value of $p = 2$ for the singular isothermal sphere. The inside-out collapse model is therefore inconsistent with the envelope density structure of the L694–2 core, in addition to being inconsistent with the extended nature of the infall in this starless source. On this basis, we have refrained from fitting this model.

The steep nature of the inferred density profile agrees well with the Visser (2001) measurement of $p = 2.7$, and with the profiles of other contracting starless cores, e.g. L1544, for which the dust emission profile can be reproduced by both a massively super-critical Bonnor-Ebert sphere ($\xi_{\rm max} \sim 42$, Evans et al. 2001) or a Plummer-like model with outer power-law index $\eta = 3$ (Lee et al. 2003). The case of L1544 demonstrates that a

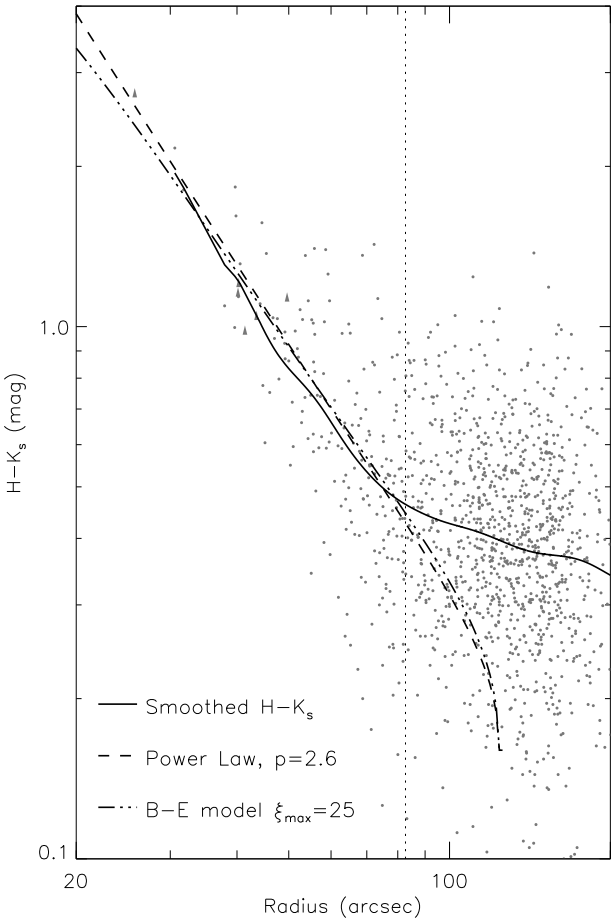

Fig. 6.4.— H − K$_s$ color against radius as in the upper-right panel of Figure 6.3. In this plot the origin is defined by the fitted position of the center, as opposed to the N_2H^+ peak used in Figure 6.3. This center adopted in this plot essentially minimizes the dispersion in the colors at a given radius. Stars that provided lower limits on H − K$_s$ that were weak have been omitted from the plot, for the sake of clarity. Overplotted are the profiles for the best-fitting power law model (Fit A, dashed line), and Bonnor-Ebert sphere (Fit B, dash-dotted line), as well as the Gaussian smoothed profile (solid line). The outer radius of the fitting region is also marked (dotted line). The two models are indistinguishable over the range in radius where there are stars to fit; only at radii $r \lesssim 20''$ (0.024 pc) do they diverge significantly.

Plummer-like model can be constructed that is essentially indistinguishable from a super-critical Bonnor-Ebert sphere. The steep structure of L694–2 inferred from our extinction data is quantitatively consistent with the Plummer-like model. But the smallest radius probed by the data is right at the turn-over radius observed in dust emission by Visser (2001), and the innermost extinction measurements show no indication of any flattening in the density profile. We are therefore unable to constrain the remaining free parameters in the Plummer-like model, $R_{\rm flat}$ and $\rho_{\rm flat}$. However, unlike the Plummer-like model, the turn-over radius for the Bonnor-Ebert sphere is intrinsically linked to the density profile in the outerregions based on the assumption of hydrostatic equilibrium. While the turn-over radius is unconstrained in the context of the Plummer-like model, it is constrained in the context of the Bonnor-Ebert model. The Bonnor-Ebert model that successfully matches the data (Fit B) has scale-radius of $R_0 = 5''$ (6×10^{-3} pc), that corresponds to the density profile turning over at around $r \simeq 15''$ (0.02 pc). This is around a factor of two smaller than the turn-over radius inferred by Visser (2001). However, this discrepancy can be explained by Visser's use of an isothermal temperature profile; more sophisticated modeling of the dust temperature distribution by Evans et al. (2001), indicates regions of relatively constant density that are systematically smaller (by factors of 0.5–0.9) than are obtained with the isothermal approximation.

6.3.6 Analyzing the Departures from Spherical Symmetry

The fact that the density profile is flat along the axis of the filament essentially allows the gas to support a steeper equilibrium density gradient in a direction perpendicular to this

axis than can be achieved by a spherically symmetric model. The steep slope of the fitted power-law model that is well in excess of $p = 2$ suggests that an isothermal cylinder might successfully reproduce the extinction data. Fitting a cylinder that is viewed end-on (line of sight parallel to the axis) provides an obvious starting point, and by introducing a tilt angle to the analysis permits an attempt to model the asymmetry observed in the L694–2 core.

The isothermal cylinder that best fits the same data sample as for the spherically symmetric model has scale height $H = 0.0127 \pm 0.002$ pc or $10.5'' \pm 2.0''$, with $\chi^2_\nu = 1.072$ (Fit IIIb). The central (on-axis) number density of the model is $n_{H_2} = 7.7 \times 10^4$ cm^{-3}, and in order to reproduce the observed normalization of the extinction data with a standard gas-to-dust ratio, distance, etc., the cylinder must have length $L = 0.6 \pm 0.2$ pc. The quality of this fit is comparable to that of the best fitting power-law model (Fit Ib) that includes the same screen of extinction. For the cylindrical model, a fit that includes no screen of extinction provides a poor description of the data ($\chi^2_\nu = 1.167$ as compared to $\chi^2_\nu = 1.114$ for a power-law model). In the context of a model with no additional screen of extinction, the profile of the cylinder can only reproduce the overall slope of the extinction data with a large value of the scale height, but this introduces a curvature to the profile that is not found in the data.

The success of the screened cylindrical model suggests an intriguing physical description of the L694–2 core. The core may represent a region of over-dense material that has condensed out of the extended filament of dense gas that is seen in the DSS image (Figure 6.1). Since the L694–2 core itself is clearly elongated along the South-East direction, the obvious

next step in the model-fitting process is to try to constrain an isothermal cylinder of length L that is tilted by an angle ϕ to the line of sight (in such a direction that its projected axis $L\sin(\phi)$ is along a South-East direction), and is embedded in a a more extended distribution of gas that produces an extra screen of extinction (i.e. as for Fit IIIb). The fitting region for this tilted model should be modified to include stars along the South-East direction, to test whether the tilted cylinder can successfully reproduce the observed asymmetry of the L694–2 core. For a dataset of all stars within $r < 0.1$ pc ($83''$) of the N_2H^+ peak, the best fitting model has scale height $H = 0.0164 \pm 0.002$ pc or $13.5'' \pm 1.5''$, with $\chi^2_\nu = 1.189$ (Fit IVb). The central (on-axis) number density is $n_{H_2} = 4.7 \times 10^4$ cm^{-3}. The top of the tilted cylinder is offset from the mm-peak by ΔR.A.$= -30'' \pm 3''$, ΔDec.$= 30'' \pm 3''$, although the top of the cylinder does not represent the peak column density of the model. The length and tilt angle of the cylinder are not constrained individually if one allows for uncertainties in the gas-to-dust ratio, distance etc. However, the projected length of the cylinder can be constrained: $L\sin(\phi) = 0.14 \pm 0.02$ pc or $117'' \pm 17''$, with the scaling given by $\mathcal{F} = (1.1 \pm 0.1)(0.5\,\mathrm{pc}/L)$. Figure 6.5 shows schematic diagrams of the 3-D geometry of this best fit tilted cylindrical model.

This model is remarkably successful at describing the extinction data from all parts of the L694–2 core. The dataset is only increased by 14 stars by the inclusion of the South-East region, and the χ^2_ν is increased by around 0.12 from the best-fitting spherically symmetric models. Yet this represents the model (on average) reproducing the high extinction of all of these 14 stars to within 1 σ in their measurement uncertainties. Moreover, if one attempts to fit a spherically symmetric model to this same dataset, the fit is drastically

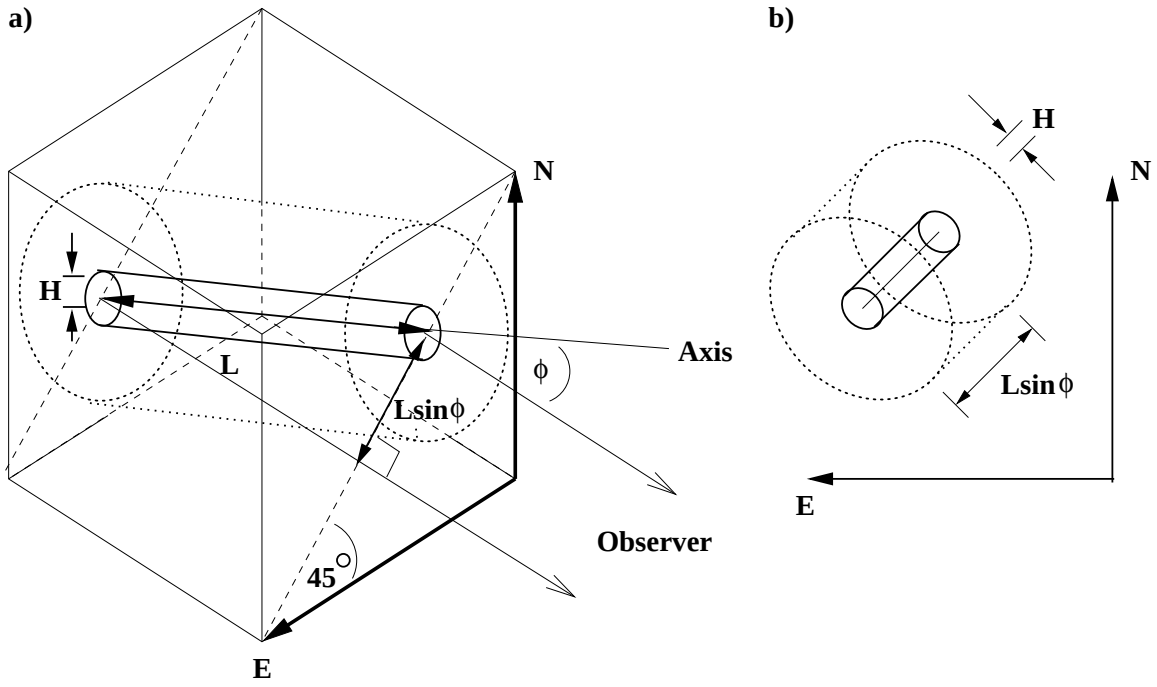

Fig. 6.5.— (a): Schematic diagram illustrating the 3-D geometry of the tilted cylindrical model of the L694–2 dense core. (b): the model as projected onto the plane of the sky. The best-fit model has scale height $H = 0.0164 \pm 0.002$ pc ($13.5'' \pm 1.5''$), and projected length $L \sin\phi = 0.14 \pm 0.02$ pc ($117'' \pm 17''$). The dotted outer contour represents where the model column density falls to the level of the extended distribution of gas in which the core is embedded, a radius of ~ 0.1 pc or $83''$. For the standard conversion factors (gas-to-dust ratio, distance, etc.), the model must be scaled by a factor of $\mathcal{F} = (1.1 \pm 0.1)(0.5 \text{ pc}/L)$ to match the observed color excess. If one allows for the uncertainties in the conversion factors (i.e. permitting $\mathcal{F} \neq 1$) then the length and tilt of the cylinder cannot be constrained individually.

worse: $\chi^2_\nu = 2.14$ for a best-fit power law model with an extinction screen. This further heightens the degree of success with which a tilted cylinder can describe both the radial and azimuthal variation of the color-excess. A pseudo-image and the radial color dependence of a best-fit tilted cylinder model with length of $L = 0.5$ pc is shown in Figure 6.6.

6.3.7 Discussion

The models that have been investigated have highly idealized geometries, and represent extreme pictures of the L694–2 core. Nevertheless, the success of these models is noteworthy, and provides a useful basis for interpreting the extinction observations, and drawing conclusions on the physical structure of the dense core. Figure 6.7 shows a plot of the molecular hydrogen number density profiles of the best fit models from Table 1. The various models have similar profiles in the region where color-excess measurements can be obtained ($r \geq 30''$, 0.035 pc or 7500 AU). In the inner regions the profiles differ significantly; future observations of L694–2 in dust emission made with interferometers may therefore distinguish between the various interpretations of density structure.

The Bonnor-Ebert model is a hydrostatic equilibrium structure, so a fitted value of $\xi_{\rm max} = 25$ that is so far in excess of the critically stable value presents an obvious problem with a Bonnor-Ebert description of L694–2. The analysis does indicate that the distribution of material in L694–2 is very unstable to gravitational collapse, a conclusion that is consistent with the strong infall signatures observed in molecular spectral lines. Including an additional screen of extinction, as might be expected since the L694–2 core is clearly embedded in a more extended distribution of gas, causes the fit for a Bonnor-Ebert model

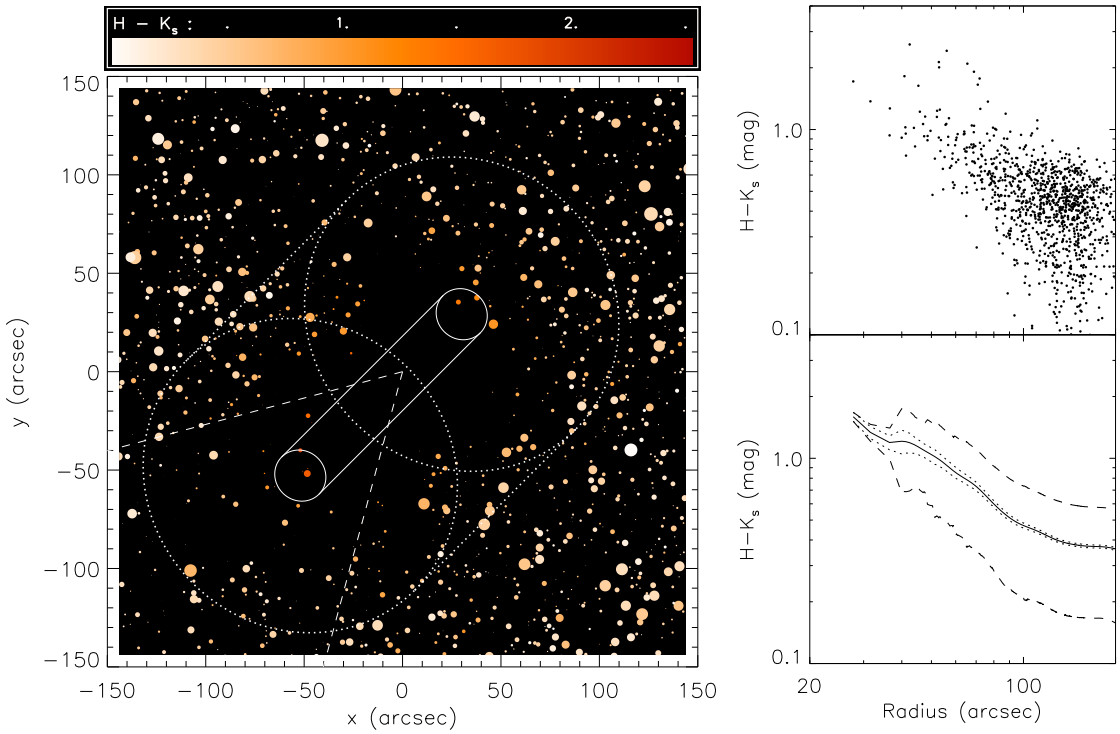

Fig. 6.6.— Left: Pseudo image of a best-fitting tilted cylindrical model (see text for description). The schematic diagram of the model from Figure 5b is superposed on the plot. Upper right: $H-K_s$ color against radius out to 200″ (0.24 pc). Stars within the dashed region in the pseudoimage are omitted from the plot. Lower right: smoothed $H-K_s$ color against radius out to 200″ from the nominal center of L694–2 (solid line), with ± one standard deviation (dashed line) and ± one standard error (dotted line). The success of the model can be seen by comparison with the actual color excess data in Figure 6.3. Note that the dispersion in the $H-K_s$ colors at a given radius is due to a combination of the variation of the intrinsic colors of the background stars, and the departures from spherical symmetry of this model. At large radii, the former effect dominates, while at small and medium radii, the latter effect is more important.

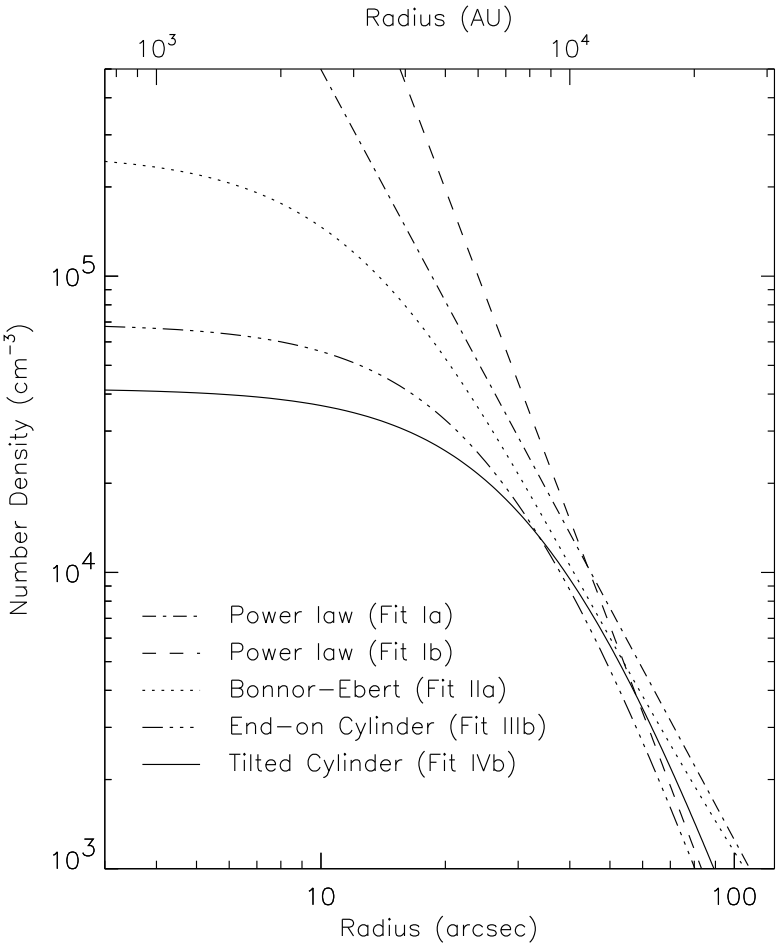

Fig. 6.7.— Number density of molecular hydrogen vs. radius for the various best fit models of L694–2 from Table 1, assuming a mean molecular weight of $\mu = 2.29$, and a hydrogen mass fraction $X_{\rm H} = 0.73$. The two power-law models (*dash-dot* and *dashed*) have been normalized to the same column density as the Bonnor-Ebert model (*dotted*). For the Bonnor-Ebert model and the two Cylindrical models (*dash-dot-dot-dot* and *solid*), the normalization is predicted directly from the fitted profile shape. Assuming the standard gas-to-dust ratio, reddening law, distance, etc. the Bonnor-Ebert model must be scaled by a factor of $\mathcal{F} = 4.3$ to match the observed color excess. In the context cylindrical models this scaling can be interpreted in terms of the extension of the cylinder along the line of sight. The extinction measurements cannot penetrate the region $r \leq 30''$ (7500 AU) where the various density profiles diverge from each other. The structure in this region can be probed with interferometer observations of dust emission.

to fail. Essentially this model is unable to reproduce the steep slope of the inferred density profile if any additional extinction is present.

The Bonnor-Ebert model provides a description of the dynamical state of the core that is absent from the simple power law models. Unfortunately, the normalization of these models differs substantially from what is observed in the L694–2 core ($\mathcal{F} = 4.3$). Remarkably, the difference in the normalization between observation and theory is quite similar to that found in the study of B335, a core that is likely associated with the same parent molecular cloud as L694–2 ($\mathcal{F} = 5.2$ for an inside-out collapse model, $\mathcal{F} = 3.3$ for a Bonnor-Ebert sphere).

The origin of this required scaling presented a difficult problem in the B335 study, since it is hard to attribute such a large discrepancy to any one stage in the conversion from density to color-excess. However, the present study suggests an intriguing explanation for the surprisingly high extinctions observed in these cores, namely that the discrepancy is simply a result of the cores having larger masses than predicted by the spherically symmetric theory, perhaps with B335 representing simply a later stage to which the L694–2 core will eventually evolve. The L694–2 core has formed out of a filament of dense gas, and our modeling suggests that it has prolate structure, with the major axis lying close enough to the line-of-sight that much of the mass is missed by analysis that assumes a symmetry between the profile of the core in the plane of the sky, and the profile of the core along the line-of-sight. The infalling motions inferred from molecular spectral lines by Lee et al. (2001) represent motions along the line of sight. If the motions arise in the core and not the surrounding envelope of material, then the strength and orientation of these motions is

consistent with our hypothesis, since a prolate core is most unstable to collapse along its major axis.

The relation of the L694–2 dense core to the associated lower-density filament seen in the DSS image is interesting: the core appears to be elongated along the line of sight, while the filament appears to be elongated in the plane of the sky. A simple explanation for the origin of such this system is as follows. Suppose a low-density filamentary cloud is extended in the plane of the sky. The cloud has some angular momentum and is very slowly rotating about an axis perpendicular to its long direction. A small elongated region of the cloud condenses while conserving its angular momentum, therefore turning faster than the rest of the cloud. The result is a short dense filament whose major axis is rotated with respect to the long axis of its lower-density parent filament, which has become "kinked". In the L694–2 case, the short dense segment seems to lie mostly along the line of sight.

Theoretical argument and numerical simulation both suggest that an un-magnetized filament will be unstable to fragmentation if its length exceeds about four times its half-mass radius. The half-mass radius for the fitted tilted cylindrical model of the L694–2 core is 0.05 pc ($40''$), which suggests a maximum stable length of only about 0.2 pc. This means that for the standard conversion factors, the length of the fitted cylinder is such that it should fragment into two or more pieces at some stage in the future (or possibly should have already done so), unless some source of support such as a magnetic field acts to prevent this process. If fragmentation of the L694–2 core does not occur, then future evolution should produce a more spherically symmetric core, with a mass that is larger than would have otherwise been expected. Subsequent collapse of this core might resemble that

observed in B335.

This hypothesis requires a special orientation of the magnetic field in the L694–2 and B335 cores, both to support the cores, but also to prevent the support from affecting the observed molecular line widths. Although this may seem contrived, the orientation of B335 is well known to be special, with the outflow lying within 10° of the plane of the sky (Hirano et al. 1988). Similarly, our modeling of the color excess near L694–2 suggests a prolate core oriented close to the line-of-sight (20° for $L = 0.4$ pc). Observations of optical and infrared polarization of stars that are embedded in, or background to filamentary molecular clouds show that the direction of the magnetic field is often related to the direction of the axis of the filament; in some cases the two are parallel (e.g. Ophiuchus, Goodman et al. 1990), while in others the two are perpendicular (e.g. Taurus, Heyer et al. 1987). Both cases can be explained by recent modeling of the production of gas filaments by the fragmentation of magnetized sheets (Nagai et al. 1998). In these models, the magnetic field delays the growth of perturbations along a particular direction, causing the production of filamentary structures. The field provides support to the filament, and increases the critical (fragmentation) length of the filament from the un-magnetized case. If the field in L694–2 is oriented in the plane-of-the-sky, perpendicular to the major axis of the core, then the support provided along the major-axis would be maximized. Since the turbulent velocity in L694–2 is low ($a_{\rm turb} \simeq 0.09$ km s^{-1} compared to the thermal speed of $a_{\rm therm} \simeq 0.18$ km s^{-1}), Alfven waves should not be strongly driven, and not add appreciably to measured line-widths. Such a field configuration might therefore inhibit fragmentation but remain essentially undetectable in observations of molecular spectral lines.

To affect the fragmentation scale of L694–2, the field strength would need to be such that the magnetic pressure ($P_M = B^2/8\pi$) is greater than or comparable to the gas pressure at the axis of the filament ($P_g = \rho_0 a^2$). For the standard conversion factors, this suggests:

$$B \gtrsim \text{few} \times 10\ \mu\text{G} \tag{6.13}$$

Such a minimum field strength is large by typical standards of the Interstellar Medium. For instance, Crutcher & Trowland (2000) measured a line of sight magnetic field of $B \sim 11\ \mu$G in starless core L1544 using the Zeeman effect in lines of OH, although any non-zero inclination angle will result in the true field being stronger. Although the L1544 field is already much higher than the typical upper limits found for other dark clouds (Crutcher et al. 1993), a field of this required strength in the L694–2 core is certainly conceivable. Moreover, if any of the required scaling can be attributed to systematic error in the conversion factors, then the minimum field strength will be lowered. For instance, a gas-to-dust ratio in the L694–2/B335 region that is half the "standard" value in the ISM (a variation that is typical in the ISM), then the inferred length of the tilted cylinder (Fit IVb) will be reduced by roughly the same factor of two, and the cylinder would be marginally stable to fragmentation even in the absence of a magnetic field.

6.4 Summary

We present a near-infrared extinction study of the contracting starless core L694–2 using observations made with the ESO NTT. In summary:

1. The $5' \times 5'$ image of L694–2 shows a dramatic fall off in the number of stars detected

toward the location of peak millimeter-wave (N^2H^+) emission, where the extinction increases because of the central concentration of dense core material. The image contains a total of 1451 stars detected in both H & K_s bands, with 199 with impact parameters within 83″ (0.1 pc), the innermost of which is at 28″ (0.034 pc) from the nominal peak. The photometry shows a steep gradient in the $H - K_s$ colors towards the center. The radial profile of the color excess demonstrates a change in behavior at a radius of around 83″: the profile flattens, apparently associated with the boundary/edge of the dense core and a more extended distribution of gas in which the core is embedded. In addition the core exhibits departures from spherically symmetry, with the regions of highest color excess extending to the South-East, and somewhat towards the North, following the shape of L694–2 visible at low extinction levels in the DSS image. These asymmetries are apparently connected to the filamentary structure of the extended gas in the region.

2. We compare a series of models of dense core structure to the extinction data, including spherically symmetric power-laws, and Bonnor-Ebert spheres. Based on the radial profile of the color excess, only stars within 83″ (0.1 pc) of the peak are included in the fit to prevent the extended extinction from biasing the fitting results towards models with shallower slopes. In addition, for the spherically symmetric analysis, we exclude stars that fall within a small wedge to the South-East (60° wide), to avoid biasing the fits with the extinction component that extends in this direction. It is not possible to fully separate the contribution to the color excess from the core from that due to additional extended material. We therefore perform two fits for each type of model,

one assuming extinction only from a model core, and the second assuming extinction from a core embedded in a screen of thickness $H - K_s = 0.19$, chosen to reproduce the colors of stars at the edge of the image where the color excess is smallest (i.e. $> 2'.5$ from the center). The best fit single power law model has index $p = 2.6 \pm 0.2$ ($1\ \sigma$), steeper than the value of $p = 2$ for an isothermal sphere. An unobscured Bonnor-Ebert sphere provides an indistinguishable fit to the data; the dimensionless outer radius is $\xi_{\rm max} = 25 \pm 3$. Including an additional uniform extinction component increases the steepness of the inferred core profiles. The best fit power law index increases to $p = 3.7 \pm 0.3$, while a Bonnor-Ebert model cannot be constructed that produces a steep enough slope over a large enough range in radius. The unobscured Bonnor-Ebert model must be scaled by a factor $\mathcal{F} = 4.3$ to match the observed color excess. Remarkably, this difference in normalization between observation and theory is similar to that found in the extinction study of B335, which is likely associated with the same molecular cloud.

3. The inferred power law index p suggests a cylindrical model for the density distribution, which can support a large density gradient perpendicular to its cylindrical axis. An embedded cylinder viewed along the axis with scale height $H = 0.0127 \pm 0.002$ pc ($10.5'' \pm 2.0''$) provides an equally good fit as a spherical power law model. A tilted cylinder can also reproduce the asymmetry of the L694–2 core, matching the color excess of stars in the South-East wedge to within $1\ \sigma$ on average. This tilted cylinder has projected length $L \sin\phi = 0.14 \pm 0.02$ pc ($117 \pm 17''$), with scale height $H = 0.0164 \pm 0.002$ pc ($13.5'' \pm 1.5''$). For standard values of the conversion factors,

the model must be scaled by a factor of $\mathcal{F} = (1.1 \pm 0.1)(0.5 \text{ pc}/L)$ to match the observed color excess.

4. The cylindrical model provides an intriguing explanation for the surprisingly high extinctions observed in the L694–2 core, and perhaps also the B335 core: the discrepancy may result from larger masses than indicated by spherically symmetric theory, perhaps with B335 representing a later stage to which the L694–2 core will eventually evolve. The large scale view suggests that L694–2 has formed out of an extended filament of dense gas, and our modeling suggests a prolate structure, with the major axis lying close enough to the line-of-sight that much of the mass is missed by assuming symmetry between the profile of the core in the plane of the sky, and the profile of the core along the line-of-sight. The inward motions in L694–2 inferred from molecular spectral lines, which represent motions along the line of sight, might reflect the fact that a prolate core is most unstable to collapse along the major axis. If the cylinder is magnetized, with static field $B_0 \gtrsim$ few $\times$ 10 μG in the plane of the sky, then fragmentation of this cylinder could be prevented. The low turbulent velocity measured in L694–2 should prevent Alfven waves from contributing to the observed widths of molecular spectral lines, and the support would remain essentially undetectable. Moreover, if the gas-to-dust ratio in this region is lower than the "standard" value, then fragmentation might be avoided at a lower field strength.

5. Future observations of dust in emission made with interferometers will measure the innermost structure of the L694–2 core that can not be probed by dust extinction. In particular, the dust emission structure will provide further tests of the cylindrical

model hypothesis.

Acknowledgements

DWAH is indebted to Tracy Huard for his help during the data reduction stages. We also thank Lee Hartmann for useful suggestions regarding departures from spherical symmetry. This publication makes use of data products from the Two Micron All Sky Survey, which is a joint project of the University of Massachusetts and the Infrared Processing and Analysis Center/California Institute of Technology, funded by the National Aeronautics and Space Administration and the National Science Foundation. CJL acknowledges support from the NASA Origins program, Grant NAG-5-9520.

Appendix 6.A

Subtleties in Fitting Bonnor-Ebert Models

It is interesting that both the scale-radius and outer-radius for the fitted L694–2 Bonnor-Ebert model (Fit IIa) are better constrained than the dimensionless radius of the sphere, when the three parameters are intrinsically linked by the relation: $R_{\rm out} = \xi_{\rm max} R_0$. The Bonnor-Ebert solution is a dimensionless curve that extends from the origin to a cutoff at the dimensionless outer radius $\xi_{\rm max}$. Scale is added by including a physical size for the curve (either the scale radius or the outer radius). A given density profile over a fixed range in radius can therefore be reproduced by a model with a larger physical size and a larger $\xi_{\rm max}$,

thereby assuring that we are still looking at the same region of the dimensionless curve. Such a model will have the same value of the scale-radius R_0.

In the model fitting procedure, what is actually observed is the integrated profile of the globule, and this is altered slightly due to the contribution from the extra material at the edge of the globule, which produces a more shallow profile. However, except for right at the edge of the globule, the effect of the extra material on the shape of the profile can be offset by reducing slightly the scale-radius of the model (or increasing $\xi_{\rm max}$ a little more), which raises the degree of central concentration and steepens the profile a little. It is the change to the profile near to the outer radius from this extra material that allows the outer radius and $\xi_{\rm max}$ to be constrained by measurements of an extinction profile.

To summarize, despite the fact that the family of Bonnor-Ebert spheres are characterized by the parameter $\xi_{\rm max}$, it is the parameter R_0, the scale-radius, that is the more robust result of a fit to an observed profile. The outer radius of a globule has some inherent and non-zero uncertainty, due to possible confusion with extended structure, nearby sources or interaction with the ambient medium or interstellar radiation field (ISRF). The effect is that the physical curvature is inevitably better defined than the dimensionless curvature, since the latter suffers the additional contribution from the uncertainty in the radius (in order to make the observed profile dimensionless, the radii must be divided by the outer radius).

When Bonnor-Ebert models were fitted to B68 (Alves et al. 2001) and B335 (Harvey et al. 2001), fixed outer radii were assumed. The uncertainty in the assumed outer radii were not included in the final assessment of the fitted profiles, which will lead to underestimated

errors in $\xi_{\rm max}$. The systematic uncertainty in the assumed radius will also lead to systematic uncertainties in $\xi_{\rm max}$, which were not accounted for in these studies. In both studies the radial variation of the H − K colors shows that the adopted outer radii represent essentially lower limits to the true outer edge of the globule, in the B68 case because the edge is assumed to occur at a visual extinction of $A_V = 1$, and in the B335 case because the edge is chosen to coincide with a low-power contour of molecular gas emission. Allowing the radius of the globule to vary as an additional parameter will therefore lead to a larger fitted value of $\xi_{\rm max}$, even for a small increase in the outer radius. The uncertainty in $\xi_{\rm max}$ will also increase. In the case of B335, the quoted $\xi_{\rm max}$ is so large (and already uncertain at a level that is similar to the uncertainty in the outer radius) that realistic changes in the outer radius cannot lead to a qualitative change in the picture — the fitted $\xi_{\rm max}$ will increase even further from the stable value, and although the fitted R_0 may decrease somewhat, the model would remain heavily resolved by the IRAM PdBI, and therefore be unable to reproduce the observed mm-wave dust emission (Harvey et al. 2003a).

For B68 however, the conclusions are less clear. The quoted value of $\xi_{\rm max} = 6.9 \pm 0.2$ leads to the interpretation that the globule is almost perfectly perched at the threshold for stability. A small change in the inferred $\xi_{\rm max}$ might alter this conclusion. We therefore apply our more detailed model-fitting procedure to the Alves et al. (2001) extinction data. Unlike the L694-2 data, the B68 data are azimuthally averaged in bins of width $3''$ centered on the position of peak column density. The small column density of the B68 globule essentially allows the profile to be measured at all radii, from $10''$ out to $130''$ where no extinction can be discerned.

A fit to the data within a conservatively chosen region $r \leq 100''$, with outer radius and $\xi_{\rm max}$ as free parameters returns essentially the Alves et al. result: $\xi_{\rm max} = 6.9 \pm 0.2$, $R_{\rm out} = 106'' \pm 1''$, with $\chi^2_\nu = 1.43$. However, with a different fitting region, the inferred model parameters are slightly changed. The value of χ^2_ν provides a useful tool to select the appropriate fitting region. As the region is extended from $100''$ towards the edge of the globule, the minimum in χ^2_ν remains fairly constant initially, but then jumps to 2.1 for $r \leq 109''$, and continues to increase, reaching a value of almost 5 for a fitting region of $r \leq 130''$ — the largest radius at which any extinction was measurable. This behavior is caused by the profile beginning to depart from the Bonnor-Ebert profile at the edge of the globule, perhaps due to interaction with the ISRF. We therefore suggest a fitting region of $r < 109''$ is most appropriate (included data point at largest radius is at $r = 106''$). In particular this choice happens to coincide with the inferred outer radius of the Bonnor-Ebert model, as well as the radius where the visual extinction reaches unity. The best fit model parameters for this region are $\xi_{\rm max} = 7.2 \pm 0.2$, $R_{\rm out} = 108 \pm 1''$, with $\chi^2_\nu = 1.55$. The increase in the minimum χ^2_ν in moving to this larger fitting region is justifiable, since it is equivalent to that for a model where the parameters differ by only $1/2\ \sigma$ from their optimal values. That the Bonnor-Ebert model is so tightly constrained results from the well defined edge to the B68 globule, in stark contrast to the extended structure associated with L694–2. However, the best-fit model with $\xi_{\rm max} = 7.2 \pm 0.2$ represents a slightly more unstable configuration than the value calculated by Alves et al. (2001).

The physical properties of this model differ at most only slightly from those of the Alves et al. model. The inferred mass of the globule is $M = 2.2\ {\rm M}_\odot$ for a distance of 125 pc,

and the standard gas-to-dust ratio. The inferred central number density is increased by roughly 2.5%, but to the level of precision in the factors required for the conversion it is essentially unchanged $n_{H_2} = 4.0 \times 10^5$ cm^{-3}. The external pressure is 6% smaller, $P_{ext} = 2.3 \times 10^{-11}$ dyne cm^{-2}, for a kinetic temperature of 16 K. Hotzel, Harjo & Juvela (2002) have proposed a smaller distance to B68 of 85 pc and a lower kinetic temperature of 10 ± 1.5 K. These changes lead to a smaller inferred mass of the globule, $M = 1.5$ M$_\odot$, a higher central number density $n_{H_2} \simeq 5.4 \times 10^5$ cm^{-3}, and a smaller external pressure $P_{ext} = 2.0 \times 10^{-11}$ dyne cm^{-2}.

Chapter 7

Inner Structure of Starless Core L694-2 Derived from Millimeter-Wave Interferometry[1]

Daniel W.A. Harvey, David J. Wilner, Philip C. Myers, & Mario Tafalla 2003d, *The Astrophysical Journal*, in press, astro-ph/0307106

---

[1]Based on observations carried out with the IRAM Plateau de Bure Interferometer and the Berkeley Illinois Maryland Array. IRAM is supported by INSU/CNRS (France), MPG (Germany) and IGN (Spain). The BIMA array is operated by the Berkeley-Illinois-Maryland Association under funding from the National Science Foundation.

Abstract

We study the density structure of the candidate contracting starless core L694–2 using 1.3 mm dust continuum observations from the IRAM Plateau de Bure Interferometer and the Berkeley-Illinois-Maryland Array, which probe spatial scales from 10000 AU to 500 AU. The long baseline PdBI observations detect no emission from the core, and limit the maximum contamination from a compact component: $F_c < 2.7$ mJy. The flux limit corresponds to a very small disk mass, $M_{\rm disk} \lesssim 5 \times 10^{-4}$ $M_\odot$ (60 K/$T_{\rm disk}$), and bolsters the "starless" interpretation of the L694–2 core. The shorter baseline BIMA data are compared to a series of density models using a physically motivated temperature distribution with a central minimum. This analysis provides clear evidence for a turn-over from the steep density profile observed in the outer regions in dust extinction to substantially more shallow behavior in the inner regions (< 7500 AU). The best fit Bonnor-Ebert, Plummer-like, broken power law, and end-on cylinder models produce very similar flattened profiles and cannot be distinguished. We quantify the sensitivity of the inferred structure to various uncertainties, including the temperature distribution, the accuracy of the central position, and the presence of a weak unresolved central component. The largest uncertainty comes from the temperature assumption; an isothermal model modifies the best fit parameters by $\sim 2\,\sigma$, with the inferred density profiles more shallow. Dust emission and extinction profiles are reproduced by an embedded cylinder with scale height $H = 13.5''$ inclined at a small angle to the line of sight. The turn-over observed in the L694–2 density distribution suggests that pressure forces still support the core, and that it has not fully relaxed as in the inside-out collapse model, despite the extended inward motions inferred from molecular line observa-

tions by Lee, Myers, & Tafalla. In the context of the cylindrical density model, these inward motions may represent the contraction of a prolate core along its major axis.

7.1 Introduction

The observed properties of dense cores (e.g. Benson & Myers 1989) form the basis of the standard model of isolated star formation. In this model, the "starless" dense core represents the earliest identifiable stage of the star formation process. The physical conditions in this early stage have a profound effect on the evolution of protostars towards the main sequence. The initial density structure, particularly in the innermost regions, affects the collapse dynamics and the time dependence of the mass accretion rate and therefore many of the observable properties of protostars, including luminosity.

A quantitative understanding of the collapse dynamics has been hindered by uncertain knowledge of appropriate initial conditions (André, Ward-Thompson & Barsony 2000). In the popular theory of "inside-out" collapse, a spherical starless core loses turbulent and magnetic support and relaxes to a balance between gravity and thermal pressure, an r^{-2} density distribution is established and the core collapses from the inside-out with a constant mass accretion rate (Shu 1977). However, if collapse begins before the density distribution fully relaxes, then a central region of relatively constant density remains and the mass accretion rate is an order of magnitude larger at early times (Foster & Chevalier 1993). This phenomenon has been identified with the youngest "Class 0" protostars, which exhibit especially powerful outflows (Henriksen, Andre & Bontemps 1997; Andre, Ward-Thompson

& Barsony 2000). Better observations of starless cores are needed to determine the initial conditions.

The L694–2 dense core is one of several "strong" infall candidates among starless cores, based on observations of molecular line profiles with redshifted self-absorption in a systematic search of more than 200 targets (Lee, Myers & Tafalla 1999). Molecular line maps of these objects provide strong evidence of inward motions, with speed ~ 0.1 km s^{-1} over a radius of ~ 0.1 pc (Lee, Myers & Tafalla 2001). The physical basis for these motions is unclear. The speeds are subsonic and may be associated with condensation through ambipolar diffusion, or perhaps a magnetically diluted gravitational collapse (Ciolek & Basu 2000). Alternatively, pressure driven motions due to the dissipation of turbulence may be responsible (Myers & Lazarian 1998).

Observations of dust column density provide a means to infer the structure and dynamical state of a dense core. Harvey et al. (2003b) describe near-infrared extinction measurements toward L694–2 that show a very steep density profile in the region $r = 30''$ to $83''$ (0.036 to 0.1 pc, or 7500 to 20000 AU), where background stars were detectable for extinction measurements. The extinction data can be fit by a number of models that produce nearly degenerate column density profiles, including a simple power law with index $p = 2.6 \pm 0.2$, a supercritical Bonnor-Ebert (B-E) sphere with dimensionless outer radius $\xi_{\rm max} = 25 \pm 3$, or a nearly end-on isothermal cylinder with scale height $H = 13.5'' \pm 1.5''$. The latter two models provide a physical description of the core that represents an unstable configuration of material that is consistent with the infalling motions inferred from molecular spectral line profiles. In particular, the slightly tilted cylindrical model that provides

a basis for interpreting the asymmetry of the L694–2 core should be highly unstable to gravitational collapse along its axis (close to the line of sight), consistent with the strength and orientation of the observed velocity structure. The model also provides a framework for understanding the very high extinctions observed in L694–2, namely that the core has prolate structure with the full extent (mass) of the core being missed by analysis that assumes symmetry between the profile of the core in the plane of the sky, and the profile of the core along the line-of-sight.

Observations of long wavelength dust emission provide another means of probing density structure. This technique is almost as direct as observations of dust extinction. The intensity of the optically thin emission provides an integral along the line-of-sight of the product of the density, temperature, and opacity of the dust. The analysis of dust emission complements dust extinction work because the dust emission method becomes most effective in the high column density inner regions of dense cores where dust extinction becomes large and difficult to penetrate.

Much of the detailed information on starless core structure comes from observations of dust emission, using data from bolometer cameras (e.g. Ward-Thompson, Motte & Andre 1999, Shirley et al. 2000, Visser, Richer & Chandler 2001). An important conclusion from these studies is that starless cores appear to show flat density profiles in their inner regions, with extended envelopes that fall off rapidly in power law fashion. Recently, the predominance of the flat central density gradients has been called into question as more sophisticated analysis including self-consistent temperature calculations indicate much smaller regions of flattening, or no flattening at all, in large part because the cores are cooler in their deep

interiors than assumed previously (Evans et al. 2001, Zucconi et al. 2001). In addition, the central regions of even the nearest protostellar cores are generally comparable in size to the beamwidths of these telescopes and are poorly resolved. The density structure at smaller scales can be probed with interferometers. Strong constraints can be derived by analyzing interferometer data from dense cores directly in the visibility domain, though this approach has been rarely used (Keene & Masson 1990, Hogerheijde et al. 1999, Harvey et al. 2003a, Looney, Mundy & Welch 2003).

L694–2 has been mapped at 850 μm with SCUBA on the JCMT by Visser (2000) and at 1.2 mm with the IRAM 30m telescope by Tafalla et al. (2003). The two maps have similar resolutions, 14" for SCUBA and 11" for IRAM. The dust emission profiles suggest a steep outer density gradient ($p \simeq 2.7$ from SCUBA, $p = 2.5$ from IRAM) consistent with that inferred from dust extinction (Harvey et al. 2003b). The usual isothermal analysis suggest a flattening of the density gradient within a radius of a few thousand AU. Visser (2000) fits a broken power law model that suggests an inner power law index of $p = 0.8$ within a break radius of 8000 AU ($\sim 30''$). Although no radio point source has been detected in the L694–2 core (e.g. Harvey et al. 2002), the measurement of the inner power law index suffers a potentially large systematic error from possible point-source contamination to the central beam (Shirley et al. 2002). In this paper, we present observations of dust continuum emission from L694–2 at 1.3 mm obtained with the IRAM Plateau de Bure Interferometer (PdBI) and the Berkeley-Illinois-Maryland-Array (BIMA). The long baseline observations from the PdBI limit the contribution to the flux from any embedded point source, while the BIMA observations sample the dense core structure on size scales from $\sim$ 10000 AU to

$\sim$ 1500 AU (resolution to 6″). Together, these observations provide conclusive evidence of a flattening in the density profile within $\sim$ 30″ from the center of the core.

7.2 Observations

7.2.1 IRAM PdBI

Continuum emission from L694–2 was observed at 1.3 mm (231.32 GHz) with the IRAM PdBI in the compact D configuration on 2001 November 20 (4 antennas) and 2002 April 03 (6 antennas). Table 7.1 lists the observational parameters. A single pointing was used, with center 19:41:04.44, 10:57:00.9 (J2000) chosen to coincide with the position of peak emission in the N_2H^+(1–0) spectral line measured at BIMA (Jonathan Williams 2003, private communication). The half-power field of view for PdBI at this wavelength is 22″ (5500 AU). The PdBI observations provide measurements at baseline lengths from the shadowing limit of 15 m to a maximum of over 100 m (resolution $\sim$ 2.″6). The absolute flux scale was set by observations of the standard source MWC 349, assumed to be 1.71 Jy. The estimated uncertainty in the flux scale is roughly 20%. Frequent observations of nearby calibrators J1751+096 and J1925+211 were used to determine time-dependent complex gains. Continuum visibility records were formed for each 60 s integration of the digital correlator (3×160 MHz bandwidth, tuning double sideband). The correlator bandpass was measured with observations of the strong sources 3C 345 (2001 November 20) and 3C 273 (2002 April 03). The data were calibrated using the IRAM software package *CLIC*, and comprise a total of 7240 records (2040 records from 2001 November 20, 5200 from 2002 April 03). In

Table 7.1. Summary of instrumental parameters

Parameter	PdBI Value	BIMA Value
Observation dates	2001 Nov. 20;	2001 Sep. 22; Sep. 29;
	2002 Apr. 03	2002 Mar. 31 Jun. 08; Sep. 09
Configuration (antennas)	D (4); D (6)	D; D; C; D; D (9)
Pointing center (J2000)	$19^h41^m04\overset{s}{.}44$, $+10°57'00\overset{''}{.}9$	$19^h41^m04\overset{s}{.}32$, $+10°57'06\overset{''}{.}1$
Observing frequency	231.3 GHz	231.3 GHz
Phase calibrators	J1751+096, J1925+211	J1925+211
Bandpass calibrator	3C 345; 3C 273	Uranus
Flux calibrator	MWC 349	Uranus
Primary beam FWHM	$22''$	$50''$
Bandwidth	480 MHz	700 MHz
RMS	0.9 mJy	1.6 mJy

addition to amplitude and phase, each record contains a variance measure, determined from the system temperature and antenna gains.

7.2.2 BIMA

Continuum emission from L694–2 was observed at 1.3 mm (231.32 GHz) with BIMA in the compact D configuration on 2001 September 22 and 29, 2002 June 08, and 2002 September 09, and in the more extended C configuration on 2002 March 31. Table 7.1 lists the observational parameters. A single pointing of the nine antennas was used on each occasion.

The pointing center for the BIMA observations is displaced from the PdBI pointing, by δR.A.$= -1\farcs8$, δDec.$= 5\farcs2$. The half-power field of view for the BIMA antennas is $50''$ (12,500 AU). The BIMA observations provide measurements at baseline lengths from the shadowing limit of 6 m to a maximum of 70 m (resolution $\sim 3\farcs7$). The bandpass and flux calibration were determined through observations of Uranus, using the a priori antenna gains. The estimated uncertainty in the flux scale is roughly 15%. Frequent observations of J1925+211 were used to determine time-dependent complex gains. Continuum visibility records were formed for each 23 s integration of the digital correlator (700 MHz bandwidth). The data were calibrated in the BIMA software package *MIRIAD*. The resulting $\sim 2 \times 10^5$ records were then averaged in time bins of 3.45 minutes (9 records). This choice of binning was made to reduce the number of visibilities to a more manageable size for analysis, without introducing significant phase error at the longer baselines. The resulting dataset contains 22327 records. As with the PdBI dataset, a variance measure for each visibility measurement is also recorded.

7.3 Constructing Model Visibilities

The visibility measurements are analyzed directly, without producing images that are limited by standard Fourier inversion and deconvolution techniques. This approach is computationally intensive, but it allows a much more direct comparison with models than analyzing images. In particular, the results are not compromised by problems with the synthesized beam characteristics and dynamic range.

The L694–2 visibilities are compared to theoretical models of protostellar envelope structure by constructing synthetic visibilities, taking account of (1) the dust continuum radiative transfer, and (2) the specifics of the observations, including the exact (u, v) sampling and primary beam pointing and attenuation for the two telescopes. The models necessarily include an assumed temperature distribution and (constant) specific mass opacity in addition to the model density field. We do not consider an exhaustive list of starless core models but instead fix attention on a few widely promoted density fields, including B-E spheres, Plummer-like models, broken power law descriptions, and isothermal cylinders. These models can all match the steep density gradient inferred for the outer regions of the core.

The model datasets are constructed using the recipe described in Harvey et al. (2003a). In brief, a 512×512 model intensity image of resolution $0\farcs5$ pixel^{-1} is calculated using the full Planck function for the emissivity and integrating the radiative transfer equation through the model globule. Each model is normalized to a flux at 1.2 mm of 800 ± 80 mJy within a circular aperture (top-hat) of radius $30''$, calculated from the continuum map of L694–2 made by Tafalla et al. (2003) with MAMBO on the IRAM 30m telescope (assuming a dust opacity spectral index of unity). We adopt an outer boundary of $R_{\rm out} = 0.15$ pc in the models based on the extinction observations (Harvey et al. 2003b), although the results are not sensitive to this assumption. Observations are simulated by performing an FFT, and assuming a Gaussian form for the primary beams (PdBI FWHM $22''$, BIMA FWHM $50''$). The exact (u, v) sampling is achieved by interpolating the real and imaginary parts of the resulting visibility grid. The center for each model is assumed to be at the pointing center

of the PdBI observations, and in Section 7.5.2 we discuss the slight sensitivity of the results to this assumption.

7.3.1 Model Selections

As detailed above, the model visibilities are derived from the assumed (1) mass density distribution $\rho(r)$, (2) dust temperature distribution $T_d(r)$, and (3) specific mass opacity of the dust $\kappa_{1.3\ \mathrm{mm}}$ (normalized to a constant flux within a 30″ circular aperture). We consider the expected form of these quantities, and their uncertainties.

Density

The main goal is to constrain the density distribution of L694–2, given a realistic choice for the temperature distribution and specific mass opacity. We consider four models of starless core density structure that can match the steep density gradient in the outer regions inferred from the near-infrared extinction.

Bonnor-Ebert spheres.— These models are pressure-confined isothermal spheres, for which the solution remains finite at the origin (Ebert 1955, Bonnor 1956). They are solutions of a modified Lane-Emden equation (Chandrasekhar 1967):

$$\frac{1}{\xi^2}\frac{d}{d\xi}\left(\xi^2\frac{d\psi}{d\xi}\right) = \exp\left(-\psi\right) \ , \tag{7.1}$$

where $\xi = (r/R_0)$ is the dimensionless-radius, $R_0 = a/\sqrt{4\pi G\rho_c}$ is the (physical) scale-radius, and $\psi(\xi) = -\ln\left(\rho/\rho_c\right)$ is a logarithmic density contrast, with ρ_c the (finite) central density, and a is the effective sound speed in the core (we adopt $a = 0.20$ km s^{-1} based on an

assumed central temperature of 9 K, with turbulent component $a_{\rm turb} = 0.09$ km s^{-1}, as in the extinction study). Configurations with $\xi_{\rm max} > 6.5$ are unstable to gravitational collapse. A highly supercritical dimensionless-radius of $\xi_{\rm max} = 25 \pm 3$ was found to reproduce the extinction observations of L694–2 for radii $r \geq 30''$.

Plummer-like models.— These are empirical models suggested by Whitworth & Ward-Thompson (2001) that capture the essential observed properties of starless cores with a minimum of free parameters. The model assumes that when a prestellar core becomes unstable against collapse at time t=0, it is static and approximates to a Plummer-like density profile (Plummer 1911), of the form:

$$\rho(r, t = 0) = \rho_0 \left[\frac{R_0}{(R_0^2 + r^2)^{1/2}} \right]^{\eta} \tag{7.2}$$

The initial density is therefore uniform for $r \ll R_0$, and falls off as $r^{-\eta}$ for $r \gg R_0$. Whitworth & Ward-Thompson (2001) propose a fixed value of $\eta = 4$ in the model in order to reproduce the relative lifetimes and accretion rates for the Class 0 and Class I phases. For L694–2, the density power law index in the outer regions inferred from near infrared extinction is $p = 2.6 \pm 0.2$ if the core is assumed to be unobscured, but has a steeper value of $p = 3.7 \pm 0.3$ if the core is embedded in a more extended uniform distribution of material, as is suggested by the flattening in the radial profile beyond $r \gtrsim 0.1$ pc (Harvey et al. 2003b). A Plummer-like core with $\eta = 4$ embedded in a more extended cloud can therefore reproduce the extinction observations. The scale radius R_0 is not constrained by the extinction measurements because no flattening is evident in the data (which do not penetrate the $r \lesssim 30''$ inner region).

Broken Power Law models.— These models represent a variation of the Plummer-like model, to allow for an inner density power law index that is non-zero. The density distribution we adopt is of the form:

$$\rho(r) = \frac{\rho_0}{((r/R_0)^{2p} + (r/R_0)^{2\eta})^{1/2}} \tag{7.3}$$

For $r \ll R_0$, the density falls off as r^{-p}, and for $r \gg R_0$, the density falls off as $r^{-\eta}$. We choose this continuous prescription to prevent discontinuities in the first derivatives (which show up in the visibility profile) that would result from including a unphysical sharp break in the density distribution. We choose $\eta = 2.6$ to reproduce the observed extinction without introducing additional structure components. There is some degeneracy between R_0 and p in the resulting visibility (or intensity) profile, since decreasing R_0 or increasing p both produce a steeper emission profile or a flatter visibility profile. The visibility amplitude for a typical starless core profile falls rapidly and is already very low at baselines that are long enough to sample the inner structure that cannot be probed with extinction. Even the high quality visibility dataset that we have obtained from BIMA and the PdBI therefore does not provide sufficient sensitivity to constrain both parameters simultaneously. We therefore choose a fixed value of $R_0 = 30''$ in order to quantify the effect of the inner power law index p. This choice is made on the basis that $R_0 = 30''$ is the largest value of R_0 that is consistent with the extinction data, which will lead to the largest possible value of p allowed by the dataset (since a smaller value of R_0 will necessarily require a shallower p to produce a given visibility amplitude at a given baseline).

Cylinder models.— The isothermal cylinder model is a two dimensional analog of the B-E sphere. The density is a function of the radial coordinate only (Ostriker 1964):

$$\rho(r,z) = \frac{\rho_c}{(1+(r^2/8H^2))^2} \tag{7.4}$$

where $H = a/\sqrt{4\pi G\rho_c}$ is the scale height that is equivalent to the scale radius R_0 in the B-E analysis. The density is uniform near the axis of the cylinder but decays ever more rapidly with increasing radius, asymptoting to a power law of index $p = 4$ for $r \gg H$. The filament is supported radially by pressure gradients, but is unstable in the direction along its axis. The density distribution of the isothermal cylinder is a two dimensional case of the Plummer-like model, with $\sqrt{8}H = R_0$, and with a physical basis for the normalization of the density profile. A cylindrical model can therefore reproduce the observational properties of pre-stellar cores that provided the motivation for the Plummer-like models. In addition, because the isothermal cylinder and the B-E sphere both represent equilibria between self-gravity and gas pressure, the spherically averaged density profile of an isothermal cylinder can also mimic closely that of a B-E sphere, in particular a flat inner region with a steeply falling envelope (Boss & Hartmann 2001). The cylindrical model also provides a basis for interpreting the departures from spherical symmetry in the L694–2 core (Harvey et al. 2003b). A slightly tilted, embedded cylinder with scale height $H = 13.5'' \pm 1.5''$ reproduces the extinction profile for the inner $83''$ (0.1 pc) of the core. In the present study we consider isothermal cylinders viewed along the axis, since the subtle effect of a small tilt angle can not be constrained with the visibility dataset.

Extended Cloud Structure

Both Plummer-like and Isothermal Cylinder models can successfully describe the near-IR extinction observations, if the cores are embedded in an extended distribution of gas. This additional component to the density structure is suggested by the shape of the radial extinction profile, and must be accounted for in the fitting of these types of model. We include the extended cloud structure in the visibility analysis as follows. The extended structure is assumed to be smooth and is therefore resolved out by the interferometers. The only effect of the additional structure is to reduce the total flux that is attributable to the core in this context. The extinction profile of the L694–2 core asymptotes to a color-excess that is approximately 0.2 magnitudes higher than the background, and about a tenth (1/10) of the color excess at 30″ radius (the edge of the flux normalization aperture). We approximate the intensity profile to be flat within 30″ of the core, and assume that the temperature of the extended gas is equal to that in the core, so that the extended structure accounts for 10% of the flux normalization for each of these types of model.

Temperature

A detailed study of the expected dust temperature distribution in starless cores has been performed by Evans et al. (2001). They calculate the temperature distribution, $T_d(r)$, self-consistently using a 1D radiative transport code, and assuming Ossenkopf & Henning (1994) opacities for grains that have grown by coagulation and accretion of thin ice mantles. They find that the Interstellar Radiation Field (ISRF) dominates the heating in the core and is roughly a factor of 3 stronger than heating due to cosmic rays, even at the center of an

opaque core. The effect of the opacity law on $T_d(r)$ is small; the largest difference is at the center of the core, where opacities for coagulated grains that lack mantles cause a lower value of T_d by ~ 0.5 K.

Evans et al. (2001) present the dust temperature distribution $T_d(r)$ for a B-E sphere with outer radius $R_{\rm out} = 0.17$ pc (35000 AU) in which the gas is isothermal at 10 K (their Figure 3). The model has a central density of $n = 1 \times 10^6$ cm^{-3}, and a dimensionless outer radius of $\xi_{\rm max} \simeq 42$, and is heated by an ISRF that combines the infrared behavior from COBE (Black 1994) and the ultraviolet behavior from Draine (1978). The dust temperature varies from a minimum of ~ 8 K in the inner thousand AU of the core, to a maximum of ~ 14 K in the outer regions. The model is similar in radius, but somewhat more centrally condensed than the B-E sphere that best fits the extinction in L694–2 ($R_{\rm out} = 0.17$ pc, $R_0 = 3.4''$ in the computed model; $R_{\rm out} = 0.15 \pm 0.14$ pc, $R_0 = 4.9'' \pm 0.6''$ for L694–2). In addition, the Evans et al. (2001) analysis neglects any shielding by an extended component of material that surrounds the core, as is seen around L694–2 in near-infrared extinction (Harvey et al. 2003b). The degree to which the interior of the L694–2 globule is shielded from the ISRF will differ somewhat from in the Evans et al. (2001) model. However, the Evans et al. (2001) model likely provides an accurate description of the actual temperature profile in L694–2 to within the uncertainties that stem from the inhomogeneities of the ISRF. We therefore adopt the Evans et al. (2001) temperature distribution for use in our modeling. We investigate the sensitivity to the assumed temperature distribution by also exploring models that assume a constant dust temperature of $T_d = 12$ K.

The B-E and Cylinder models used in the model fitting are based on hydrostatic equi-

librium density configurations for a gas cloud that has an isothermal kinetic temperature T_K. The Evans et al. (2001) temperature distribution is calculated using a density model that obeys the same assumption. At high densities efficient gas-dust coupling forces T_K to equal the dust temperature T_d, while at low densities ($n \lesssim 10^4$ cm^{-3}) $T_K \neq T_d$ (Takahashi, Silk, & Hollenbach 1983, Doty & Neufeld 1997). The B-E model that best fits the L694–2 extinction has central density $n \sim 3 \times 10^5$ cm^{-3}, with a center-to-edge density contrast of ~ 400. In the inner regions of L694–2 the kinetic temperature of the gas should decrease in a similar fashion to the dust temperature, but in the outer regions the two temperature distributions may depart. An entirely self-consistent approach to the problem would include a full calculation of the gas energetics, including dust coupling to calculate simultaneous density and (dust) temperature distributions. Such an approach has been followed by Galli, Walmsley & Gonçalves (2002). However, to zeroth order, small departures from isothermality in the kinetic temperature have little effect on the density profile, since the pressure gradient of the gas is dominated by the gradient in the density and not the temperature. The effect of non-isothermality on the resulting emission profile is therefore dominated by the dust temperature dependence of the Planck function. Since the uncertainties that surround the calculation of the dust temperature profile are substantial, the computational overhead of a more self-consistent approach is not justified at this time. We separate the problem into two parts, modeling density profiles assuming a constant gas kinetic temperature, but relaxing the isothermal assumption in order to model the resulting thermal emission from the core.

A remaining issue deals with the appropriate temperature distribution to use for the

cylindrical models, since these are by definition not spherically symmetric. Since no self-consistent 3D dust radiative transfer results are available for this type of model, we have made a very simple approximation, assuming the filament to have an aspect ratio of 2:1 and stretching the Evans et al. (2001) temperature distribution appropriately along the line-of-sight.

Mass Opacity

The mass opacity of dust grains in the millimeter region of the spectrum in protostellar envelopes is uncertain but generally assumed to follow a power law with frequency, $\kappa_\nu \propto \nu^\beta$. The power-law index varies depending on the dust properties, but tends to be bounded by a small range, roughly 1 to 2 (Ossenkopf & Henning 1994). The opacity of the dust affects the temperature distribution of the dust, as described above. For our purposes, only the spectral index is of importance, since we assume a constant opacity (independent of r), and the overall normalization is fixed by matching the MAMBO single dish observation. The spectral index affects the normalization of the models only weakly since the MAMBO flux constraint is made at a wavelength very close to that of the PdBI and BIMA observations. We have adopted $\beta = 1$; the extreme alternative of $\beta = 2$ leads to only a 4% change in flux normalization (for $T_d = 12$ K), which is small compared to the overall 10% uncertainty in the normalization itself.

7.4 Fitting Model Parameters and Evaluating Fit Quality

The basic procedure is to maximize the probability distribution:

$$P(\text{Model} \mid \text{data}) = \prod_i e^{-(Z_i - f(x_i;p,m))^2/2\sigma_i^2} \, e^{-(m-m_0)^2/2\sigma_m^2} \tag{7.5}$$

where the Z_i are the visibility data points with uncertainty σ_i, $f(x_i;p,m)$ are the model data points, p a free parameter in the models, and m a model parameter about which we have a constraint (namely that it is a Gaussian random variable with mean m_0 and standard deviation σ_m). Maximizing the probability distribution is equivalent to minimizing the logarithm of its inverse. Taking account the fact that the Z_i are by nature complex visibilities, we want to minimize a modified χ^2:

$$\tilde{\chi}^2 = \sum_i \frac{|Z_i - f(u,v;p,m)|^2}{\sigma_i^2} + \frac{(m-m_0)^2}{\sigma_m^2} \tag{7.6}$$

The sum/product can extend over any suitable subset of the visibility points. It is useful to be more explicit about the parameters p & m. The free parameter p is used to describe the shape of the model, e.g. the index of the inner part of the broken power-law density distribution. The parameter m allows us to include the observational uncertainties, e.g. the $\sim 10\%$ uncertainty in the normalization of the models derived from the Tafalla et al. (2003) map, and the $\sim 15\%$ uncertainty in the flux calibration for the BIMA data. This is achieved by allowing the BIMA model visibilities to be scaled by a constrained parameter m, assumed to be a Gaussian random variable with mean $m_0 = 1.0$ and standard deviation $\sigma_m = 20\%$. The longer baselines of PdBI do not detect any signal from the L694–2 core. These measurements are used to constrain a limit on the point source contamination and are not included in the model fitting.

For a given model, we evaluate the best fit parameters by minimizing the modified χ^2 distribution. Uncertainties in the parameter values are analyzed using the Monte Carlo technique known as the *bootstrap* (Press et al. 1992). In brief, the dataset is resampled n times (typically $n \sim 200$), each time the fitting process is repeated and the best-fit parameters recorded, until the distribution of best-fit parameters is well sampled. The width of the distribution provides an estimate of the uncertainty in the parameters that best fit the original dataset.

This numerical approach is made necessary by the non-linear nature of the fitting parameters, and is especially useful for this analysis because small variations in the value of the modified χ^2 as defined above may represent surprisingly large variations in fit quality. The nature of the visibility dataset, comprising a very large number of very low signal-to-noise measurements, means that even a model with zero signal will on average reproduce each visibility measurement to within its uncertainty. The resulting shallowness of the χ^2 wells causes two models with slightly differing parameters to seem almost equally good despite the fact that there is ample signal to distinguish them. The numerical approach essentially bypasses this complication. The issue could also be circumvented by binning the visibilities (e.g. radially in (u, v) distance), to increase the signal-to-noise, and then performing a χ^2 fit to the binned values. We avoid this solution because the visibility profiles for the various models are falling steeply at the baselines of interest, and binning the data inevitably introduces a bias in the fit due to contracting the range of baseline vectors to a single length at the center of the bin. We use binning only as a graphical tool in order to demonstrate the fit quality of a particular model.

7.5 Results and Analysis

7.5.1 Limits on Point Source Flux

The PdBI dataset covers baselines from 12 to 80 kλ, with an overall rms noise of 0.9 mJy. The visibility data are consistent with the noise. The long baselines covered by the PdBI data therefore provide an important constraint on the maximum compact component of the flux from the L694–2 core: $F_c < 2.7$ mJy (3 σ). For optically thin dust, this limiting flux corresponds to an implied (disk) mass limit of $M \lesssim 5 \times 10^{-4}$ M$_\odot$ (60 K/$T_{\rm disk}$) for an opacity $\kappa_{1.3\ {\rm mm}} = 0.02$ cm^2 g^{-1}. This limit is roughly an order of magnitude lower than the 0.002–0.3 M$_\odot$ range of disk masses observed around T-Tauri stars by Beckwith et al. (1990), and further demonstrates the "starless" nature of the L694–2 core.

The flux limit allows an estimate of the maximum bolometric luminosity for any compact component embedded in the L694–2 core. For a simple estimate, we assume a dust opacity spectral index of unity, and model the compact component as a graybody of the form:

$$F_\nu \; = \; B_\nu(\langle T_{\rm dust}\rangle)\,[1 - \exp(-\tau_\nu)]\,\Omega_S \;, \tag{7.7}$$

where $B_\nu(\langle T_{\rm dust}\rangle)$ denotes the Planck function at frequency ν for a mean dust temperature $\langle T_{\rm dust}\rangle$, τ_ν is the dust optical depth, and Ω_S the solid angle subtended by the source (e.g. Beckwith et al. 1990). Since the envelope is entirely optically thin at 1.3 mm, the graybody must have a flux that is ≤ 2.7 mJy at this wavelength. For a given mean dust temperature, this constraint fixes the mass of the compact component. The only remaining parameter is the radius R of the component, which essentially identifies the wavelength at which the

emission becomes optically thick.

For a compact component to remain undetected in our PdBI observations implies that its bolometric luminosity is:

$$L_{\rm bol} \lesssim 0.07\ {\rm L}_\odot\ (R/100\ {\rm AU})^{0.1}\ (\langle T_{\rm disk}\rangle/50\ {\rm K})^{3.9} \tag{7.8}$$

Note that these power law dependencies are an approximation and are not accurate for changes in the parameters by factors of more than ~ 2. The dependences on temperature and radius can be understood in the following way. The dominant contribution to the luminosity comes from the Rayleigh-Jeans region of the Planck function, in which the emission is optically thin (for this typical size scale and temperature, the compact component becomes optically thick slightly to the Wien side of the peak in the Planck function). If the emission from beyond the peak in the Planck function is entirely negligible, then the luminsosity is proportional to: $L \propto \int_0^{\nu_{\rm max}} \kappa_\nu \nu^2 d\nu$. Note that the flux constraint at 1.3 mm causes there to be no temperature dependence in the integrand. Using the Wien law for $\nu_{\rm max} \propto \langle T\rangle$, and $\kappa_\nu \propto \nu$, then gives $L_{\rm bol} \propto \langle T\rangle^4$. The contribution of the optically thick emission causes the actual temperature dependence to depart from this relation, and introduces a weak dependence on the radius of the compact source.

The limit the PdBI observations place on the maximum bolometric luminosity of any embedded compact object is substantially lower than the IRAS limit for L694–2 of ~ 0.3 L$_\odot$. Reprocessing of the warm compact emission to long wavelengths by the envelope essentially allows a large bolometric luminosity to remain hidden below the IRAS detection limit.

7.5.2 Density Structure

The PdBI data constrains the maximum compact component of dust emission, which allows us to proceed to fit for the envelope structure using the BIMA data at shorter baselines. The envelope visibility profiles fall steeply with increasing baseline. (Note that a flatter emission profile leads to a steeper visibility falloff.) At the longer BIMA baselines, the visibility amplitudes for the best fit models falls well below the signal-to-noise of the entire BIMA dataset. This makes restricting the visibility fitting to the shorter baselines advisable, since extending the fitting range to longer baseline adds noise but no signal. Having experimented with various upper limits on the baseline length, we found that an upper limit of 10 kλ was optimal. Increasing the upper limit to 15 kλ, or 20 kλ did not change the results but produced higher values of the reduced χ^2. The visibility dataset to which the models were fit contains 6424 visibility measurements (each a 3.45 minute integration) and covers baselines from 5 to 10 kλ. The rms noise in this reduced dataset is 3.3 mJy. Table 7.2 summarizes the results from the χ^2 fits to the four types of model described in Section 7.3.1. Below we describe these results.

Bonnor-Ebert Sphere.— the model that best fits the visibility data has dimensionless outer radius $\xi_{\rm max} = 18\,^{+3}_{-4}$ (Fit I). At the 2 σ level this is consistent with the results of the extinction study, where a B-E sphere with $\xi_{\rm max} = 25 \pm 3$ reproduced the observed color excess.

Plummer-like model.— the embedded model that best fits the visibility data has scale radius $R_0 = 26\,''\,^{+4}_{-3}\,''$, or 6500^{+1000}_{-750} AU (Fit II). This turn-over radius is consistent with the

Table 7.2. Summary of the Density Model Fits

Fit	Density Model	Fitted Model Parameter	Calibration scaling M	χ^2_ν
I	Bonnor-Ebert	$\xi_{\max} = 18^{+3}_{-4}$	0.90 ± 0.04	1.2520
II	Plummer-like	$R_0 = 26'' {}^{+4}_{-3}{}''$	0.90 ± 0.05	1.2521
III	Broken Power Law	$p = 0.9^{+0.12}_{-0.16}$	0.92 ± 0.04	1.2519
IV	Cylinder	$H = 12'' {}^{+3.0}_{-1.5}{}''$	0.90 ± 0.05	1.2520

Visser (2000) analysis of SCUBA data, which fit a broken power law with a transition to a shallower index within a break radius of $\sim 32''$ (8000 AU).

Broken Power law.— the model that best fits the visibility data has a power law index in the inner region ($r < 30''$) of $p = 0.9^{+0.12}_{-0.16}$ (Fit III). The turn-over radius used in this model is similar to that from the Visser (2000) analysis, and the fitted inner power law index is consistent with her result of $p = 0.8$ (no uncertainties are given), despite their use of an isothermal dust temperature distribution. Note that the use of a smaller turn-over distance results in a lower fitted value of p. The above result should therefore be construed as a "mean" index in the $r < 30''$ (7500 AU) region, or as an upper limit on the power law index in the innermost regions.

Cylinder.— the end-on cylindrical model that best fits the visibility data has scale height $H = 12'' {}^{+3.0}_{-1.5}{}''$, or 3000^{+750}_{-400} AU (Fit IV). This is consistent with the results of the extinction study, where a slightly tilted cylinder with $H = 13.5'' \pm 1.5''$ best matched the observed color excess.

For each of the best fit models, the fitted value of the scaling parameter is $m \simeq 0.9 \pm 0.05$. That the preferred value is similar for each model and not unity suggests that the data prefer a particular slope of visibility profile that when extrapolated back to zero baseline has 10% lower normalization than the MAMBO flux. This difference is well within the combined uncertainties of the MAMBO flux measurement and the BIMA calibration accuracy (total $\sim 20\%$).

Figure 7.1 shows plots of visibility amplitude vs. (u, v) distance for the various best fit models, and models that differ by $\pm 2\,\sigma$ in the fitting parameters. The profiles of the best fit models are remarkably similar, and we return to this point in Section 7.5.3. The mean signal in the BIMA dataset used to fit the models is shown on the plots (filled circle) with $\pm 2\,\sigma$ error bar. The binning introduces an uncertainty (and/or bias) in the appropriate (u, v) distance for the data point, that is not present in the model fitting procedure. For each type of model, we have adopted the (u, v) distance that provides a match with the best-fit model. This is motivated by purely graphical reasons, but we note that the mean baseline length weighted by the signal to noise of the best fit model (for constant noise on each baseline) provides an essentially indistinguishable (u, v) coordinate. However, the greater spread of the fitted models compared to the binned data point demonstrates the effect of this "smearing" of the signal in (u, v) distance.

The plots in Figure 7.1 also show $\pm 2\,\sigma$ confidence intervals of an azimuthally averaged synthetic visibility profile derived from the Tafalla et al. (2003) MAMBO map of L694–2. The visibility profiles are computed assuming the MAMBO map to be the true intensity distribution convolved with a Gaussian beam of $11''$ FWHM. No assessment has been made

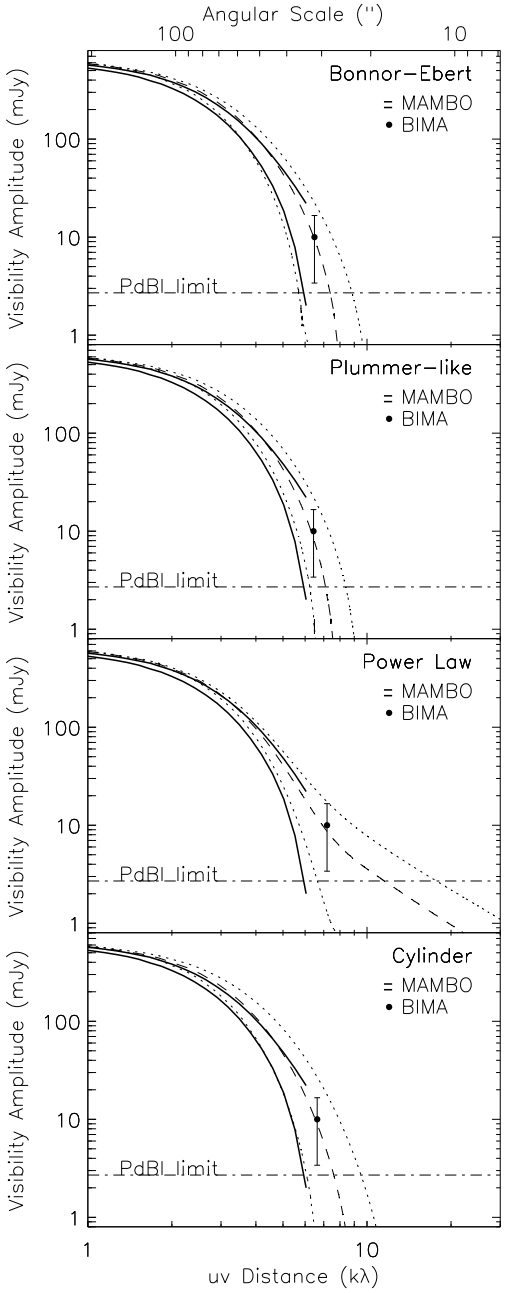

Fig. 7.1.— Visibility amplitude vs. (u, v) distance for L694–2 at 1.3 mm, for the best-fitting models (dashed lines) and models that deviate by $\pm 2\,\sigma$ in the fitting parameters (dotted lines). The binned BIMA visibility amplitude in the baseline range 5 to 10 kλ is also shown (circle), with a $\pm 2\,\sigma$ error bar. The PdBI limit on a point-like component (> 12 kλ) is shown as a horizontal (dash-dot) line. The solid lines represent $\pm 2\,\sigma$ intervals of the azimuthally averaged synthetic visibility profile derived from the MAMBO map. See text for further explanation.

for systematic errors in the profile due to chopping and subsequent reconstruction of the MAMBO observations. The synthetic confidence intervals are extended until the the signal to noise drops below 2 (i.e. the intervals become consistent with zero signal).

Systematic Uncertainties

Table 7.3 lists the main sources of systematic uncertainty along with the level of uncertainty they produce in the fitted density parameters ($\xi_{\rm max}$, r_0, p, & H). The various systematic errors are discussed below, in rough order of importance.

Dust temperature distribution.— This is the largest source of systematic uncertainty. The temperature distribution that has been assumed in the analysis varies from $\sim$ 8 K at the center to $\sim$ 14 K in the outer regions, and it is motivated by physical argument. Nevertheless, the profile is probably uncertain at the level of $\pm$2 K. To study the effect of this uncertainty on the inferred density structure, we have repeated the analysis for each model, replacing the physical temperature distribution with an isothermal distribution at 12 K. The removal of the central minimum in the temperature profile results in a given density model producing a steeper emission profile and a shallower visibility profile. The density structure inferred is therefore less centrally concentrated than with the physical temperature profile. The effect is of a similar magnitude for all of the models: the best-fit parameters are changed by close to 2 σ.

Table 7.3. Summary of systematic uncertainties in fitted parameters

Model Assumption	Variation	Resulting Systematic Error (σ) [1]
Temperature distribution	$T_d = T_{\rm phys}(r) \longrightarrow 12$ K	~ 2
Central point source flux	$F \sim 2$ mJy	~ 1
Central position	$\delta\theta \lesssim 4''$	~ 1
Neglect extended structure [2]	$F_0(r < 30'') = 80$ mJy $\longrightarrow 0$	~ 0.5
Outer boundary of L694–2 [3]	$\delta R_{\rm out}/R_{\rm out} \lesssim 50\%$	$\ll 1$
Dust opacity spectral index	$\beta = 1 \longrightarrow 2$	$\ll 1$

[1]Systematic error in the fitted model parameter given in units of σ, the random error in the parameter listed in Table 7.2. Note that each quoted systematic error corresponds to a *shallowing* of the inferred density profile.

[2]Applies to Plummer-like and Cylinder models only

[3]Does not apply to B-E sphere; for the B-E model, increasing the outer radius increases $\xi_{\rm max}$ in proportion to $R_{\rm out}$, keeping constant scale radius R_0

Unresolved compact component.— The PdBI data limit the maximum contribution to the emission from an unresolved compact component: $F_c < 2.7$ mJy (3 σ). Including a dimmer compact component in the model fitting essentially reduces the visibility amplitude that is attributable to the envelope and results in fitted density structures that are more shallow. For a point source flux of $F_c = 2$ mJy, the density structure parameters are changed by roughly 1 σ.

Central position.— The flatness of the inner density profile and the lack of a detected compact component make the appropriate central position for the L694–2 core uncertain.

However, the baselines of the BIMA visibilities from which the density structure is inferred are short and correspond to a fringe size of $\sim 20''$. This means that the results are not very sensitive to small changes in the adopted central position (the pointing center of the PdBI observations). The signal in the combined visibilities peaks at 10 mJy within $1''$ of the adopted central position — the peak of N_2H^+(1–0) emission. A shift in the central position of $5''$, i.e. the shift between the fitted center from the extinction study and central position assumed here, leads to a ~ 2 mJy reduction in the binned signal and a 1 σ change in the density structure parameters, corresponding to shallower density profiles.

Extended structure.— A leading source of systematic uncertainty in the L694–2 extinction study was the effect of the contribution of the extended structure in which the core appears to be embedded (Harvey et al. 2003b). Including this additional component to the models lead to inferred core density profiles that were significantly more steep, consistent with Plummer-like and isothermal cylinder models. In the present study, this uncertainty has much smaller effect on inferred structure. Since the extended structure must be largely resolved out by the interferometers, neglecting the extended structure entirely leads to only a 10% increase in the amplitudes of the visibility profiles of the model cores. Repeating the fitting analysis for the two types of model in this context results in inferred density profiles that are ~ 0.5 σ more shallow.

Outer boundary.— The outer boundary of the L694–2 core has little effect in the modeling due to the limited field of view of BIMA and PdBI. For BIMA, the intensity distribution at the assumed outer edge of the core is suppressed by a factor ~ 0.05 due to the antenna pattern. Moreover, the intensity at the edge is already lower than the intensity at the center

by a factor of ~ 500 (Fit I). Modifying the outer boundary therefore has no effect on the shape of the inferred density profile. However, for the B-E sphere (Fit I), changing the outer radius does modify the density structure parameter $\xi_{\rm max}$ because this parameter describes the dimensionless profile, not the physical profile. For this fit, the alternative structure parameter, the scale radius $r_0 = R_{\rm out}/\xi_{\rm max}$ is unchanged.

Dust opacity spectral index.— The dust opacity adds systematic error via the use of the spectral index to transform the flux normalization from MAMBO to the frequency at which our observations were made. To some extent, the appropriate MAMBO frequency itself depends on the spectral index, because of the broad bandwidth used in the single dish bolometer observations. The spectral index of the dust opacity should lie in the range β =1–2. We have used $\beta = 1$ throughout; an alternative extreme, $\beta = 2$, leads to only a 4% reduction in the flux normalization, and to inferred density structure that is more shallow, but to a degree that is negligible in comparison to the other sources of error (both systematic and random).

7.5.3 Discussion: A Physical Density Distribution for L694–2

The fitted physical models demonstrate clearly that the steep density gradient observed in the $r > 30''$ region with extinction (Harvey et al. 2003b) does not continue in the inner region that could not be probed in that study. This is consistent with the modeling of single dish dust emission observations by Visser (2000) and Tafalla et al. (2003).

The visibility profiles of the best fit models shown in Figure 7.1 are remarkably similar to each other, only the power law model differing enough to be distinguishable by eye, and

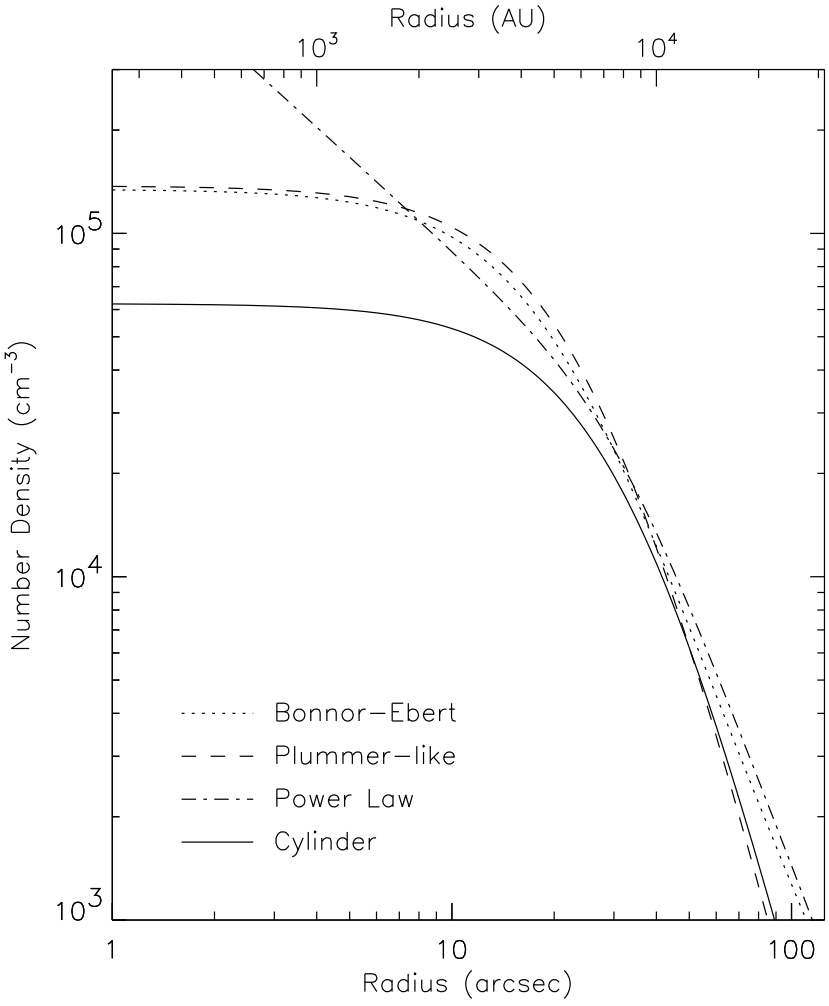

Fig. 7.2.— Number density of molecular hydrogen vs. radius for the various best fit models of L694–2. The number density calculation assumes a dust opacity of $\kappa_{1.3\mathrm{mm}} = 0.02$ cm^2 g^{-1}, a mean molecular weight of $\mu = 2.29$, and a Hydrogen mass fraction $X_{\mathrm{H}} = 0.73$. The best-fit Bonnor-Ebert (*dotted*) and Plummer-like (*dashed*) profiles are nearly identical. The cylindrical model (*solid*) has density a factor ~ 2 lower due to the extension of the cylinder along the line-of-sight.

then only at long baselines. This provides an interesting demonstration of the degeneracy of the various models for starless core density structure. Figure 7.2 presents a plot of the best-fit density models. The normalization of the density assumes an opacity of $\kappa_{1.3\mathrm{mm}} = 0.02$ cm^2 g^{-1}, which is uncertain by a factor of ~ 5 or more (Ossenkopf & Henning 1994). At large radii the B-E and Power-law models differ from the Plummer-like and cylinder models due to the fact that the latter models are assumed to be embedded in an extended uniform distribution of gas. The Plummer-like and B-E models are almost identical, and have central densities that differ by only 5% ($n(\mathrm{H_2}) = 1.4 \times 10^5$ cm^{-3} with uncertainty $\sim 50\%$). The density profile of the end-on cylinder departs significantly from the the B-E and Plummer-like profiles. The profile is more shallow with much lower central density ($n(\mathrm{H_2}) = 5.1 \times 10^4$ cm^{-3} with uncertainty $\sim 30\%$). This occurs despite the identical form of the expressions for the cylinder and Plummer-like models (with $R_0 = \sqrt{8}H$), and the fact that the cylinder and B-E models both represent a balance between self-gravity and thermal pressure. The difference derives from the lower dimensionality of the cylindrical model; a given line-of-sight corresponds to a constant "radius", and hence there is no radial integration that for the spherically symmetric models makes the column density profiles more shallow than the density profiles. In addition, the extension of the cylinder along the line-of-sight means that the densities are correspondingly lower at a given radius. The asymmetry of the L694–2 core viewed in extinction provides a basis for preferring the cylindrical model over the others. A tilted cylinder with $H = 13.5$, $L \sin\phi = 0.14$ pc ($L \simeq 0.2$–0.5, and $\phi \simeq 20$–$45°$), and central density ($n(\mathrm{H_2}) = 4 \times 10^4$ cm^{-3} embedded in a uniform distribution of gas with column density $N(H + H_2) \sim 6 \times 10^{21}$ (L/0.5 pc) cm^{-2}, successfully reproduces the dust emission visibility profile, as well as the profile and asymmetry of the

dust extinction map. The instability of the cylindrical model along its axis is also consistent with the inward motions in L694–2 inferred from molecular spectral lines (Lee, Myers & Tafalla 2001).

As noted above, the inner power law index of the fitted broken power law model ($p = 0.9\,^{+0.12}_{-0.16}$, Fit II) may be construed both as a "mean" index in the $r < 30''$ region, and as an upper limit on the index in the innermost regions (due to the trade-off between turn-over radius and power law index in the inferred visibility profile). The former is illustrated by the fact that the radially averaged "mean" effective power law index for the best-fit Plummer-like model is $\bar{p} = 0.86$ over the range in radius $0 \leq r \leq R_0$ (with $R_0 = 26''$). The profile is consistent with the Visser (2000) study who found that a similar index ($p = 0.8$) and turn-over radius ($R_0 = 32''$) reproduced the SCUBA map. The index in the inner region is much less than that observed in the outer envelope and shows that the density distribution in the inner region of the L694–2 core has clearly not relaxed fully, along the lines assumed in the inside-out collapse of Shu (1977), despite the presence of extended inward motion in the gas (Lee et al. 2001). These inward motions may reflect the contraction of a prolate core along its major axis (Harvey et al. 2003b).

7.6 Summary

We present a study of the density distribution of the candidate contracting starless core L694–2 using high resolution 1.3 mm dust continuum observations from BIMA and the IRAM PdBI. In summary:

1. The PdBI visibility data span baselines from 12 to 80 kλ (spatial scales from $\sim$ 500 to $\sim$ 5000 AU) and do not detect any significant emission from the core. This provides a stringent constraint on the maximum point source flux: $F_c < 2.7$ mJy (3 σ). This flux limit corresponds to a very small disk mass, $M \lesssim 5 \times 10^{-4}$ M$_\odot$ (60 K/$T_{\rm disk}$), and bolsters the "starless" interpretation of the L694–2 core.

2. The BIMA visibility data in the baseline range 5 to 10 kλ (spatial scales $\sim 10^3$–10^4 AU) detect emission from the core and are used to constrain models for the density structure. That no signal is evident on baselines beyond 10 kλ confirms the flat emission profile in the inner regions, and a significant change in behavior from the steep density profile for $r \gtrsim 8000$ AU inferred from near infrared extinction of background stars (Harvey et al. 2003b). We fit four types of model for starless core density structure that can match the steep density gradient in the outer regions inferred from extinction. We adopt a temperature distribution that decreases in the inner regions due to shielding from the ISRF (Evans et al. 2001). The best fit Bonnor-Ebert sphere has dimensionless outer radius $\xi_{\rm max} = 18\,^{+3}_{-4}$ (1 σ). The best fit Plummer-like model has turn-over radius $R_0 = 26\farcs{}^{+4}_{-3}\,\farcs{}$ (6500^{+1000}_{-750} AU). The best fit broken power law model has index $p = 0.9\,^{+0.12}_{-0.16}$ (this model uses the maximum allowable turn-over radius of $R_0 = 30''$ (7500 AU) and provides an upper limit on the index at the center of the core). The best fit end-on isothermal cylinder has scale height $H = 12\farcs{}^{+3.0}_{-1.5}\,\farcs{}$ (3000^{+750}_{-400} AU).

3. We consider the effects of various sources of systematic uncertainty on the derived density structure. The largest uncertainty comes from the dust temperature distri-

bution; assuming an isothermal core modifies the best fit parameters by $\sim 2\,\sigma$, and makes the inferred density profiles more shallow. A possible weak compact component to the emission ($F \sim 2$ mJy) and the appropriate central position ($\delta\theta \lesssim 4''$) are the main remaining sources of uncertainty. Both of these uncertainties lead to $\sim 1\,\sigma$ changes in the inferred model parameters, again to shallower density profiles.

4. The density profiles of the various best-fit models are nearly indistinguishable at baselines shorter than ~ 10 kλ. There is a strong degeneracy between the models for starless core density structure. The two physical models (B-E sphere and isothermal cylinder) represent a balance between self-gravity and thermal pressure, and therefore they produce similar profiles. The asymmetry of the L694–2 core evident in the extinction map may provide a basis for favoring the cylindrical model. A cylinder slightly tilted to the line-of-sight with $H = 13.5''$, $L \sin\phi = 0.14$ pc ($L \simeq 0.2$–0.5, and $\phi \simeq 20$–$45°$) and central density ($n(\mathrm{H_2}) = 4 \times 10^4$ cm^{-3} embedded in a uniform distribution of gas with column density $N(H + H_2) \sim 6 \times 10^{21}\,(L/0.5$ pc) cm^{-2} reproduces both the dust emission and extinction measurements.

Acknowledgements

We acknowledge the IRAM and BIMA staff for carrying out the observations. We are especially grateful to Roberto Neri and Jerome Pety for coordinating remote reduction of the IRAM PdBI observations.

Conclusions

The origin of stars represents one of the most fundamental unsolved problems of contemporary astronomy. In particular, the initial conditions of the protostellar collapse process have been the subject of controversy, as have the dynamics of the collapse. Better measurements of star forming cores are needed to further our understanding of this process.

I have used two newly feasible observational techniques — dust extinction, and dust emission — and intensive computer modeling to measure the density structure of a sample of dense molecular cloud cores that are in the process of evolving to form stars: protostellar collapse candidate Barnard 335, and candidate contracting starless core Lynds 694–2. The cores are fairly isolated, round condensations, situated very close to each other on the sky (separated by less than 4°). Indeed the cores have likely formed from the same parent molecular cloud complex. Molecular spectral lines observed in both cores exhibit strong redshifted self absorption, an indication that inward motions are likely present. Yet despite their similar mass and history, the two cores differ significantly in their evolutionary state: the B335 core harbors an embedded young stellar object and a strong bipolar outflow, while L694–2 is apparently starless. It is an intriguing possibility that B335 might represent a

later stage of the star formation process to which the L694–2 core will one day evolve.

The dust extinction study of B335 (Chapter 2) is the first application of this method to a candidate protostar, and the only extinction work that has been done with the Hubble Space Telescope. The extinction data include data taken at the W.M. Keck Observatory, and provide a quantitative test of the "inside-out" collapse model previously proposed to explain molecular line profiles observed toward this region. We find that the *shape* of the density profile is well matched by the collapse model, but that the *amount* of extinction corresponds to larger column densities than predicted. The bipolar outflow driven by the embedded young star strongly affects the extinction through the core; modeling the outflow as a hollowed-out bipolar cone provides a good match to the observations. The shape of the inferred density structure provides the strongest evidence yet for the inside-out model of protostellar collapse.

The dust emission studies of B335 (Chapters 3 & 4) are based on observations made with the Plateau de Bure Interferometer (PdBI) of the Institut de Radioastronomie Millimetrique (IRAM) at subarcsecond resolution, probing spatial scales down to < 100 AU. These observations provide the first millimeter-wave flux measurement for the circumstellar disk, and constrain the inner density profile with a precision that is unique amongst protostellar cores. The inner density structure is consistent with the $r^{-1.5}$ profile of gravitational free-fall, in accord with basic expectations for the formation of a star. The properties of the disk are typical of the disks around T-Tauri stars.

The dust extinction study of L694–2 (Chapter 6) utilizes data from the European Southern Observatory New Technology Telescope. The density profile in the outer regions

is significantly steeper than the value for the singular isothermal sphere, the initial condition of the inside-out collapse model. The steep density gradient represents an unstable configuration of material in the L694–2 core that may be related to the inward motions inferred from spectral line profiles. A hydrostatic isothermal cylinder viewed at a small inclination to its axis matches the observed extinction remarkably well, including the asymmetry of the L694–2 core. In addition, this model provides a basis for understanding why the observed column density normalization is a factor of ~ 4 larger than predicted by spherically symmetric models. If L694–2 is a prolate structure, aligned close to the line-of-sight, then the full extent (mass) of the core is underestimated if one assumes a symmetry between the profile of the core in the plane-of-the-sky and the line-of-sight. If such a prolate core is sufficiently magnetized then it may not fragment, and later evolution might produce a protostar similar to B335 with mass larger than expected for a spherically symmetric core.

The dust emission study of L694–2 (Chapter 7) is based on data from the Berkeley Illinois Maryland Array (BIMA) and the IRAM PdBI that probe to 500 AU scales. The long baseline PdBI observations detect no emission from the core, and limit the maximum luminosity of any compact object that may be hidden in this apparently starless core. This further bolsters the "starless" interpretation of the L694–2 core. The shorter baseline BIMA data provide clear evidence for a turn-over from the steep density profile observed in the outer regions in dust extinction to substantially more shallow behavior in the inner regions (< 7500 AU). The competing models for starless core structure — Bonnor-Ebert, Plummer-like, broken power law, and isothermal cylinder models — produce very similar flattened profiles that fit the data well, but cannot be distinguished. The turn-over observed in the

L694–2 density distribution suggests that pressure forces still support the core, and that it has not fully relaxed as in the inside-out collapse model, despite the extended inward motions inferred from molecular line observations (Lee, Myers, & Tafalla 2001). In the context of the cylindrical density model that reproduces both the extinction and emission observations of L694–2, these inward motions may represent the contraction of a prolate core along its major axis.

The Future

In the next few years, a number of new telescopes will come online that should provide much opportunity to extend the work presented in this thesis. In particular, the Smithsonian Sub-Millimeter Array (SMA) will allow the dust emission work to be done at new shorter wavelengths. Studing the emission at an additional short wavelength that is beyond the Rayleigh-Jeans region of the spectrum for these cold dense cores should allow the degeneracy between the dust temperature and density to be broken. In addition, this summer should see the launch of the Space Infrared Telescope Facility, the next of NASA's family of great orbiting observatories. This telescope should be able to study dust extinction and emissiopn from dense cores at a wide range of infrared wavelengths, most of which cannot be observed from the ground.

Further in the future, the Attacama Large Millimeter Array (ALMA) should revolutionize the study of dense cores in dust emission, due to unprecendented sensitivity, resolution, and image making capability at sub-millimeter and millimeter wavelengths. In a similar

way, the Next Generation Space Telescope (NGST) will revolutionize the study of dust extinction, providing significantly higher sensitivity and resolution than even the Hubble Space Telescope. Extinction mapping of protostellar cores has been expressed as one of NGST's mission goals: our extinction work on B335 may therefore be the first of many Space Telescope extinction studies of star forming dense cores.

References

Adams, F.C. 1991, ApJ, 382, 544

Alves, J.F., Lada, C.J., & Lada E.A. 2001, Nature, 409, 159

Alves, J.F., Lada, C.J., & Lada E.A. 1999, ApJ, 515, 265

Alves, J.F., Lada, C.J., Lada E.A., Kenyon, S.J. & Phelps R. 1998, ApJ, 506, 292

André, P., & Montmerle, T. 1994, ApJ, 420, 837

André, P., Ward-Thompson, D., & Barsony, M. 1993, ApJ, 406, 122

André, P., Ward-Thompson, D., & Barsony, M. 2000, in Protostars and Planets IV, eds. V. Mannings, A.P. Boss and S.S. Russell, (Tucson: University of Arizona Press), p. 59

Anglada, G., Villuendas, E., Estalella, R., Beltrán, M.T., Rodríguez, L.F., Torrelles, J.M., & Curiel, S. 1998, AJ, 116, 2953

Anglada, G. 1995, RMxAA, 1, 67

Bastien, P. 1983, A&A, 119, 109

Beckwith, S.V.W. 1999, in The Origin of Stars and Planetary Systems, ed. C.J. Lada and N.D. Kylafis (Kluwer Academic Publishers), 579

Beckwith, S.V.W., Sargent, A.J., Chini, R.S. & Güsten, R. 1990, AJ, 99, 924

Beichman, C.A., Myers, P.C., Emerson, J.P., Harris, S., Mathieu, R., Benson, P.J. & Jennings, R.E. 1986, ApJ, 307, 333

Beichman, C. et al. 1988, *Infrared Astronomical Satellite (IRAS) Catalogs and Atlases, vol. 1, Explanatory Supplement*, NASA RP-1190 (Washington, DC: GPO)

Benson, P.J., & Myers, P.C. 1989, ApJs, 71, 89

Bessell M.S., & Brett, J.M. 1988, PASP, 100, 1134

Black, J.H. 1994, ASP Conf. Ser. 58, The First Symposium on the Infrared Cirrus and Diffuse Interstellar Clouds, ed. R.M. Cutri & W.B. Latter (San Francisco: ASP), 355

Bohlin, R.C., Savage, B.D. & Drake, J.F. 1978, ApJ, 224, 132

Bok, B.J., & Cordwell, C.S. 1973, in Molecules in the Galactic Environment, ed. T. Gehrels (Tucson: University of Arizona Press), p. 288

Bok, B.J. & McCarthy, C.C. 1974, ApJ, 79, 42

Bonnor, W. 1956, MNRAS, 116, 351

Boss, A.P., & Hartmann, L.W. 2001, ApJ, 562, 842

Brown, D.W., Chandler, C.J., Carlstrom, J.E., Hills, R.E., Lay, O.P., Matthews, B.C., Richer, J.S. & Wilson, C.D. 2000, MNRAS, 319, 154

Butner, H.M., Evans, N.J.II, Harvey, P.M., Mundy, L.G., Natta, A. & Randich, M.S. 1990, ApJ, 364, 164

Cabrit, S., Goldsmith, P.F. & Snell, R.L. 1988, ApJ, 334, 196

Carpenter, J.M. 2001, AJ, 121, 2851

Casali, M. & Hawarden, T. 1992, JCMT-UKIRT Newsl., No. 4, 33

Caselli, P., Walmsley, C.M., Zucconi, A., Tafalla, M., Dore, L. & Myers, P.C. 2002, ApJ, 565, 331

Chandler, C.J. & Sargent, A.L. 1993, ApJ, 414, 29

Chandrasekhar, S. 1967, in *An Introduction to the Study of Stellar Structure*, (Dover, Toronto), p. 156

Chini, R. 1981, å, 99, 346

Choi, M., Evans, N.J.II, Gregerson, E.M., Wang, Y. 1995, ApJ, 448, 742

Ciolek, G.E., & Basu, S. 2000, ApJ, 529, 925

Ciolek, G.E. & Mouschovias, T.Ch. 1996, ApJ, 468, 749

Condon, J.J. 1984, ApJ, 287, 461

Crutcher, R.M. & Troland, T.H. 2000, ApJ, 537, 139

Crutcher, R.M., Troland, T.H., Goodman, A.A., Heiles, C., Kazes, I. & Myers, P.C. 1993, ApJ, 407, 175

de Geus, E.J. & Burton W.B. 1991, A&A, 246, 559

Dickman, R.L. 1978, ApJ, 83, 363

Doty, S.D. & Leung, C.M. 1994, ApJ, 424, 729

Draine, B.T. 1978, ApJs, 36, 595

Ebert, R. 1955, *Z.Astrophys.*, 37, 217

Elias, J.H. 1978, ApJ, 224, 857

Emerson, J.P. 1988, in *Formation and Evolution of Low Mass Stars,* eds. Dupree & Lago, p. 21

Evans, N.J.II, Rawlings, J.M.C, Shirley, Y.L., & Mundy, L.G. 2001, ApJ, 557, 193

Foster, P.N. & Chevalier, R.A. 1993, ApJ, 416, 303

Frerking, M.A. & Langer, W.D. 1982, ApJ, 256, 523

Frerking, M.A., Langer, W.D. & Wilson, R.W. 1987, ApJ, 313, 320

Galli, D. & Shu, F.H. 1993, ApJ, 417, 220

Galli, D., Walmsley, M., & Gonçalves, J. 2002, A&A, 394, 275

Goldsmith, P.F., Snell, R.L., Hemeon-Heyer, M. & Langer, W.D. 1984, ApJ, 286, 599

Goodman, A.A, Bastien, P., Myers, P.C., & Ménard, F. 1990, ApJ, 359, 363

Gordon, M.A. 1988, ApJ, 331, 509

Harvey, D.W.A., Wilner, D.J., Alves, J.F., Chen, H., Lada, C.J. & Myers, P.C. 2001, ApJ, 563, 903

Harvey, D.W.A, Wilner, D.J., Di Francesco, J., Lee, C.-W., Myers, P.C., & Williams, J.P. 2002, AJ, 123, 3025

Harvey, D.W.A., Wilner, D.J., Myers, P.C., Tafalla., M., & Mardones, D. 2003a, ApJ, 583, 809

Harvey, D.W.A., Wilner, D.J., Lada, C.J., Myers, P.C. & J. Alves 2003b, ApJ, *accepted*

Harvey, D.W.A., Wilner, D.J., Myers, P.C. & Tafalla, M. 2003c, ApJ, *accepted*

Harvey, D.W.A., Wilner, D.J., Myers, P.C. & Tafalla, M. 2003d, ApJ, *submitted*

Henriksen, R., Andre, P., & Bontemps, S. 1997 å, 323, 549

Heyer, M.H., Vrba, F.J., Snell, R.L., Schloerb, F.P., Storm, S.E., Goldsmith, P.F., & Storm, K.M. 1987, ApJ, 321, 855

Hirano, N., Kameya, O., Kasuga, T. & Umemoto, T. 1992, ApJ, 390, 85

Hirano, N., Kameya, O., Nakayama, M. & Takakubo, K. 1988, ApJ, 327, 69

Hodapp, K.-W. 1998, ApJl, 500, 183

Hogerheijde, M.R., van Dishoeck, E.F., Salverda, J.M. & Blake, G.A. 1999, ApJ, 513, 350

Hotzel, S., Harju, J., & Juvela, M. 2002, å, 395, 5

Jones, T.J., Hyland, A.R. & Bailey, J. 1984, ApJ, 282, 675

Jones, T.J., Hyland, A.R., Robinson, G., Smith, R. & Thomas, J. 1980, ApJ, 242, 132

Kawamura A., Kun, M., Toshikazu, O., Vavrek, R., Domsa, I., Mizumo, A., & Fukui, Y. 2001, PASJ, 53, 1097

Keene, J., Davidson, J.A., Harper, D.A., Hildebrand, R.H., Jaffe, D.T., Loewenstein, R.F., Low, F.J. & Pernic, R. 1983, ApJ, 274, 43

Keene, J. & Masson, C.R. 1990, ApJ, 355, 635

Kenyon, S.J., Calvet, N. & Hartmann, L. 1993, ApJ, 414, 676

Koornneef, J. 1983, A&A, 128, 84

Krügel, E., Stenholm, L.G.,Steppe, H., Sherwood, W.A. 1983, A&A, 127, 195

Lada, C.J. 1985, ARA&A, 23, 267

Lada, C.J., Alves, J.F. & Lada, E.A. 1999, ApJ, 512, 250

Lada, C.J., Lada, E.A., Clemens, D.P. & Bally, J. 1994, ApJ, 429, 694

Larson, R.B. 1969, MNRAS, 145, 271

Larson, R.B. 1972, MNRAS, 156, 437

Larson, R.B. 1985, MNRAS, 214, 379

Lee, C.W., Myers, P.J., & Tafalla, M. 2001, ApJs, 136, 703

Lee, C.W., Myers, P.J., & Tafalla, M. 1999, ApJ, 526, 788

Lee, J.-E., Evans, N.J.II, Shirley Y.L., & Tatematsu, K. 2003, ApJ, 583, 789

Lehar, J., Falco, E.E., Impey, C.D., Kochanek, C.S., McLeod, B.A., Rix, H.-W., Keeton, C.R., Munoz, J. & Peng, C.Y. 1999, ApJ, 523, 617

Li, Z. & Shu, F.H. 1997, ApJ, 475, 237

Looney, L.W., Mundy, L.G. & Welch, W.J. 2003, ApJ, 592, 255

Looney, L.W., Mundy, L.G. & Welch W.J. 2000, ApJ, 529, 477

Matthews, K. & Soifer, B.T. 1994, in *Infrared Astronomy with Arrays: the Next Generation*, ed. I. McLean (Dordrecht: Kluwer Academic Publishers), p. 239

Mathis, J. 1990, ARA&A, 28, 37

McLaughlin, D.E., & Pudritz, R.E. 1997, ApJ, 476, 750

McLeod, B. 1997, in *1997 HST Calibration Workshop,* ed. S. Casertano et al., p. 281

Menten, K.M., Walmsley, C.M., Krugel, E. & Ungerechts, H. 1984, A&A, 137, 108

Monet, D., Bird A., Canzian, B., Dahn, C., Guetter, H., Harris, H., Henden, A., Levine, S., Luginbuhl, C., Monet, A.K.B., Rhodes, A., Riepe, B., Sell, S., Stone, R., Vrba, F., & Walker, R. 1998, The USNO-A2.0 Catalogue, (U.S. Naval Observatory, Washington DC)

Motte, F. & André, P. 2001, A&A, 365, 440

Mouschovias, T.Ch. 1976, ApJ, 207, 141

Mundy, L.G., Looney, L.W., Erickson, W., Grossman, A., Welch, W.J., Forster, J.R., Wright, M.C.H., Plambeck, R.L., Lugten, J. & Thornton, D.D. 1996, ApJ, 464, 169

Mundy, L.G., Looney, L.W. & Welch W.J. 2000, in *Protostars and Planets IV*, eds. V. Mannings, A.P. Boss and S.S. Russell, (Tucson: University of Arizona Press), p. 355

Myers, P.C., Evans, N.J.II & Ohashi, N. 2000, in *Protostars and Planets IV*, eds. V. Mannings, A.P. Boss & S.S. Russell, p. 217

Myers, P.C., Fuller, G.A., Goodman, A.A., & Benson, P.J. 1991, ApJ, 376, 561

Myers, P.C., Fuller, G.A., Mathieu, R.D., Beichman, C.A., Benson, P.J., Schild, R.E., &

Emerson, J.P. 1987, ApJ, 319, 340

Myers, P.C., & Lazarian, A. 1998, ApJ, 507, 157

Myers, P.C., Linke, R.A. & Benson, P.J. 1983, ApJ, 264, 517

Nagai, T., Inutsuka, S.-I., & Miyama, S.M. 1998, ApJ, 506, 306

Natta, A. 1993, ApJ, 412, 761

Ossenkopf, V. & Henning, T. 1994, A&A, 291, 943

Osterloh, M. & Beckwith, S.V.W. 1995 ApJ, 439, 288

Ostriker, J. 1964, ApJ, 140, 1056

Penston, M.V. 1969, MNRAS, 144, 425

Persson, S.E., Murphy, D.C., Krzeminski, W., Roth, M. & Rieke, M.J. 1998, ApJ, 116, 2475

Plummer, H.C. 1911, MNRAS, 71, 460

Press, W.H., Teukolsky, S.A., Vetterling, W.T. & Flannery, B.P. 1992, *Numerical Recipies in C*, p. 691

Reike, G.H. & Lebofsky, M.J. 1985, ApJ, 288, 618

Reipurth, B., Rodriguez, L.F., Anglada, G. & Bally, J. 2002, AJ, 124, 1045

Rodriguez, L.F., Carral, P., Moran, J.M., & Ho, P.T.P. 1982, ApJ, 260, 635

Saito, M., Sunada, K., Kawabe, R., Kitamura, Y. & Hirano, N. 1999, ApJ, 518, 334

Sandford, S.A. & Allamandola, L.J. 1993, ApJ, 409, L65

Schneider, S., & Elmegreen, B.G. 1979, ApJs, 355, 172

Shirley, Y.L., Evans, N.J.II, Rawlings, J.M.C. & Gregerson, E.M. 2000, ApJs, 131, 249

Shirley, Y.L., Evans, N.J.II & Rawlings, J.M.C. 2002, 575, 337

Shu, F.H. 1977, ApJ, 214, 488

Shu, F.H., Adams, F.C., & Lizano, S. 1987, ARA&A, 25, 23

Shu, F.H., Najita, J., Galli, D., Ostriker, E., & Lizano, S. 1993, in Protostars and Planets III, eds. E. Levy and J. Lunine (Tucson: University of Arizona Press), p. 3

Stahler, S.W. 1988, ApJ, 332, 804

Tafalla, M., Mardones, D., Myers, P.C., Caselli, P., Bachiller, R., & Benson, P.J. 1998, ApJ, 504, 900

Tafalla, M., Myers, P.C., Caselli, P., Walmsley, C.M. & Comito, C. 2002, ApJ, 569, 815

Tafalla, M., et al. 2003, *in preparation*

Takahashi, T., Silk, J., & Hollenbach, D.J. 1983, ApJ, 275, 145

Terebey, S., Shu, F.H. & Cassen, P. 1984, ApJ, 286, 529

Tomita, Y., Saito, T. & Ohtani, H. 1979, PASJ, 31, 407

Visser, A. 2000, Ph.D. thesis, University of Cambridge (UK)

Visser, A.E., Richer, J.S. & Chandler, C.J. 2001, MNRAS, 323, 257

Walmsley, M., Caselli, P., Zucconi, A., & Galli, D. 2001, in Proceedings of ESO workshop, The Origins of Stars and Planets: The VLT View, eds. J. Alves and M. McCaughrean

Ward-Thompson, D. 1993, MNRAS, 265, 493

Ward-Thompson, D., Andreé, P. & Kirk, J.M. 2001, MNRAS, 329, 257

Ward-Thompson, D., Motte, F. & André, P. 1999, MNRAS, 305, 143

Ward-Thompson, D., Scott, P.F., Hills, R.E. & Andre, P. 1994, MNRAS, 268, 276

Whitworth, A.P., & Ward-Thompson, D. 2001, ApJ, 547, 317

Williams, J.P., Myers, P.C., Wilner, D.J. & Di Francesco, J. 1999, ApJ, 513, L61

Wilner, D.J., Chen, H. & Myers, P.C. 1997, HST Cycle 7-NICMOS proposal, GO-7843

Wilner, D.J., Ho, P.T.P. & Rodriguez, L.F. 1996, ApJ, 470, 117

Wilner, D.J., Myers, P.C., Mardones, D. & Tafalla, M. 2000, ApJ, 544, 69

Zhou, S. 1992, ApJ, 394, 204

Zhou, S. 1995, ApJ, 442, 685

Zhou, S. & Evans, N.J.II 1994, in *Clouds, Cores and Low Mass Stars: the Fourth Haystack Observatory Conference,* eds. D. Clemens and R. Barvainis, (San Fransisco: ASP), p. 183

Zhou, S., Evans, N.J.II, Butner, H.M., Kutner, M.L., Leung, C.M. & Mundy, L.G. 1990, ApJ, 363, 168

Zhou, S., Evans, N.J.II, Kompe, C. & Walmsley, C.M. 1993, ApJ, 404, 232

Zucconi, A., Walmsley, C.M., & Galli, D. 2001 A&A, 376, 650